THE MEASUREMENT OF INTER-PARTICLE DIFFUSION COEFFICIENTS IN MINE WASTES

by

Peter Van Eck

A thesis
presented to the University of Waterloo
in fulfillment of the
thesis requirement for the degree of
Master of Science
in
Earth Sciences

Waterloo, Ontario, Canada, 2021

Author's Declaration

I hereby declare that I am the sole author of this thesis. This is a true copy of the thesis including any required final revisions, as accepted by my examiners.

I understand that my thesis may be made electronically available to the public.

ABSTRACT

Acid mine drainage (AMD) is the release of acidic waters from mines, waste-rock piles and mine tailings impoundments containing high concentrations of SO_4, Fe(II) and other metal(oid)s. The bulk of AMD generation occurs in the vadose zone where water and $O_{2(g)}$ can react with the gangue sulfide minerals present in mine waste. The ability to quantify and model the limiting reactants of water and $O_{2(g)}$ is vital to understanding and controlling the generation of AMD at a mine site.

Characterizing the unsaturated properties of mine wastes is important for determining the rate of sulfide oxidation and the extent of AMD. Soil-water characteristic curves (SWCC) are a tool used to describe the unsaturated conditions present in mine waste. Soil-water characteristic curves were measured using matrix-matrix material (<4.75 mm) from three mine sites: Faro Mine Complex, YT; the Detour Lake Gold Mine, ON; and Diavik Diamond Mine, NT, to examine the differences in matrix-material particle-size distribution among mine sites and the effect of particle-size distribution on SWCC morphology. Estimations of effective diffusion coefficients and sulfide oxidation rates were calculated using parameters derived from these measurements. The results indicate that mine waste-rock matrix material can exhibit a high degree of hysteresis, that can result in differences between oxygen diffusion coefficients and sulfide oxidation rates during wetting and drying stages. The results contribute to the characterization of the unsaturated properties of mine wastes and provide estimates of the variation in inter-particle diffusion coefficients of mine waste in response to changing moisture content reflecting hysteresis.

Laboratory column experiments were conducted to measure $O_{2(g)}$ diffusion rates through variably saturated waste-rock matrix material. Effective diffusion coefficients were calculated using the numerical model MIN3P for both wetting and drying phases of waste-rock matrix material to assess the impact of hysteresis on $O_{2(g)}$ diffusion. The calculated effective diffusion coefficients were used to estimate sulfide oxidation rates to observe potential variability in oxidation rate caused by hysteresis. The results from the SWCC measurements indicate the potential for waste-rock matrix material to exhibit a high degree of hysteresis. The results from the laboratory column experiments indicate that the effect of hysteresis on effective diffusion coefficients and sulfide oxidation rates was negligible for high values of negative matric suction. Potential concern for the impact of hysteresis on sulfide oxidation rates occurs at near zero-values of matric suction where estimated effective diffusion coefficients and sulfide-oxidation rates vary by orders of magnitude.

ACKNOWLEDGEMENTS

I would first and foremost like to thank my supervisor Dr. David Blowes for accepting me to this amazing program. His patience, guidance and expertise have been inspiring and immensely helpful in my journey through my Masters. I would also like to thank my committee members Dr. Tom Al and Dr. Walter Illman for their assistance and interest in my project. It has been a privilege to work with all of you.

I would also like to express my gratitude and appreciation to everyone I have met along the way. Thank you to: David Hilger, David Geuder, Joanne Angai, Adrienne Schmall, Carol Ptacek, David Wilson, Jeff Bain, Sara Fellin, Steve Holland, Keith Delaney, Sue Fisher, Filip Budimir, Alexei Tarnopolski, Esteban Larrea, Mason McAlary, Brent Verbuyst, Emily Saurette and Zhongwen Bao and every member of the GGR research group who have helped me.

I would like to thank my Mom, my Dad and my brother Daniel for their unconditional love and encouragement in this pursuit. This past year has been hard not seeing you and I can't wait to see you all soon.

Finally, last but not least, a special thank you to my girlfriend Gabi and my dog Obi who have been amazing roommates over the course my Masters. Thank you for all the love, advice, encouragement, and rides to and from work. I am going to miss the home we have built here but I am optimistic and excited for our road ahead. Thank you and I love you both.

TABLE OF CONTENTS

LIST OF FIGURES

LIST OF TABLES

LIST OF SYMBOLS / ABBREVIATIONS

a shape fitting parameter of the soil-water characteristic curve (-)

a_1 model coefficient for the Kovács (1981) model (= 2.5×10^{-3}) (-)

a_2 model coefficient for the Kovács (1981) model (= 7.5×10^{-2}) (-)

C_U uniformity coefficient (-) ($C_U = D_{60}/D_{10}$)

C_0 atmospheric concentration of oxygen (kg m^{-3})

D_a^0 free-air diffusion coefficient for $O_{2(g)}$ (m^2 s^{-1})

D_w^0 free-water diffusion coefficient for $O_{2(g)}$ (m^2 s^{-1})

D_{e_O2} effective diffusion coefficient for oxygen (m^2 s^{-1})

D_a diffusion coefficient component in the air phase (m^2 s^{-1})

D_h effective particle size (cm)

D_w diffusion coefficient component in the water phase (m^2 s^{-1})

D_{10} diameter corresponding to 10% passing on the cumulative particle-size distribution curve (cm)

D_{60} diameter corresponding to 60% passing on the cumulative particle-size distribution curve (cm)

H Henry's equilibrium constant (-)

m shape fitting parameter of the soil-water characteristic curve (-)

n shape fitting parameter of the soil-water characteristic curve (-)

p_w Aachib (2002) model parameter related to tortuosity

p_a Aachib (2002) model parameter related to tortuosity

r degree of hysteresis (-)

R overall oxidation rate (kg (O_2) m^3 s^{-1})

S' intrinsic oxidation rate (kg (O_2) m^{-3} s^{-1})

S_a adhesive force contributing to the total saturation (-)

S_c capillary force contributing to the total saturation (-)

S_r degree of saturation ($S_r = \theta/\theta_s$)

x, y material parameters used in Collin and Rasmuson (1988) (-)

α inverse of the air-entry pressure (kPa^{-1})

α_k shape factor (-)

ϕ porosity (-)

θ volumetric moisture content ($m^3\ m^{-3}$)

θ_a volumetric-air content ($m^3\ m^{-3}$)

θ_r residual moisture content ($m^3\ m^{-3}$)

θ_s saturated moisture content ($m^3\ m^{-3}$)

$\Delta\theta_{max}$ maximum difference of moisture content between the two curves at a specified ψ ($L^3\ L^{-3}$)

τ_a tortuosity for the air phase

τ_w tortuosity for the water phase

ψ matric suction (kPa)

ψ_a matric suction of the AEV (kPa)

ψ_r matric suction corresponding to residual saturation (kPa)

AMD	Acid-mine drainage
SWCC	Soil-water characteristic curve
IOR	Intrinsic oxidation rate

CHAPTER 1

INTRODUCTION

1.1 Background

An average metal mine immediately rejects 42% of the total mined material as waste rock (spoil), 52% of the ore is separated at the mill as tailings, 4% leaves the smelter as slag, and only 2% is retained as the commodity for which the ore was extracted (Godin, 1991). The mining industry is the largest producer of waste in the World, producing about 59 billion tonnes annually, based on 2010 production figures (Jones, 2012). As the population of the World and standard of living continues to rise, so does the demand for metals. With the readily accessed minerals consumed, there has been a shift towards extracting less accessible minerals, producing a greater amount of waste for each unit of metal mined.

If not carefully managed, mine waste poses a significant problem for the surrounding environment and local populations. The oxidation of sulfide minerals, such as pyrrhotite ($Fe_{1-x}S$) and pyrite (FeS_2), is the dominant process in mine waste leading to the degradation of nearby groundwater and surface water. The oxidation reactions for these minerals are shown in Equations 1.1 and 1.2, respectively (Blowes et al., 2013).

(1.1) $$Fe_{1-x}S_{(s)} + \left(2 - \frac{x}{2}\right) O_2 + xH_2O \rightarrow (1-x)Fe^{2+} + SO_4^{2-} + 2xH^+$$

and

(1.2) $$FeS_{2(s)} + \frac{7}{2}O_2 + H_2O \rightarrow Fe^{2+} + 2SO_4^{2-} + 2H^+$$

Equations 1.1 and 1.2 represent the production of acid-mine drainage (AMD), which is due to the oxidation of iron-sulfide minerals, resulting in poor-quality leachate characterized by acidic pH and high concentrations of dissolved iron, sulfate and metals. The generation of AMD

in waste-rock piles is governed by the rate of sulfide mineral oxidation. Understanding the role of the reactants, oxygen gas ($O_{2(g)}$) and water, is vital to determining the quantity and quality of the leachate produced from waste-rock piles.

1.2 Organization

The contents of this thesis are divided into four chapters. Chapter 1 provides an introduction, a background of waste rock hydrogeology, site descriptions for the three sites associated with this project, the Diavik Diamond Mine, NT, the Detour Lake Gold Mine, ON, and the Faro Mine Complex, YT, as well as project research objectives. Chapter 2 contains particle-size analysis of matrix material, the measurement of hysteretic soil-water characteristic curves using laboratory methods and the estimation of effective diffusion coefficients and sulfide oxidation rates. Chapter 3 provides the laboratory measurement of the effect of hysteresis on inter-particle diffusion coefficients in mine-waste matrix material and the implications on sulfide mineral oxidation. Lastly, Chapter 4 provides a summary of the conclusions from the research and ideas for future work.

1.3 Waste-Rock Hydrogeology

1.3.1 *Waste-Rock Clast Composition*

Waste-rock piles are highly heterogenous with particle sizes ranging from clay to boulders. Variations in particle size, mineralogy and morphology of the waste-rock pile are dependent on the geologic properties of the ore deposit, the mining technique and the method of dumping the waste rock into piles (Smith, 1995). Waste-rock piles, and zones within a waste-rock pile, can be characterized as either having soil-like or rock-like properties. Waste rock is

considered soil-like when the fines contain greater than 20% sand-sized particle-size fraction and finer, and is characterized by a fine-grained matrix that supports larger clasts with hydraulic properties reflective of the fine-grained matrix. Rock-like waste-rock piles, or areas within the pile, are composed of rock on rock contact with matrix free void spaces with fluid flow mechanisms and hydraulic properties resembling coarse grained material (Momeyer, 2014).

1.3.2 *Fluid Flow in Waste-Rock Piles*

Precipitation falling on the surface of waste-rock piles may either run off, infiltrate or evaporate. Infiltration into waste-rock piles is dependent on rain-fall intensity, topography, antecedent moisture content, and infiltration capacity of the surface material. Matrix flow and preferential flow are the two main types of water flow mechanisms in waste-rock piles (Nichol et al., 2005). Matrix flow refers to water flow through the fine-grained matrix material, which occurs as result of gravity and capillary action. Water flow through preferential pathways is driven by macropore flow and film flow, which transports water through localized pathways at greater rates than the average water flow velocity in the system (Tokunaga and Wan, 2001). The differences in matrix flow versus preferential flow paths leads to differences in drainage quality and residence time, which affects the geochemical signature of the effluent. Water that flows more slowly through the matrix material, interacts with a greater surface area of minerals producing a larger dissolved load in the drainage (Smith and Beckie, 2003). Cash (2014) estimated average residence time for water in matrix fines to be 200 to 400 days assuming 100% infiltration. With typical average flow velocity through the matrix material on the order of 1 m/year to 5 m/year (Ritchie, 1994). Waste-rock matrix material is classified as the <4.75 mm fraction of waste rock based on observations that diffusion is the primary O_2 ingress process and

that little water retention and capillary flow occurs within pore spaces coarser than 4.75 mm (Neuner, 2009; Yazdani et al., 2000; Amos et al., 2015; Pantelis and Ritchie, 1992).

Most of the flow through a waste-rock pile will occur through the fine-grained matrix material in response to infiltration rates that are less than the saturated hydraulic conductivity value of the fine-grained matrix (Smith, 1995). At the beginning of a rainfall event, capillary forces and gravity draw the precipitation into the waste-rock pile. When the surface material reaches close to uniform moisture content the infiltration rate approximately equals the hydraulic conductivity of the material. The amount of precipitation that exceeds the infiltration capacity of the fine-grained matrix material will either infiltrate through the macropores or pond and create surface runoff. Waterflow through macropores occurs in connected matrix-free pore spaces between clasts greater than a 5 mm diameter (Nichol et al. 2005).

1.3.3 *Freeze-Thaw Effects on Water Transport in Waste Rock*

At northern mine sites which are subject to freeze-thaw condition, the near surface area that thaws from the onset of warmer temperatures during the late-spring and summer months is known as the active zone. There is potential for AMD to occur in the active-zone of the waste-rock piles during the warmer months. Development of the active zone is influenced by the gas-permeability and air-filled porosity of the waste-rock pile. An increase in permeability and large air-filled voids within the pile will result in an increase of depth of the active zone (Fretz, 2013). As the ambient air temperature begins to drop in the fall months, freezing conditions migrate inward from the top of the pile as well as the batters of the stockpile. A freezing front will also migrate upward from the base of waste-rock piles that are constructed on permafrost (Momeyer, 2003). This freezing and thawing process increases the complexity of flow regimes in waste rock

by creating non-uniform active periods for flow paths in waste-rock piles. Water that is held by relatively low matrix tension will freeze more rapidly as the temperature decreases, while moisture in matrix material, held at high matrix tension, may remain liquid at temperatures below freezing. Matrix material that has wet-up prior to freezing conditions will be largely ice-filled, whereas larger macropores will remain air-filled or partially frozen (Neuner, 2009). Water infiltrating to the interface of the active-zone and the frozen zone will likely result in the development of ice-saturated matrix material. Neuner (2009) found that the development of a frozen zone can act to redistribute pore water closer towards the ice due to a matrix-suction gradient created by the freezing of the waste rock. This redistribution creates layers or films of higher moisture content filling larger air-filled voids adjacent to frozen areas, decreasing the local air-filled porosity.

Fretz (2013) observed a correlation between the increase in warmer temperatures and a rapid increase in the average volumetric-water content recorded by TDR sensors. Conversely, temperatures below freezing resulted in a rapid decrease in average volumetric-water content. Highest outflow occurs from the thawing of the edges of the waste-rock pile during the initial spring melt. Volumetric discharge becomes increasingly proportional to the thawed volume of waste rock as the interior of the pile thaws. As the discharge from the spring melt occurs, a sharp gas concentration gradient can develop between the gas-filled pore space and the atmosphere, resulting in an increase in gas ingress into the pile. As the ambient air temperature drops, the outer portion of the pile begins to freeze and discharge decreases. However, the inner portion of the pile still contains liquid water allowing for longer residence times and greater solute loading (Momeyer, 2003; Fretz 2013).

1.4 Site Descriptions

1.4.1 *Diavik Diamond Mine, NT*

Located 300 km northeast of the Northwest Territories capital Yellowknife, the Diavik Diamond Mine is situated on a 20 km^2 island in Lac de Gras (Figure 1.1). The mine is in a continuous permafrost region with an average air temperature of -12° C, ranging between -50° C to +25° C (Yip and Thompson, 2015).

Since 2003, Diavik has utilized a combination of both underground and open pit mining to extract ore from three kimberlite pipes for diamond recovery (DDMI, 2004). The kimberlite pipes are hosted by Archean country rock composed primarily of granite (75%) and pegmatitic granite (14%) with the smaller fraction being biotite schist (10%) and diabase dykes (1%) (Jambor, 1997). Sulfidic minerals are primarily found as trace quantities of pyrite in granite and as pyrrhotite in biotite schist.

Diavik Diamond Mines has a waste-rock management program that segregates the waste rock into three operational classifications based on the sulfur content (Table 1). A series of three test piles were constructed at the Diavik site to study the evolution of hydrogeology, geochemistry, mineralogy and microbiology of the waste rock, and to evaluate the potential effectiveness of a proposed closure concept. The experimental piles include a Type-I waste-rock test pile, a Type-III waste-rock test pile and a covered pile, based on a closure concept for the Type-III waste rock which includes a 1 m layer of till overlain by 3 m of low-sulfide Type-I waste rock. The piles were constructed by standard end and push dumping methods (Smith et al., 2013). Each test pile covers an area of approximately 3000 m^2 with an average height of 15 m. The Type-I waste-rock pile is primarily composed of granite and has the lowest wt % S (< 0.04) of the three types. Type-III waste rock contains greater than 0.08 wt % S due to higher

concentrations of biotite schist in the host rock. Portions of the Type-III pile are potentially acid-generating as determined by standard acid base accounting methods (Smith et al., 2013). The samples collected from Diavik for this project originated from the deconstruction of the Type-I test pile.

1.4.1.1 *Diavik Waste Rock Characterization*

The test piles at Diavik were constructed with end-dumping construction methods characterized by finer-particle size fraction near the crest of the pile with coarsening of particle size from the crest to the base of the pile (Chi et al., 2013). The waste-rock matrix, defined as particles finer than 4.75 mm, comprises 18% of the waste rock within the Type-I test pile. Due to the low abundance of matrix material, the test piles are best characterized as rock-like having fluid flow mechanisms and hydraulic properties resembling coarse-grained material (Smith et al. 2013). Sieving of 197 samples finer than 100 mm in diameter to analyze the <5 mm portion indicated that, on average, the matrix material of the Type-I test pile consisted of 28% gravel, 65% sand and 7% silt and clay (Neuner, 2009). The matrix material in the Type-III test pile had a mean particle size distribution of 26% gravel, 67% sand and approximately 7% silt and clay. Porosity values of six samples of matrix material were measured and determined to be 0.25 ± 0.02 (Neuner, 2009; Neuner et al. 2012; Smith et al., 2013). Estimates of matrix porosity as a proportion of total porosity of the waste-rock pile were 5% (Diavik Waste Rock Program, 2009).

1.4.1.2 *Water Flow Mechanisms*

Precipitation data has been consistently recorded at the Diavik Diamond Mine site since 1997. Rainfall generally occurs between the months of May to October, with mean monthly

rainfall peaking in August. Average annual rainfall recorded from 1999 to 2010, and from 2013 to 2015 was 135.0 mm (DDMI, 2017). Water flows through the waste-rock pile in two different ways: matrix and preferential flow (Nichols et al. 2005; Smith et al, 2013; Neuner et al., 2013). Infiltration into the waste-rock pile at less than field capacity will be held in the matrix until drainage occurs (Bear, 1972). During low precipitation events, infiltrating water will move through the matrix domain. The activation of preferential flow paths where water flows through macropores is gravity driven and can occur during high-intensity precipitation events. A high-intensity rainfall for Diavik is characterized as a rainfall with a recurrence interval of approximately 2 years (Neuner, 2009). Such an event would produce rainfall of 6 mm/hr for one hour or 1.5 mm/hr for twelve hours (Golder, 2008). Neuner (2009), observed only one high-intensity rainfall event of 7.7 mm/hr lasting for 3.8 hours on September 13, 2007. This rainfall event generated rapid, spatially variable flow indicative of macropore flow. Momeyer (2014) also observed an intense rainfall event (35.8 mm in 24.8 hours) in which the activation of preferential flow paths occurred. However, while preferential flow was observed, it was not the dominant flow mechanism during this event based on the geochemical signature of the effluent from the waste-rock pile.

1.4.2 *Detour Lake Gold Mine, ON*

Detour Lake Gold Mine is located in northern Ontario, Canada about 300 km northeast of Timmins and 8 km west of the Ontario - Québec border within the northwestern portion of the Archean Abitibi greenstone belt (Figure 1.2). In 2018, average daily temperatures ranged from -23.7° C in January to 24.3° C in July with an average total precipitation of 851 mm the majority of which occurred between June and October (Jensen, 2018).

Detour Lake Mine was operated between 1983 and 1999 by Placer Dome Inc. and generated 1.8 million ounces of gold and 14.3 million tonnes of waste rock from both open-pit and underground mining (Oliver et al, 2011). The waste rock was separated into four stockpiles around the open pit starting in 1983. Due to the low price of gold and the depletion of high-grade gold deposits mining operations ceased in 1999. In 2006 Detour Gold Corporation (DGC) purchased the property and resumed mining operations in early 2013. With the redevelopment and construction of new properties, the mine plans to be operational for 23 more years and is expected to produce 16.4 million ounces of gold. DGC plans to remove approximately 2.2 billion tonnes of rock, the majority of which will be stored in new waste-rock piles (Panneton, 2009; Cash, 2014; McNeill, 2016).

The Detour Lake Gold Mine is located within the Archean Abitibi greenstone belt that is comprised of volcano-sedimentary assemblages and adjacent plutonic-gneissic terranes. Oliver et al. (2012) provides a recent and complete geologic history of the greenstone belt. Three main geologic units; the Upper Detour Lake Formation (UDLF), Lower Detour Lake Formation (LDLF) and Caopatina assemblage are intersected by the mining operations at Detour Lake (McNeill, 2016). The UDLF is made up of mafic tuffs, mafic flows, mafic hyaloclastites and pillowed flows and that constitutes approximately 55% of the waste rock in the stockpiles. The remaining 45% of the waste rock is composed of the LDLF, which consists of ultramafic to mafic flows, sills and dikes, and felsic volcaniclastic rocks. The Caopatina formation is composed of interbedded argillaceous siltstones, quartz wackes, banded amphibolites, and lesser mafic volcanic rocks (Oliver, 2012; Robertson, 2012; McNeill, 2016).

1.4.2.1 *Detour Waste Rock Characterization*

The historic waste-rock piles at Detour Lake were constructed in 10-15m lifts using a push or paddock-style dumping method, which resulted in particle sizes fining upward with coarse-grained boulders and cobbles at the bottom of the lifts (Cash, 2014). The stockpiles contained primarily plagioclase, quartz, horneblende and clinochlore minerals, with trace amounts of biotite (Cash, 2014). The main sulfide minerals in the waste-rock piles were pyrite and pyrrhotite, with small amounts of chalcopyrite and covellite. McNeill (2016) determined the sulfur content of waste-rock stockpile #1 (WRS#1) and WRS#2 ranged from 0.05 – 2.2 wt % S. Over 50% of the sample collected from these two stockpiles were potentially acid generating. WRS#3 and WRS#4 were slightly less sulfidic, with sulfur contents of 0.1 wt % S and 0.6 wt % S, respectively. None of the samples from WRS#3 were considered potentially acid generating; however, 45% of WRS#4 were considered potentially acid generating. In WRS#1 and WRS#2, particle size trends showed an enrichment in S, Fe, Cu, Ni, and Zn in the finer particle size fractions (Cash, 2014; McNeill, 2016).

The portion of material passing a No. 4 (4.75mm) sieve is defined as the waste rock matrix material at Detour (Cash, 2014; McNeill, 2016). The porosity of the matrix material ranged from 0.3 to 0.5. Due to the low proportion of fines in the waste-rock pile, the matrix material contributed little to the overall porosity in the range of 0.05 to 0.12. None of the samples Cash (2014) collected had greater than 40% passing the 4.75 mm sieve. Additionally, digital image processing (DIP) analysis of the waste-rock piles demonstrated that on average the <4.75 mm fraction only made up 17% of the waste-rock mass (McNeill, 2016). These observations indicate that the waste-rock piles should behave as rock-like material with a clast support structure containing voids that are empty or filled with matrix materials.

1.4.2.2 *Water and Gas Transport*

The oxidation of sulfide minerals and transport of AMD are dependent on water flow within the waste-rock pile. Due to particle sizes ranging from clay to boulders, the stockpiles are highly heterogenous making it difficult to characterize water flow throughout the pile. Using a porosity average of 0.40 for the matrix material, saturation of the matrix material ranged from 12.5% to 62.5% (McNeill, 2016). The permeability of WRS#3 ranged from 8.5×10^{-11} to 1.9×10^{-9} m^2 with the cover material being on the order of 10^{-11}. The average permeability among Detour waste rock ranged from 10^{-9} to 10^{-11}. In a study by Pantelis and Ritchie (1992), gas transport as a means by diffusion was dominant in material with a permeability of $<10^{-10}$ m^2. Additionally, the cover system over the stockpiles helped to limit the advection of $O_{2(g)}$. McNeill (2016) noted that advection was likely a factor in WRS#4 due to a damaged cover system from excavation in June 2012. Pore-gas concentrations decreased with increasing distance from the surface of the pile in WRS#3, which is consistent with diffusion as the dominant $O_{2(g)}$ transport process. Comparatively, in WRS#4 pore-gas $O_{2(g)}$ concentrations were near atmospheric levels though being consumed by the oxidation of sulfide minerals; indicative of a faster recharge of $O_{2(g)}$ in the pore spaces due to advective gas transport (Cash, 2016; McNeill, 2016).

1.4.3 ***Faro Mine Complex, YT***

Once the largest open pit lead – zinc mine in the world, the Faro Mine Complex now sits abandoned awaiting remediation. Faro is located in the central Yukon, Canada about 200 km northeast of Whitehorse, the capital of the Yukon (Figure 1.3). The Faro Mine is situated in a sub-arctic region of Canada within a discontinuous permafrost zone. Faro officially opened in 1969 when it began the production of lead and zinc ore moving up to 10,000 tonnes of rock per

day. At the end of operation, 70 million tonnes of tailings and 320 million tonnes of waste rock containing sulfide minerals remained at Faro (Tang, 2011). This waste rock has the potential to leach heavy metals and acid as a result of oxidation of the sulfide minerals.

The Faro and Grum deposits, as well as the Mount Mye and Vangorda formations are the main deposits associated with the Faro mining operations. The Faro Deposit is one of five major synsedimentary lead-zinc silver deposits along the southern edge of the Anvil Batholith. The deposit lies approximately 100 m below the Mount Mye-Vangorda Formation contact. Due to proximity to the batholith, the Mount Mye Formation rocks were metamorphosed to biotite-andalusite-muscovite schist, and the overlying Vangorda Formation banded calc-silicate. The Grum Deposit, located 12 km southeast from the Faro deposit, is a major lead-zinc silver deposit that consists of three to five massive sulfide lenses containing graphitic-phyllite and quartz-phyllite. Seven sulfide rock types have been associated with these formations. The dominant sulfide rock is quartzose with pyrite, with other major sulfide minerals occurring as pyrrhotite, schist, chalcopyrite and marcasite. Acid-base accounting was used to estimate acid generation potential of each waste-rock pile. Sulfide-rock content of the dumps varied from 0 to 100% with an average of 13%. Only four dumps (less than 10% of the total waste rock) were expected to contain no sulfide rock. However, since mining records do not specify in which dump the rock was placed and the degree of mixing of the various rock types, these estimates are limited (Deloitte & Touche, 2004; Robertson GeoConsultants Inc., 1996).

The Faro Mine Complex has a total footprint of approximately 25 km^2 and can be divided into three main areas: Faro Mine, Rose Creek Tailings, and the Vangorda Plateau. The two areas that contain waste rock dumps are the Faro Mine Pit and the Vangorda Plateau. The Faro Mine area includes a large open pit approximately 1 km^2, surrounded by 250 million tonnes of waste

rock. The waste rock located in this dump is primarily composed of schist, calcareous silicates and overburden rock units with total sulfur content of 4.72%. Potential sources of inflow of water into the waste-rock pile include leakage from Faro Creek along the eastern wall of the main pit, local runoff from the sub-catchment of the main pit, and seepage of shallow ground water from Faro Creek Valley into the north wall (Robertson GeoConsultants Inc., 1996)

The Vangorda Plateau contains two open pits, the Vangorda and Grum pits with 16 million tonnes of waste rock and 100 million tonnes of waste rock, respectively (Horvath, 2011). The main rock type of these two pits consists of calcareous phyllite, phyllite and sulfide rock with a total sulfur content of 5.22% at Vangorda and 1.67% at the Grum pit. Mineralogical analysis of the particle-size fractions showed that sulfur content is similar throughout, regardless of particle size. (Deloitte & Touche, 2004; Robertson GeoConsultants Inc., 1996).

1.4.3.1 *Gas Transport*

Two boreholes along with instrumentation were installed at the Faro intermediate dump. One borehole was located in a sulfide cell and the other closer to the edge of the pile. For the borehole in the sulfide cell, temperature in the waste-rock pile was affected by seasonal changes to a depth of around 5.6 m. The maximum temperature increased to around 50 °C at a depth of around 20 m. Below 20 m, temperatures sharply drop to about 6 °C at the bottom of the borehole. Oxygen pore gas concentrations decreased to about 5 vol. % at a depth of 5 m. The borehole located outside of the cell near the edge of the pile had a temperature profile similar to that of the borehole in the sulfide cell. The $O_{2(g)}$ concentrations ranged from 15 to 20 vol. %. The high $O_{2(g)}$ concentrations, along with the high temperatures within the pile indicated a high oxidation rate as well as advective gas flow into the pile (Deloitte & Touche, 2004).

1.5 Research Objectives

The intent of this project is to measure soil-water characteristic curves for waste rock matrix material for the three mine sites as well as calculate values for inter-particle diffusion coefficients for waste-rock matrix material using a modification of the technique presented by Rouf et al. (2012). Samples collected from Faro Mine Complex, YT, the Detour Lake Gold Mine, ON, and Diavik Diamond Mines, NT will be subjected to drying and wetting conditions to simulate a hysteretic effect. The moisture content of these samples will be adjusted to evaluate the degree of hysteresis and the moisture content-matric suction relationship to develop a series of inter-particle diffusion coefficients. These values, accompanied with a better understanding of the relationship between hysteresis and $O_{2(g)}$ transport, will help to improve the predictions of sulfide-oxidation rates within mine wastes.

The overall goal is to measure variations in inter-particle diffusion coefficients in waste rock matrix material to evaluate the impact of hysteresis, or the wetting and drying effect, on these values. The scope of this project involves laboratory analyses and experimentation with a saturation diffusion apparatus. This research does not include the measurement of *in situ* inter-particle diffusion coefficients or *in situ* hysteretic behavior. Few studies have simultaneously measured gas-transport parameters and soil-water characteristic curves under repeated wetting and drying conditions.

FIGURES

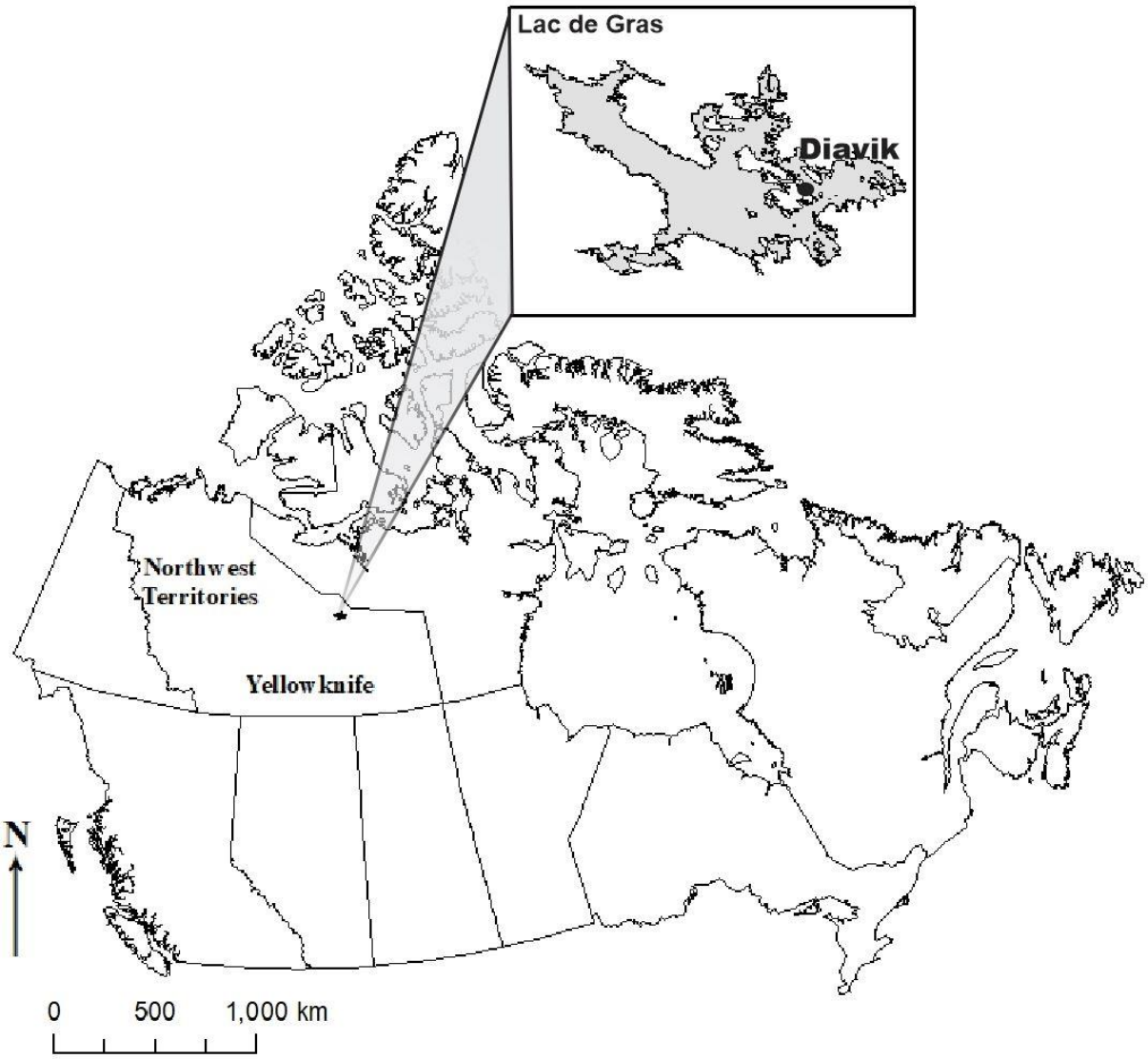

Fig. 1.1 Diavik Diamond Mine located 300 km northeast of Yellowknife, Northwest Territories, Canada in Lac de Gras.

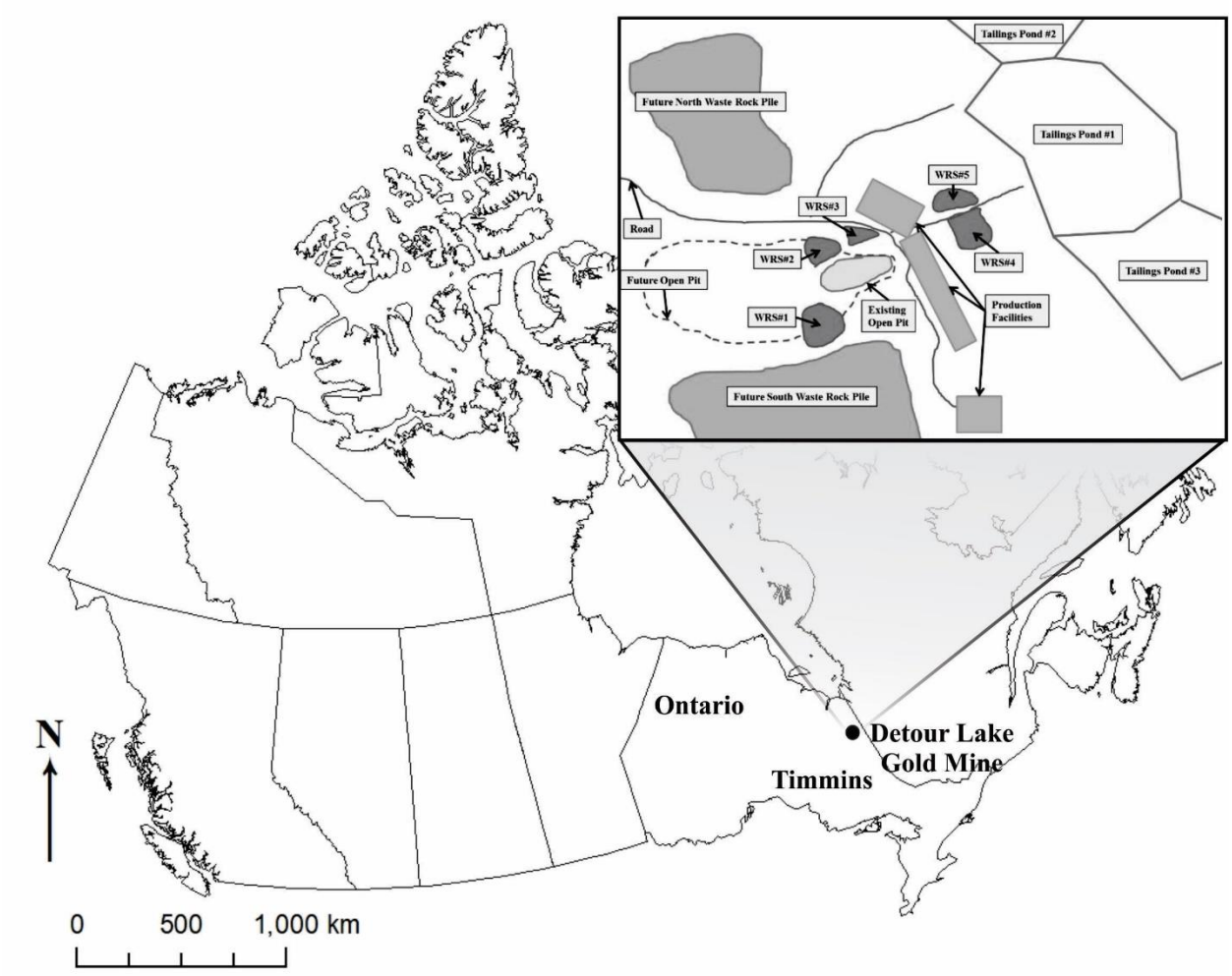

Fig. 1.2 Location of the Detour Lake Gold Mine, Ontario, Canada**.**

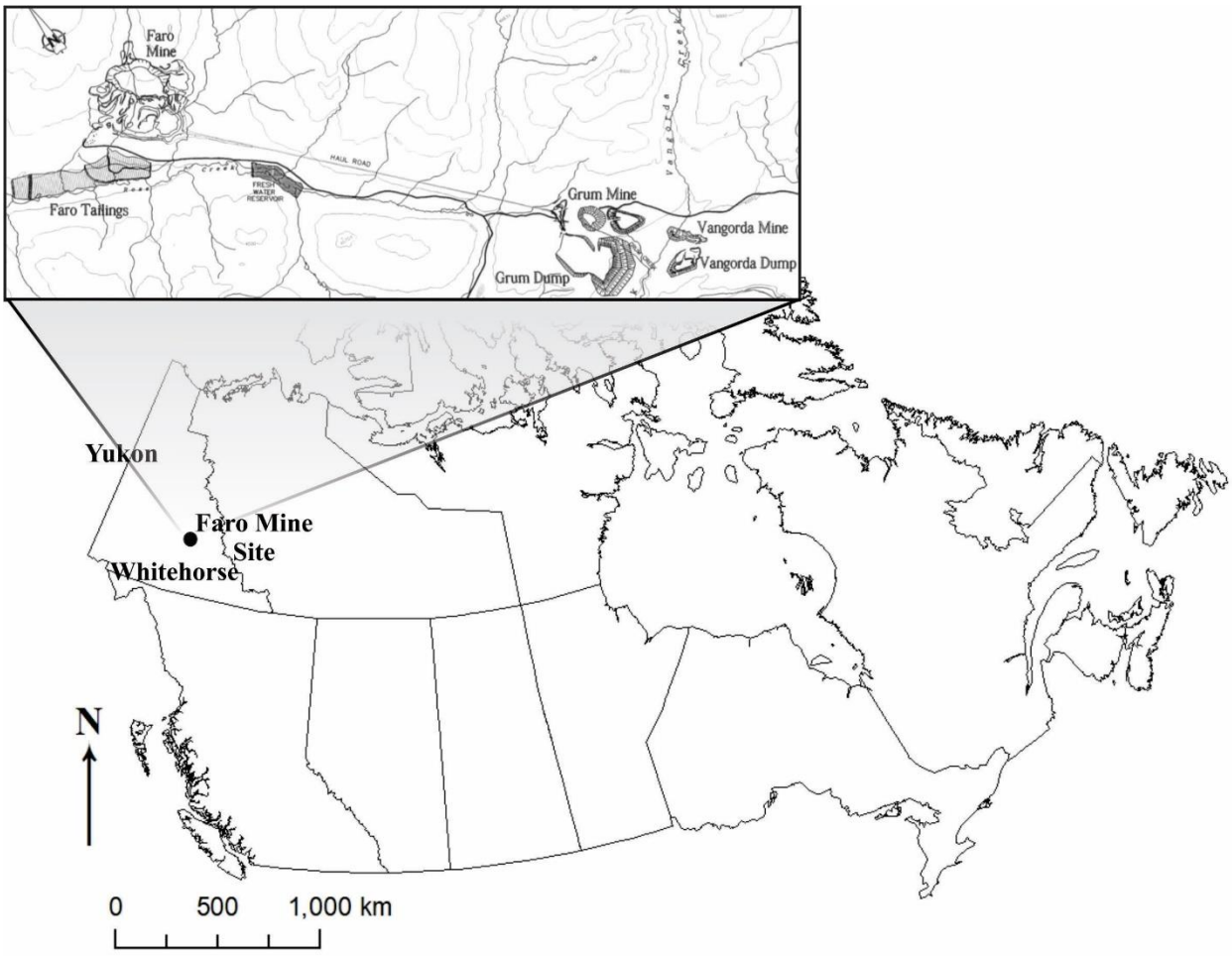

Fig. 1.3 Location of the Faro Mine Complex, Yukon, Canada.

TABLES

Table 1 Waste-rock management plan at Diavik Diamond mine divided into three types (Diavik Diamond Mines, 2004)

Diavik Waste Rock Classification	Weight % Sulfur Content	Acid-Generating Potential
Type I	< 0.04	Non-acid-generating
Type II	0.04 - 0.08	Low acid-generation potential
Type III	> 0.08	Potentially acid-generating

CHAPTER 2

MEASUREMENT OF HYSTERETIC SOIL-WATER CHARACTERISTIC CURVES OF MINE WASTE AND THE ESTIMATION OF EFFECTIVE DIFFUSION COEFFICIENTS AND SULFIDE OXIDATION RATES

2.1 Introduction

Understanding water flow through unsaturated waste materials at mine sites is vital in quantifying and preventing low-quality drainage from mill tailings and waste rock. Moisture content in a waste-rock pile is temporally variable due to evaporation, infiltration, and drainage, which results in varying oxygen diffusion coefficients throughout the waste-rock pile, and affects the potential for release of effluent containing high concentrations of dissolved metals that are detrimental to human health and the environment. A soil-water characteristic curve (SWCC) describes the unsaturated flow properties of materials, including hydraulic conductivity and water storage, and provides useful data, such as van Genuchten parameters (Fredlund, 2019), for incorporation in numerical modeling. Soil-water characteristic curves illustrate the relationship between volumetric moisture content (θ) and matric suction (ψ) of a porous material (Rahardjo et al., 2019). The change in moisture content due to increasing ψ provides a delineation of the three main hydrologic zones in a waste-rock pile; namely the (1) phreatic zone, (2) capillary fringe, and (3) the unsaturated zone (Fig. 2.1).

Wetting and drying are unique processes that are accompanied by hysteresis, wherein the moisture content at a specified ψ is lower during wetting than during drying. The degree of hysteresis is empirically determined as the difference between the main-drying and wetting curves of a SWCC. Determination of a SWCC within a mine-waste pile is complicated by the degree of heterogeneity of pore size, shape, distribution, and mineralogy. Due to both time and difficulty of *in situ* measurements and laboratory methods, SWCCs are often estimated using

empirical relationships incorporating porosity, particle size and matric suction (Aubertin et al., 1998; Swanson et al., 1999; Fredlund et al., 2002; Aubertin et al., 2003; Martin et al., 2004). Although these techniques provide an expedited and cost-effective method to characterize the SWCC of a material, caution must be taken because the effects of confinement, fabric, stress history and hysteresis are often not included in the estimation (Fredlund et al., 2002).

Because little water retention and capillary flow occurs within pore spaces of waste rock that is coarser than 4.75 mm (Pantelis and Ritchie, 1992; Yazdani et al., 2000; Tokunaga et al., 2002), most studies on water movement in waste-rock piles focus on the fine-grained matrix material. The objective of this study is to measure and compare soil-water characteristic curves and to evaluate the impact of hysteresis on inter-particle diffusion coefficients and sulfide oxidation for waste-rock matrix material (<4.75 mm), from three mine sites (Faro Mine Complex, YT; the Detour Lake Gold Mine, ON; and Diavik Diamond Mine, NT).

2.2 Materials and Methods

2.2.1 *Particle-Size Analysis*

Waste-rock samples collected at 1.5 m below ground surface from waste-rock piles at the Faro Mine Complex, YT, the Detour Lake Gold Mine, ON, and Diavik Diamond Mines, NT were sieved following ASTM D6913 (2017) standards to collect matrix material finer than 4.75 mm. Prior to sieving, the samples were oven dried at 60 ˚C for 24 h. The dried samples were loaded into a single sieve set with a maximum particle size of 4.75 mm. The sieve set consisted of mm grating sizes of 4.75 (No. 4), 2.36 (No. 8), 1.00 (No. 18), 0.600 (No. 30), 0.355 (No. 45), 0.180 (No. 80), and 0.075 (No. 200). The sample was loaded into the sieve set in batches of 200 – 400 g to prevent overloading within the sieve column. The sieve column was placed onto a

mechanical-sieve shaker for 15 to 20 minutes to ensure the matrix material was properly fractionated. The total mass of matrix material sieved for each of the three sites was 11,500 ± 300 g. The geometric mean and standard deviation of the particle-size diameters were calculated using the graphical method described by Folk and Ward (1957). To quantify the degree of sorting, the coefficient of uniformity ($C_U = D_{60}/D_{10}$) was calculated; where D_{60} and D_{10} are the particle sizes at which 60% and 10% of the particles are finer, respectively. Values of $C_U > 6$ correspond to a poorly-sorted material (Watson and Burnett, 1995).

2.2.2 *Laboratory Measurement of Soil-Water Characteristic Curves*

Sieved matrix material from each site was recombined and thoroughly mixed, and packed into Tempe cells (3.0 cm high, 5.5 cm diameter) to 1.60 ± 0.10 g cm^{-3}, to mimic *in situ* bulk density values (Bao et al., 2020; Neuner et al., 2013; Cash, 2014). The ceramic plates (ψ value at air-entry, ψ_a, of 100 kPa) were saturated by soaking in deionized water for 48 hours. The samples were placed onto the ceramic plates and saturated for at least 48 hours by allowing water into the base of the plate. After saturation, the top of each Tempe cell was fastened and the cell weight was recorded.

Following ASTM 6836 (2016) the Tempe cells were attached to a hanging-water column to generate lower pressures (< 10 kPa) to capture the ψ_a of the material. The hanging-water column was lowered in 10-20 cm intervals (1-2 kPa) and the weight was recorded after equilibrium was reached. Once the hanging-water column reached 1 m (10 kPa), the Tempe cells were disconnected from the hanging-water column and attached to a pressure manifold.

Following a test procedure described by Gallage et al. (2013), a pressure-manifold system with compressed air was utilized to obtain pressures up to 100 kPa. Air pressure was applied to the top port of the Tempe cell causing water to drain out of the bottom port. The Tempe cell was

repeatedly weighed at an applied pressure until the weight of the Tempe cell reached equilibrium. This procedure was repeated until a pressure of 1 bar (100kPa) above atmospheric was achieved. At this point the drying process was stopped and the wetting curve was initiated.

The wetting process was started by decreasing the applied air pressure to the Tempe cell allowing water to re-enter the system through capillary action (Gallage et al., 2013). The Tempe cell was connected to a water reservoir vented to the atmosphere with the water level of the reservoir maintained at the middle height of the sample in the Tempe cell. The water reservoir provided a source of water to re-enter the Tempe cell. Care was taken to ensure air bubbles did not form a gap between the water reservoir and the ceramic plate of the Tempe cell. Each Tempe cell was disconnected from the manifold and weighed daily to determine the gravimetric water content. When the main-wetting curves of the matrix material were completed, the Tempe cells containing the sample were oven dried for 24 hours at 60 °C and weighed. Using the recorded weights, volumetric-moisture contents were back calculated at each pressure change of the experiment and plotted against the applied ψ to determine the SWCC.

Both the main-wetting and drying curves for each material were modeled separately using the van Genuchten (1980) and Fredlund & Xing (1994) equations. The van Genuchten equation is:

(2.1) $$\theta = \theta_r + \frac{\theta_s + \theta_r}{\left[1 + \left(\frac{\psi}{\alpha}\right)^n\right]^m}$$

Where, θ is the volumetric moisture content, α [kPa^{-1}] is the inverse of ψ_a, and n and m [-] are shape fitting parameters of the soil-water characteristic curve. The variable θ_r represents the residual-volumetric moisture content [m^3 m^{-3}] and θ_s represents the saturated-volumetric moisture content [m^3 m^{-3}].

The Fredlund & Xing equation (1994) is:

(2.2) $$\theta = \theta_s \left[\frac{1}{\ln\left[e+\left(\frac{\psi}{a}\right)^n\right]}\right]^m$$

Where θ_s corresponds to the saturated-volumetric moisture content and θ is the volumetric moisture content. The variables a, n, and m [-] are fitting parameters and ψ has units of kPa.

Using Eq. [2.3], the difference between the main-wetting and drying curves for each matrix-material, modeled by the van Genuchten equation, were used to determine the degree of hysteresis. Where r [-] is the degree of hysteresis and $\Delta\theta_{max}$ represents the maximum difference of moisture content between the two curves at a specified ψ (Konyai et al., 2009).

(2.3) $$r = \frac{\Delta\theta_{max}}{\theta_s - \theta_r}$$

2.2.3 *Prediction of the Soil-Water Characteristic Curve*

The drying components of the SWCCs were estimated for each sample using Kovács model (Kovács, 1981; Aubertin et al., 1998):

(2.4) $$S_r = S_c + S_a(1 - S_c)$$

with

(2.5) $$S_c = 1 - \left[\left(\frac{h_{co}}{\psi}\right)^2 + 1\right] exp\left[-\left(\frac{h_{co}}{\psi}\right)^2\right]$$

(2.6) $$S_a = a_1\left(\frac{1-\phi}{\phi}\right)\psi^{-\frac{1}{6}}\left(\frac{\alpha_k}{D_h}\right)^{\frac{1}{3}}$$

(2.7) $$h_{co} = a_2\left(\frac{1-\phi}{\phi}\right)\left(\frac{\alpha_k}{D_h}\right)$$

In Eq. [2.4], S_r is the degree of saturation ($S_r = \theta/\theta_s$), and S_c and S_a are the capillary and adhesive forces contributing to the total saturation. The values of S_c and S_a are determined using the porosity (ϕ), a shape factor (α_k), the effective particle size of the matrix material (D_h), and model coefficients a_1 and a_2 ($a_1 = 2.5 \times 10^{-3}$ and $a_2 = 7.5 \times 10^{-2}$).

The shape factor α_k approximately varies between 6 (sphere) and 18 (tetrahedron) and is estimated using the relationship $\alpha_k/D_h = 4/D_{10}$ to $10/D_{10}$. The parameter D_h was estimated from the following equation (Mbonimpa et al., 2003; Aubertin et al., 1998):

(2.8) $$D_h = (1.17 \log C_U + 1)\, D_{10} \qquad \text{for } C_U \leq 50$$

2.2.4 *Calculating Effective Diffusion Coefficients*

A semi-empirical relationship modified from the Millington and Quirk (1961) expression was developed by Collin and Rasmuson (1988) to account for gaseous diffusion through air, and through water when $S_r > 85\%$ (Eq. 9).

(2.9) $$D_{e\_O2} = D_a + HD_w$$

Where H is the Henry's equilibrium constant [-] ($H \approx 0.03$ at room temperature for $O_{2(g)}$) and the parameters D_a and D_w are the diffusion coefficient components for $O_{2(g)}$ in the air and water phase respectively, and are expressed as:

(2.10) $$D_a = \theta_a D_a^0 \tau_a \quad \text{and} \quad D_w = \theta D_w^0 \tau_w$$

Where θ_a and θ are the volumetric-air and moisture contents [$L^3\ L^{-3}$], D_a^0 is the free-air diffusion coefficient for O_2 (1.8×10^{-5} $m^2\ s^{-1}$) and D_w^0 is the free-water diffusion coefficient for O_2 (2.5×10^{-9} $m^2\ s^{-1}$) (Aachib et al. 2002; Scharer et al., 1993). The parameters τ_a and τ_w are the tortuosity corrections for the air and water phases (Collin and Rasmuson, 1988). And are related to basic material properties as:

(2.11) $$\tau_a = \frac{{\theta_a}^{2x+1}}{\phi^2} \quad \text{and} \quad \tau_w = \frac{\theta^{2y+1}}{\phi^2}$$

Where *x* and *y* are material parameters that can be determined from the following expressions (Collin and Rasmuson, 1988):

(2.12) $$\theta_a^{2x} + (1-\theta_a)^x = 1 \quad \text{and} \quad \theta^{2y} + (1-\theta)^y = 1$$

A second, semi-empirical expression was also used to estimate D_{e_O2} for the drying curve based on the material properties, θ and ϕ (Aachib et al., 2002).

(2.13) $$\mathrm{D_{e\_O2}} = \frac{1}{\phi^2}\{D_a^0 \theta_a^{3.3} + \mathrm{H} D_w^0 \theta^{3.3}\}$$

2.2.5 *Estimating Sulfide Oxidation Rates*

To further evaluate the effect of variable $O_{2(g)}$ diffusion coefficients on sulfidic waste-rock piles, oxidation rates for the three study sites were calculated using (Gibson et al., 1994):

(2.14) $$R = \sqrt{2S'C_0 D_{e\_O2}}$$

Where R [kg (O_2) m^{-3} s^{-1}] is the overall oxidation rate, S' [kg (O_2) m^{-3} s^{-1}] is the intrinsic oxidation rate, C_0 [kg m^{-3}] is the atmospheric oxygen concentration. Values for S' were derived from humidity cell experiments for each of the three sites (SRK Consulting, 2004; Robertson et al., 2012; Langman et al., 2014). The D_{e_O2} values that were estimated with the method described by Collin and Rasmuson (1988) were used in these calculations.

2.3 Results

2.3.1 *Particle-Size Characteristics*

The percent-passing measurements were compiled to summarize the particle-size characteristics for each of the samples (Fig. 2.2; Table 2.1). The slopes of the PSD curves

illustrate that the matrix material from all three sites is poorly sorted. The C_U was calculated for each of the materials and all have C_U values above 6, with the Detour mine samples having the highest value (Table 2.1).

Particle-size classifications (ASTM, 2006) for each of the matrix materials range from clay/silt to fine gravel, representing poorly-sorted gravelly sands with fines. Faro samples have the lowest percentage of fines (D_{10} = 0.173 mm), and Diavik and Detour matrix materials have D_{10} values of 0.122 mm and 0.101 mm (Table 2.1). Using the graphical method described by Folk and Ward (1957), the geometric mean particle diameter was calculated for each site. The geometric means for material from Diavik and Detour are similar at 0.594 and 0.642 mm respectively. The geometric mean for the material from Faro is 0.878 mm, which is 42% coarser, on average, than both Diavik and Detour. Variations in the particle sizes of the matrix materials between the three sites likely reflect a combination of factors including blasting techniques, material-handling and dumping methods, and mineralogical composition and particle size of the host rock.

2.3.2 *Soil-Water Characteristic Curves*

Gravimetric differences between the oven-dried and fully saturated Tempe cells containing the samples were used to calculate porosity values. Porosities for the Diavik, Detour and Faro samples are 0.216, 0.227 and 0.301, respectively. The data that define the SWCCs (θ versus ψ) are plotted for each material in Figure 2.3, showing both the wetting and drying curves. These SWCC data were fit with the van Genuchten (1980) and Fredlund & Xing (1994) models using a non-linear fitting program (Seki, 2007) to determine the parameters in Eq. [2.1] (n, α and θ_r; Table 2.1) and Eq. [2.2] (a, n, m; Table 2.1). The SWCCs developed from the van Genuchten and Fredlund & Xing models show good agreement with the laboratory measurements (Fig. 2.3).

The R^2 values ranged from 0.97 – 0.99 indicating excellent fits between the models and the data (Table 2.1). The predicted drying curves were also estimated from empirically derived particle-size parameters using the Kovács model (Fig. 2.3; Kovács, 1981).

The Diavik SWCC has the highest θ_r value of 0.063. Both Detour and Faro SWCCs have estimated θ_r values near zero. It is possible that the θ_r values were not achieved for the matrix-materials during the laboratory measurements because they are very poorly-sorted materials requiring high pressures to remove the residual water from the finer pore spaces. The high pressures needed to remove this moisture were probably not attained during the laboratory measurements because of limitation of the ceramic plate.

Degrees of hysteresis (r) were calculated for the three materials using Eq. [2.3] (Konyai et al, 2009). The sample from the Detour mine was determined to be the least hysteretic with the lowest r value (0.217), whereas samples from the Diavik and Faro mines exhibited higher degrees of hysteresis with r values of 0.402 and 0.451, respectively. The Faro mine matrix material had the greatest $\Delta\theta_{max}$ value (0.13 [$m^3\ m^{-3}$]) between the wetting the drying curves. Material from the Diavik and Detour mines had similar $\Delta\theta_{max}$ values of 0.06 and 0.05 [$m^3\ m^{-3}$] respectively.

2.3.3 *Calculated Diffusion Coefficients and Sulfide Oxidation Rates*

Estimated effective diffusion coefficients of $O_{2(g)}$ (D_{e_O2}) for the wetting and drying curves were calculated using the Collin and Rasmuson (1988) relationship (Fig. 2.4; Eq. 2.9). Calculated D_{e_O2} values from the three sites ranged in order of magnitude from 10^{-11} to 10^{-6}. Diffusion coefficients for Diavik mine material ranged from 1.1×10^{-11} to $6.0 \times 10^{-7}\ m^2\ s^{-1}$. Detour mine material had a similar range from 1.1×10^{-11} to $6.4 \times 10^{-7}\ m^2\ s^{-1}$ and Faro matrix material had the largest range from 1.6×10^{-11} to $1.9 \times 10^{-6}\ m^2\ s^{-1}$. The D_{e_O2} values estimated

using the method of Collin and Rasmuson (1988) were compared to the Aachib et al. (2002) approach which modeled D_{e_O2} values across the range of saturation (0.0 to 1.0) for a material with similar porosity and show good agreement. Faro mine matrix material displayed the largest difference in D_{e_O2} between wetting and drying, with a factor of 1.7×10^4 increase in D_{e_O2} for wetting compared to drying conditions. In comparison, the D_{e_O2} increased by factors of 1.1×10^3 and 1.3×10^3 for the Detour and Diavik matrix materials, respectively. For each material, as the values of ψ increase, the difference between D_{e_O2} values for the wetting versus drying curves becomes negligible.

Overall oxidation rates for the three study sites were calculated using a simple homogeneous oxidation model developed by Gibson et al. (1994) for pyrite oxidation in a waste-rock dump (Fig. 2.5; Table 2.3; Eq. 2.14). Estimated oxidation rates for the Faro mine matrix material ranged from 3.6×10^{-10} to 1.1×10^{-7} kg (O_2) m^{-3} s^{-1}. Detour mine matrix material ranged from 1.8×10^{-10} to 4.3×10^{-8} kg (O_2) m^{-3} s^{-1} and Diavik mine matrix material ranged from 1.3×10^{-11} to 3.0×10^{-9} kg (O_2) m^{-3} s^{-1}. Estimated oxidation rates for the three variably-saturated matrix materials show a similar relationship to the estimated D_{e_O2} values (Fig. 2.4). The calculated oxidation rates from the wetting process were higher compared to the drying process with the greatest difference in oxidation rates at near-zero values of ψ. Faro matrix material had the largest difference in oxidation rates with 130 times increase in sulfide-oxidation rate under wetting conditions compared to drying conditions. The Diavik matrix material had the second largest increase; 36 times increase in sulfide-oxidation rate during the wetting conditions. The Detour matrix material had the largest increase, with 34 times increase in sulfide-oxidation rate.

2.4 Discussion

2.4.1 *Effect of Particle Size on Soil-Water Characteristic Curve Morphology*

The shape of the SWCC is dictated by the pore-size distribution and ϕ of the material (Yang et al., 2004). Several key parameters are used to characterize SWCC morphology; namely, the θ_r, the slope at the inflection point, and the ψ_a value (Gallage and Uchimura, 2010; Zhai and Rahardjo, 2012; Fredlund et al., 2012). The portion on a SWCC where a large suction change is needed to drain additional water from the soil is the residual saturation zone and defines the upper limit of a SWCC (Barbour, 1998; Yang et al., 2004; Zhai and Rahardjo, 2012). Unlike bulk-waste rock that reaches a low-residual moisture content as a result of gravity drainage, matrix material is poorly-sorted and fine-grained so it is able to retain a higher moisture content. Neuner et al. (2013) compared the SWCC of bulk waste rock to matrix material from Diavik and found that bulk waste rock drained more rapidly and reached a lower residual water content faster than the matrix material. This difference in moisture retention leads to distinct differences in acid-generating potential between bulk-waste rock and matrix material (Blowes, 1997). The longer residence time of water in the matrix material results in a higher concentration of metal(loid)s and increased solute loadings in the porewater (Yazdani et al., 2000; Smith and Beckie, 2003; Stockwell et al., 2006; Smith et al., 2013).

The slope of the SWCC at the inflection point reflects the water-storage potential, wherein a relatively steep slope indicates greater water-storage potential (Swanson et al., 1999; Fredlund et al., 2012). The slope can be calculated as $[(\log \psi_r - \log \psi_a) / (\theta_s - \theta_r)]$ and is related to the PSD curve, with a steep slope being characteristic of a poorly-sorted material, requiring a relatively large change in ψ to desaturate the wider range of pore sizes (Fredlund et al., 2002; Yang et al., 2004; Neuner et al, 2013; Gallage and Uchimura, 2010). Gallage and Uchimura (2010) found that materials with a steeper slope of the PSD curve corresponded to a slope of the

SWCC that drained more rapidly with increases in suction. Faro material displayed a steeper slope of the PSD curve (Fig. 2.2) and a shallower slope of the drying curve of the SWCC (Fig. 2.3); where the larger pore spaces that contain a greater volume of water drain more rapidly in response to small increases in pressure (Benson et al., 2014; Fredlund et al. 2012). Diavik and Detour materials had a similar, shallower, PSD slope that corresponded to a slope of the SWCC requiring a larger range of pressure to desaturate the pore spaces (Fig. 2.2; Fig. 2.3).

Coarser materials begin to desaturate at lower ψ values which corresponds to a lower ψ_a value (Barbour, 1998; Gallage and Uchimura, 2010). The ψ_a value tends to decrease with the increase in D_{10} of the PSD (Yang et al, 2004; Gallage and Uchimura, 2010). Faro material was the coarsest material and had the largest D_{10} value with the lowest ψ_a. Diavik and Detour materials had lower D_{10} values and higher ψ_a values compared to Faro material. Materials with a relatively large ψ_a (smaller D_{10}) can maintain higher θ in the high range of ψ values due to stronger capillary forces. The higher θ results in lower values for θ_a which slows the diffusion of $O_{2(g)}$ into matrix materials.

The PSD and the ϕ of the material influence the r value of a material (Konyai et al., 2009; Gebrenegus and Ghezzehei, 2011; Gallage et al., 2013). Konyai et al. (2009) calculated the r values for six different soils, with values ranging from 0.120 to 0.408, and determined that the coarser materials with lower ψ_a correspond to relatively high r values. Faro matrix material had the greatest r value (0.451) with the lowest ψ_a (7.0 kPa). Detour and Diavik materials have similar ψ_a values (15.4 and 18.5 kPa), however, Diavik material has a greater calculated r value (0.402) than Detour material (0.217). This could illustrate to impact of PSD on r values where the more poorly-sorted material has a lower degree of hysteresis. The matrix materials of Diavik

and Faro fall close to and above the upper range measured by Konyai et al. (2009) indicating that these matrix materials have a greater degree of hysteresis than soils included in that study.

2.4.2 *Impact of Hysteresis on Effective Diffusion Coefficients and Sulfide Oxidation Rates*

Differences in the estimated *R* values between the three sites are attributed to variations in matrix-material properties, which translate into differences in D_{e_O2}, and intrinsic oxidation rates. However, it is generally agreed that the oxidation of sulfide minerals is controlled by the availability of $O_{2(g)}$ (Elberling et al., 1994; Blowes et al., 1997; Lefebvre et al., 2001b; Molson et al., 2005; Demers et al., 2013; Vriens et al., 2018). Experiments designed to measure D_{e_O2} values of waste rock under varying saturations are often difficult to conduct, costly and time consuming (Aachib et al., 2002). Alternatively, numerous models have been established to estimate D_e values based on material properties such as ϕ and θ (Penman, 1940a; Millington, 1959; Millington and Shearer, 1971; Collin and Rasmuson, 1988; Elberling et al., 1994; Aachib et al. 2002). Two of these models have been used in this study to estimate D_{e_O2} values and they show good agreement (Fig. 2.4). For all three matrix materials, estimated D_{e_O2} values are lower at lower values of ψ because of the relatively high degree of saturation and correspondingly lower θ_a and higher tortuosity in the air-filled diffusion pathways. Differences in D_{e_O2} values between the wetting and drying curves are attributed to differences in saturation at varying ψ, reflecting hysteresis. The largest difference in the D_{e_O2} values between wetting and drying phases is at the ψ where the hysteretic effect on the SWCC is the greatest. For all three materials, greater D_{e_O2} values were estimated during the wetting phase at near-zero ψ values and asymptotically approached D_{e_O2} values calculated for the drying curve at high-negative ψ values. This corresponds with the SWCC measurements that showed lower θ during wetting than

during drying across most ψ values (Fig. 2.3) indicating a greater volume of inter-connected pore spaces, which contributes to more rapid rates of $O_{2(g)}$ diffusion (Fig. 2.4; Rouf et al., 2012)

The *R* values estimated in this study fall within the widely reported range of oxidation rates between 10^{-11} and 10^{-5} kg (O_2) m^{-3} s^{-1} (Vriens et al., 2018; Ritchie, 2003; Lefebvre et al., 2001b; Bennett et al., 2000). The wide range of reported values illustrates the impact on sulfide oxidation rates of heterogeneous distributions for parameters such as mineralogy, particle size and diffusion rates. The trend of estimated *R* values with ψ follows the same trend of D_{e_O2} values which is consistent with oxidation being controlled by the availability of $O_{2(g)}$ in mine wastes (Elberling et al., 1994; Blowes et al., 2017; Lefebvre et al., 2001b; Molson et al., 2005; Demers et al., 2013; Vriens et al., 2018).

The hierarchy of the estimated *R* values are in good agreement with the respective properties of the matrix materials. Faro matrix material has the highest ϕ of 0.301 contributing to more rapid rates of $O_{2(g)}$ diffusion and the highest S' calculated from humidity cells. Diavik material has a lowest ϕ value of 0.216 and lowest S' resulting in the lowest *R* values of the three sites. For all three materials, greater *R* values were estimated for more-negative ψ values, which corresponds to lower saturations contributing more rapid rates of $O_{2(g)}$ diffusion into mine wastes (Blowes, 1997; Vriens et al., 2018). The largest difference in estimated *R* values between wetting and drying curves was at near-zero values of ψ where the influence of hysteresis on D_{e_O2} was the greatest. Greater *R* values were estimated for the wetting curve because of lower measured θ values at most ψ values (Fig. 2.3) resulting in the increase availability of $O_{2(g)}$ for the oxidation of sulfide minerals.

2.5 Conclusions

Particle-size analysis and measurement of SWCCs were completed for waste-rock matrix materials from the Diavik Diamond Mine, Detour Gold Mine, and the Faro Mine Complex to evaluate the impact of PSD on SWCC morphology and the degree of hysteresis in the matrix material from waste-rock piles.

The SWCC fitting models, proposed by van Genuchten (1980) and Fredlund & Xing (1994), provided excellent fits to the SWCC data for waste-rock matrix material for the matric suction range of 0–100 kPa. The coarser-matrix material from Faro has the flattest slope because the larger pore spaces drain more extensively in response to small decreases in pressure. The SWCC for poorly-sorted matrix material (e.g., Diavik) is steeper sloped than less uniform matrix material. The maximum difference in θ of the matrix material between the wetting and drying stages ranged between 0.047 [m^3m^{-3}] for Detour and 0.135 [m^3m^{-3}] for Faro. The coarser, poorly-sorted matrix materials from Diavik and Faro had greater calculated *R* values than the more poorly-sorted finer-grained matrix material from Detour. This study shows that waste-rock matrix material has the potential to be strongly hysteretic, resulting in large variability in moisture contents between wetting and drying stages. Whether waste-rock matrix material is predominantly in the wetting or drying phase is dependent on numerous factors including climate, local-scale heterogeneities, depth etc.

Variations in D_{e_O2} values are largely dependent on the unsaturated properties of the matrix material. The estimated D_{e_O2} values for the matrix materials vary by three to five orders of magnitude between wetting and drying cycles at near zero values of pressure head. This variation in D_{e_O2} results in increased rates of sulfide oxidation, by up to two orders of magnitude, under wetting conditions. The impact on the change of moisture content can have a significant effect on solute release rates which are dependent, in part, on oxidation rates. Solute

release rates are also dependent on acid neutralization mechanisms, the formation and dissolution of secondary minerals, and adsorption/desorption reactions.

FIGURES

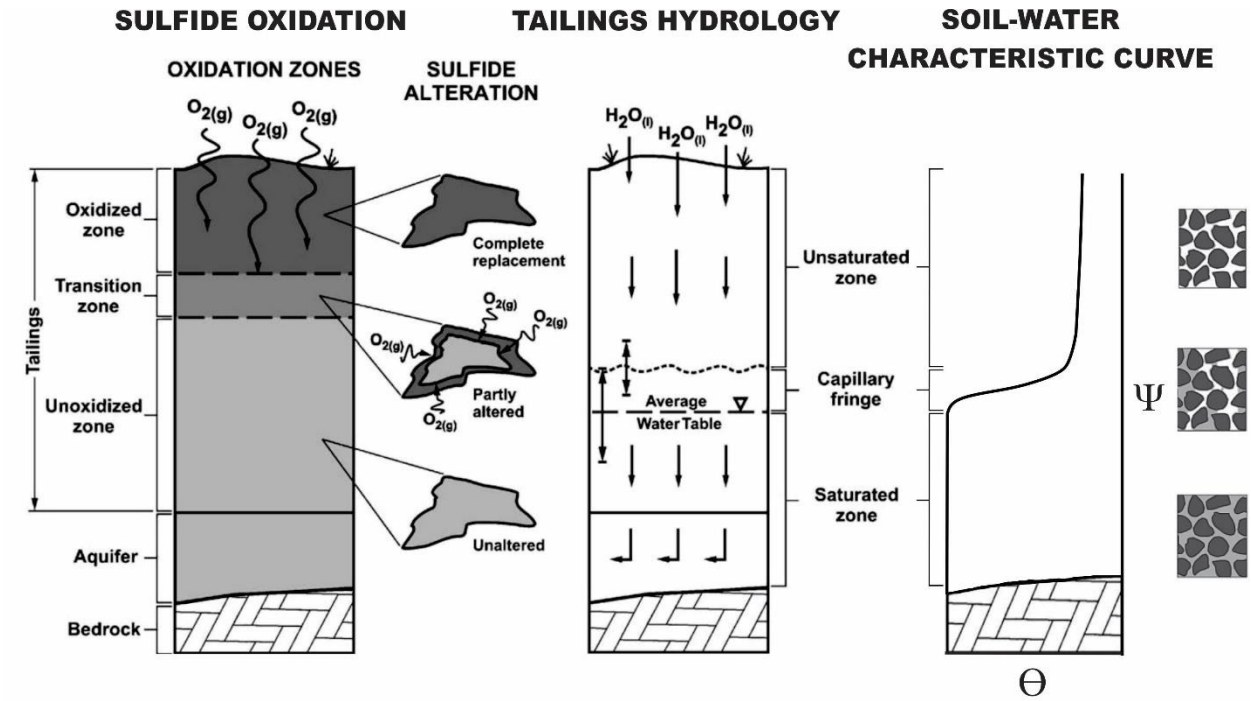

Fig. 2.1 Soil-water characteristic curve corresponding to a typical-tailings profile and the three main sulfide oxidation zones.

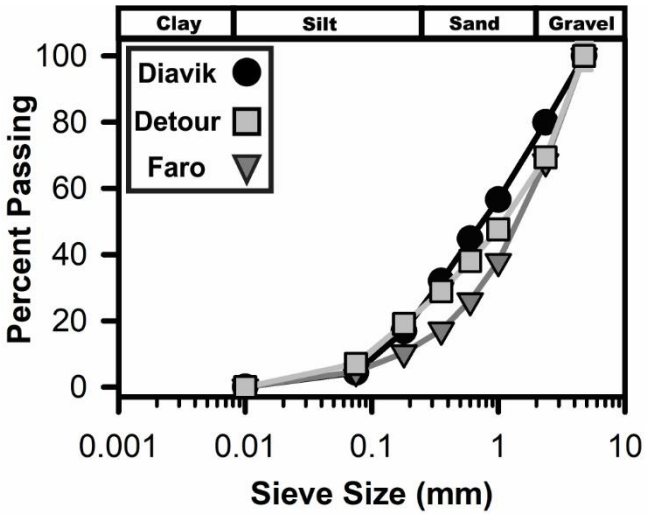

Fig. 2.2 Particle-size distributions for matrix material (<4.75 mm) from Diavik, Detour and Faro. Error bars and the 95% confidence interval were plotted for each sieve size, however, due to the limited extent of the uncertainty they are obscured by the plotting points.

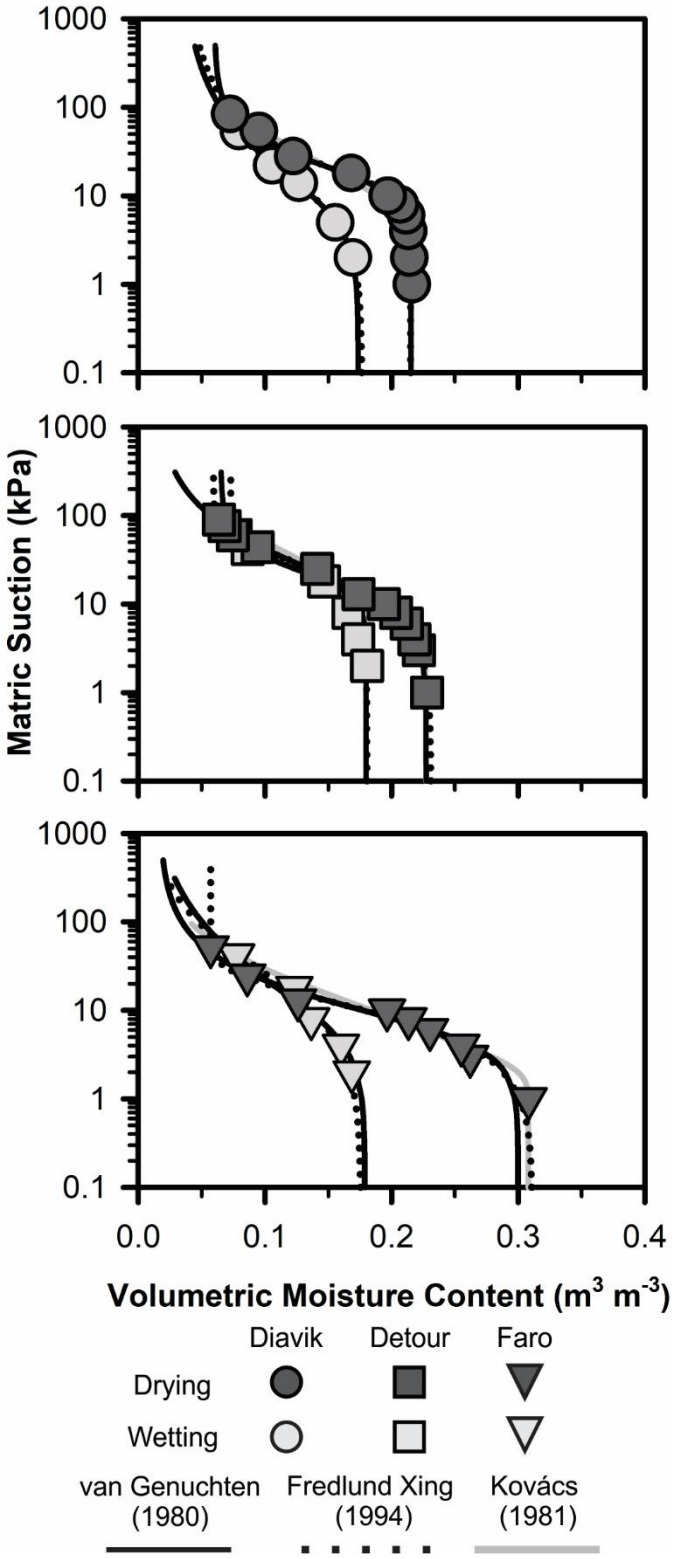

Fig. 2.3 Soil-water characteristic curves for Diavik, Detour and Faro matrix material.

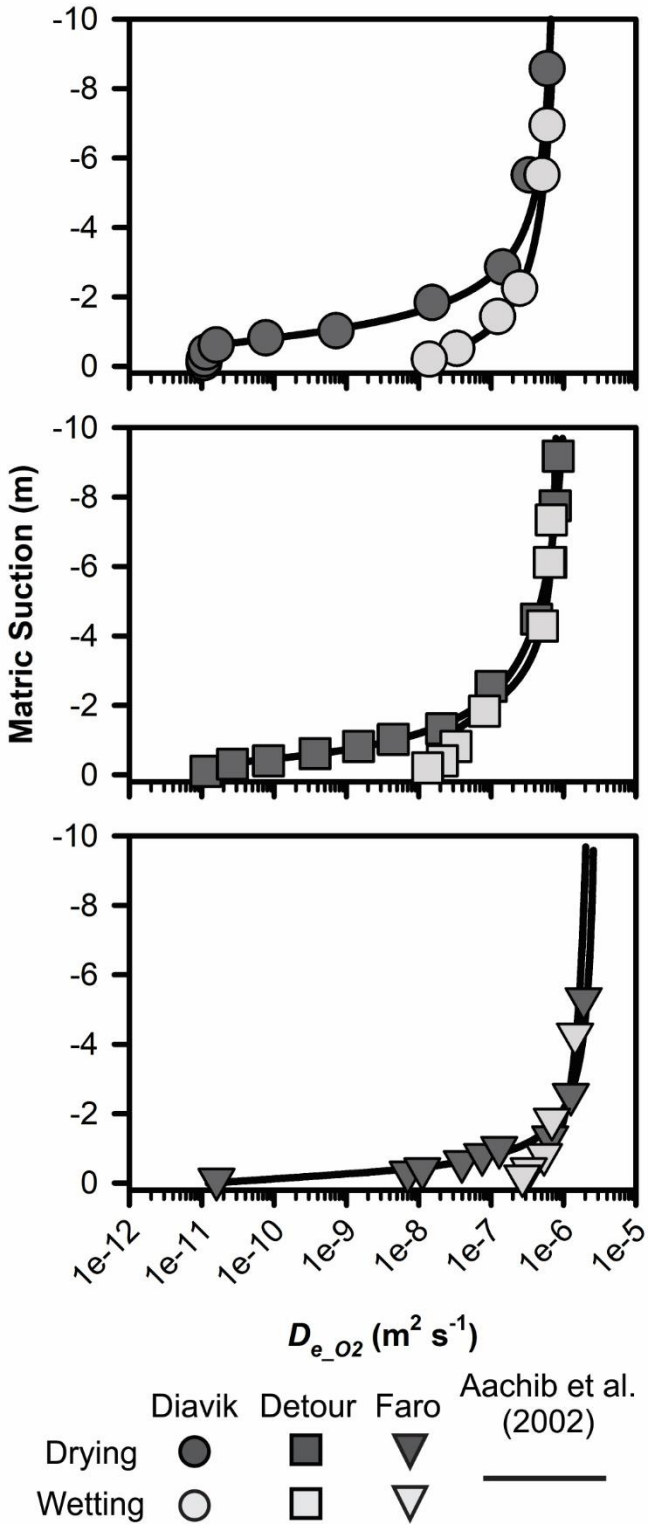

Fig. 2.4 Calculated effective diffusion coefficients for Diavik, Detour and Faro matrix material as a function of ψ.

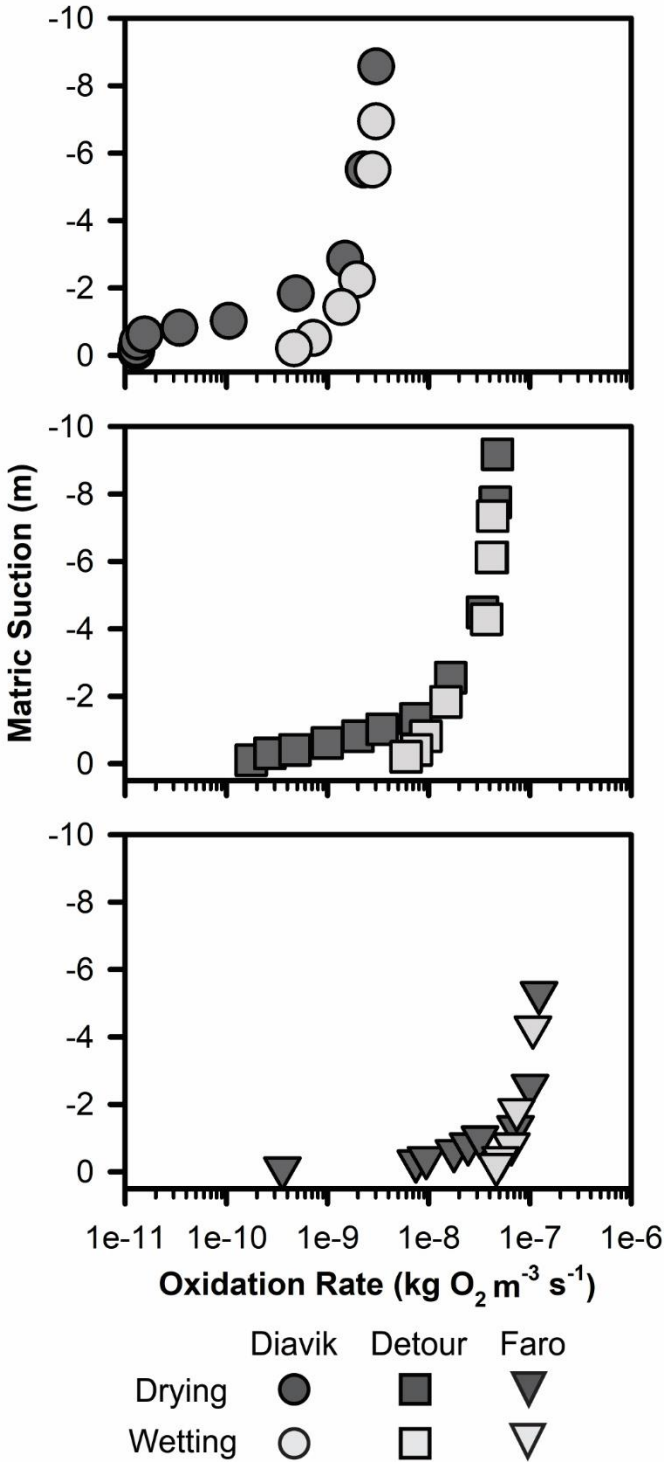

Fig. 2.5 Estimated sulfide-oxidation rates for Diavik, Detour and Faro matrix material.

Tables

Table 2.1: Particle-size analysis parameters.

Location	Mass Sieved (g)	Particle Diameter				Sorting Class	Soil Classification (USCS, 2006)
		D_{10} (mm)	*Geometric Mean (mm)	*Standard Deviation (σ)	Coefficient of Uniformity ($C_U=(D_{60}/D_{10})$		
Diavik	11,315.0	0.122	0.594	0.0028	9.82	Poorly Sorted	Gravelly Sand w/ Fines
Faro	11,544.8	0.173	0.878	0.0022	11.5	Poorly Sorted	Gravelly Sand w/ Fines
Detour	11,775.5	0.101	0.642	0.0031	17.9	Poorly Sorted	Gravelly Sand w/ Fines

* Geometric mean and standard deviation values were calculated using the Folk and Ward (1957) method.

Table 2.2: Modeling parameters for van Genuchten (1980) and Fredlund & Xing (1994) models.

Model	Parameter	Diavik		Detour		Faro	
		Drying	Wetting	Drying	Wetting	Drying	Wetting
van Genuchten (1980)	θ_s	0.216	0.174	0.227	0.180	0.301	0.179
	θ_r	0.063	0.032	9.4E-3	0.065	0.016	3.0E-6
	α	0.054	0.114	0.065	0.047	0.142	0.182
	n	2.64	1.60	1.80	3.17	1.95	1.31
	R^2	0.99	0.99	0.99	0.98	0.97	0.97
Fredlund & Xing (1994)	θ_s	0.215	0.177	0.231	0.180	0.311	0.176
	θ_r	1.1E-5	0.061	0.059	0.073	0.057	3.9E-06
	a	14.5	24.99	447.2	599.3	1580.7	26.1
	m	0.642	3.77	81.1	991.6	1244.0	2.07
	n	2.90	1.19	1.26	1.96	1.27	1.01
	R^2	0.98	0.99	0.99	0.98	0.98	0.99

Table 2.3: Parameters used to calculate *R* values using Gibson et al. (1994) simple homogeneous oxidation model.

Parameter	Diavik	Faro	Detour
S' ($kg\ (O_2)\ m^3\ s^{-1}$)	1.7×10^{-9}	1.5×10^{-7}	5.1×10^{-9}
C_0 ($kg\ m^3$)	0.265	0.265	0.265
D_{e_O2} ($m^2\ s^{-1}$)	1×10^{-11} to 6×10^{-7}	2×10^{-11} to 2×10^{-6}	1×10^{-11} to 6×10^{-7}

CHAPTER 3

LABORATORY MEASUREMENT OF THE EFFECT OF HYSTERESIS ON INTER-PARTICLE DIFFUSION COEFFICIENTS IN MINE-WASTE MATRIX MATERIAL AND THE IMPACT ON SULFIDE OXIDATION RATES

3.1 Introduction

The mining and processing of sulfide-rich ore bodies produces large volumes of wastes that are often stored in the form of heterogeneous sulfide-bearing waste-rock piles and sulfidic-tailings impoundments. If not managed carefully, mine wastes pose a significant threat to the surrounding environment and local population. One consequence of poorly-managed mine waste is the generation of acid-mine drainage (AMD) caused by the weathering of sulfide minerals, resulting in low-quality leachate with elevated concentrations of metal(oid)s. Within a waste rock pile, the production of AMD primarily occurs in the vadose zone, where water and $O_{2(g)}$ interact with sulfide minerals present in mine waste.

The determination of sulfide-oxidation rates within mine wastes is complicated by numerous factors including waste-rock mineralogy, particle size, climate, and availability of the limiting reactants oxygen and water (Amos et al., 2015). Previous studies have established that the availability of $O_{2(g)}$ is the main controlling factor in sulfide oxidation rates within waste-rock piles (Elberling et al., 1994; Lefebvre et al., 2001b; Molson et al., 2005; Demers et al., 2013; Vriens et al., 2018). Advection and diffusion are the two dominant mechanisms for $O_{2(g)}$ transport into a waste-rock pile (Amos et al., 2015). The advective transport of $O_{2(g)}$ is the result of wind-driven air flow into the batters of the pile as well as thermal and pressure gradients. Inter-particle diffusion becomes the dominant process of $O_{2(g)}$ transport into waste-rock material with an air permeability lower than 10^{-10} m^2 (Pantelis and Ritchie, 1992). Quantifying diffusive

rates of $O_{2(g)}$ becomes increasingly important in waste-rock matrix material (<4.75 mm in particle diameter) as a finer texture is associated with an increased surface area of sulfide minerals and increased residence times of water due to capillary forces. Longer residences times coupled with an increased surface area results in a greater release of metal(loid)s and increased solute loadings in porewater (Yazdani et al., 2000; Smith and Beckie, 2003; Stockwell et al., 2006; Smith et al., 2013).

Understanding the relationship between moisture content and gaseous diffusion of $O_{2(g)}$ in a waste-rock pile is vital to predicting the rate and extent of AMD generation. Transport of $O_{2(g)}$ primarily occurs through air-filled voids, because the rate at which $O_{2(g)}$ diffuses through water-filled voids is orders of magnitude slower than diffusion through air (Jones, 2003). The presence of water-filled pores causes an increase in the tortuosity of the air-filled pathway of the porous media, which results in a longer diffusion pathway. The moisture-content throughout mine waste is temporally variable due to infiltration, evaporation, and drainage. Repeated wetting and drying processes result in hysteresis (*i.e.*, the moisture content for the wetting process differs from the drying path at a given matric suction; Pham et al., 2005). Variability in moisture content between wetting and drying phases of mine waste influences the effective diffusion coefficients of $O_{2(g)}$ (D_{e_O2}) within a waste rock pile. The rate of $O_{2(g)}$ diffusion varies temporally and spatially throughout the waste-rock pile dependent on localized moisture-content values (Molson et al., 2005).

Currently, no studies have compared inter-particle diffusion coefficients for mine-waste matrix material under wetting and drying conditions. The calculated D_{e_O2} values are used with mathematical models to estimate overall sulfide-oxidation rates for the matrix materials (Gibson et al., 1994). The goal of this study is to evaluate the impact of hysteresis on inter-particle

diffusion coefficients and examine the variability in sulfide-oxidation rates of waste-rock matrix materials from two mine sites: Faro Mine Complex, YT, and Diavik Diamond Mine, NT.

3.2 Materials and Methods

3.2.1 *Saturation-Diffusion Apparatus*

A saturation-diffusion apparatus that consisted of two individual cylindrical-acrylic chambers was used to measure inter-particle diffusion rates in waste-rock matrix material (Fig. 3.1). The top chamber, designated as the diffusion chamber (12 cm high and an inner diameter of 15 cm), provided a headspace to accumulate $O_{2(g)}$ diffusing through the sample. The diffusion chamber was instrumented with an oxygen sensor [model SO-110, Apogee Instruments] to measure $O_{2(g)}$ within the chamber for the development of breakthrough curves. A gas-injection port was used to purge the entire apparatus with 99.9% $N_{2(g)}$ prior to the start of each diffusion experiment. A hygrometer [Kiyanco mini-hygrometer] was installed into the diffusion chamber to measure the relative humidity to calibrate the oxygen sensor.

The bottom chamber, the sample chamber (39.5 cm high and an inner diameter of 15 cm), had a total of four levels of eight evenly-spaced diffusion ports installed around the circumference of the column (Fig. 3.1). Perforated-polyethylene tubes inserted into the diffusion ports provided uniform distribution of atmospheric air into the sample chamber. A moisture content/temperature/electrical conductivity probe [Decagon Model Devices Inc. 5TE ECH_2O probe] was installed at each level of diffusion tubes to measure the moisture content profile in the matrix material. At the base of the column, beneath a 1-bar porous ceramic plate, a three-way drainage and saturation port was used to control the moisture content of the matrix material in the column. An elevated Mariotte tank, containing deionized water, was used to saturate the matrix material during the wetting process. The drying process was initiated by attaching the

three-way port to a drainage needle to provide slow rates of drainage at high saturations. Lower moisture content values were attained using a vacuum pump and regulator. A heat lamp was introduced above the column to achieve low saturations (*i.e.*, <0.20) through evaporation.

Prior to each experiment, the oxygen sensor was calibrated according to ambient oxygen levels under anaerobic conditions as well as atmospheric conditions. Leak tests were frequently performed to assess the apparatus for both water and air leaks, and to ensure integrity of the experiment. The column was considered leak-proof when the diffusion chamber had an increase of oxygen concentration of 0.05% or less in 180 minutes after being filled with 99.9% $N_{2(g)}$ (Rouf et al., 2012).

The matrix material examined in this study was segregated from bulk waste-rock samples from the Diavik Diamond Mine and the Faro Mine Complex following ASTM D6913 (2017) standards. Oven-dried matrix material was packed into the sample chamber to a bulk density of 1.60 ± 0.10 g/cm^3 according to reported *in situ* values (Bao et al., 2020; Neuner et al., 2013), and tamped down in 2 - 3 cm lifts to eliminate preferential flow paths and macropore spaces. Prior to saturation, the entire apparatus was purged with $CO_{2(g)}$, a highly water-soluble gas, to avoid entrapment of air bubbles in the void spaces. After the column was purged with $CO_{2(g)}$, the matrix material was slowly saturated from the bottom through the saturation port using an elevated Mariotte tank. The wetting process was conducted by saturating the column from the base upward to displace air out of the void spaces with the aim to approach complete saturation.

3.2.2 *Measurement of Gaseous Diffusion*

The matrix material was considered fully saturated when standing water ponded at the top of the sample and the moisture-content profile throughout the length column reached steady state. The drying curve was initiated by opening the drainage port at the base of the apparatus.

Saturation was decreased in 5 - 10% intervals. When the moisture content reached equilibrium at a specified saturation the drainage port was closed. The headspace and the sample were then purged with 99.9% $N_{2(g)}$. After the column was flushed with $N_{2(g)}$, one level of eight diffusion ports was opened to provide uniform radial diffusion of atmospheric air into the sample. Moisture content values along the vertical profile of the column were recorded using ECH_2O probes at the time of the experiment. Voltages measured from the SO-110 oxygen sensor were converted to $O_{2(g)}$ concentrations based on ambient air concentrations of $O_{2(g)}$, anaerobic conditions, temperature, and humidity within the headspace. This experimental process was repeated until the drying curve was complete. The wetting curve was initiated by introducing deionized water from the bottom port and the sample was rewet in intervals of 5 - 10% saturation. At desired values of moisture content, one level of ports was opened and an $O_{2(g)}$ breakthrough curve was measured in the headspace.

3.2.3 *Numerical Model Parameters*

A 1-D numerical model, using the reactive transport code MIN3P, was used to derive the appropriate parameters necessary to calculate D_{e_O2} values (Mayer et al., 2002; Molins et al., 2008). The numerical model was implemented using empirically derived parameters from the experimental design and measured properties of the matrix samples. The simulation time was set for 24 hours to correspond with the duration of a single laboratory diffusion experiment. The saturation-diffusion apparatus was represented as a 0.565 m one-dimensional domain to match the total height of the apparatus. The simulation domain was discretized into 1131 x 0.05 cm cells in the z-direction with two distinct zones: the diffusion chamber and the sample chamber. The upper zone of the simulation domain, the diffusion chamber, was assigned a length of 0.17 m and a porosity (ϕ) value of 1.0 to represent the empty void space for $O_{2(g)}$ to accumulate. The

bottom portion was assigned a length of 0.395 m to match the height of the sample chamber. Boundary conditions of the numerical model were set according to the experimental set-up (Fig. 3.2). The initial concentration of $O_{2(g)}$ was set to 2.4×10^{-9} kPa throughout the model domain. Wetting and drying phases were simulated separately using physical properties based on laboratory measured soil-water characteristic curves of each material (Chapter 2). Adjustments to the laboratory measured van Genuchten parameters were required to simulate lower saturation values observed during the diffusion experiment because the effects of evaporation and air-drying were not accounted for during the laboratory SWCC measurements (Table 3.1).

Internal influx boundaries were set at the heights of the diffusion tubes for each of the levels to simulate the bi-directional diffusion of $O_{2(g)}$ into the domain. A reduced-porosity layer was implemented to represent the influx boundaries and simulate diffusion through the perforated tubes, rather than the entire cross-sectional area of the column. The ϕ surrounding the boundary was reduced by the ratio of the area of the tubes to the cross-sectional area of the column (0.17). Decreasing the ϕ effectively reduced the elementary volume of $O_{2(g)}$ diffusion. Gas samples were taken from within the tubes in the column during the experiment to determine the source concentration of $O_{2(g)}$. Based on the measurements, a value of 12.16 kPa for $O_{2(g)}$ was assigned to the internal influx boundaries. The free-air diffusion coefficient (D_a^0) for $O_{2(g)}$ was set to 1.8×10^{-5} m s^{-2} and 2.5×10^{-9} m s^{-2} for gaseous diffusion in the aqueous phase (D_w^0) (Aachib et al., 2002).

The sample chamber domain was sub-divided into four zones, with the locations of the ECHO probes at the center of each zone, to match the moisture-content profile of the matrix material. Each ECH_2O probe reading corresponded to an average moisture content for the specific zone. Moisture content values were adjusted in the MIN3P simulations by changing the

initial head conditions in each zone to correspond to the measured moisture-content value. Full moisture-content profiles for each simulation are included in Appendix B.

Tortuosity values (ranging from 0.0 - 1.0) were adjusted in both the reduced-porosity layer (RPL) and the domain above the input boundary to match the observed O_2 breakthrough curve derived from the experimental data. The values assigned to the RPL were lower than the tortuosity values assigned to the sample to account for the diffusion of $O_{2(g)}$ through the perforations in the tubes and not the entire area of the tube. Tortuosity values assigned to the sample above the input boundary were adjusted between simulations to obtain a visual fit between the breakthrough curves measured experimentally and simulated using MIN3P. The tortuosity values assigned through the curve matching procedure were subsequently used to calculate a corresponding D_{e_O2} value.

3.2.4 *Calculation of Effective Diffusion Coefficients and Sulfide Oxidation Rates*

Effective diffusion coefficients for $O_{2(g)}$ were calculated utilizing the equation incorporated into MIN3P for simulation of gaseous diffusion:

(3.1) $$D_{e\_O2} = D_a^0 \, \theta_a \tau$$

Where D_a^0 is the free-air diffusion coefficient for $O_{2(g)}$ (1.8×10^{-5} m s^{-2}), θ_a is volumetric air content ($m^3\, m^{-3}$), and τ is tortuosity (-) (Mayer et al., 2010). The results of the calibrated simulations were compared to non-linear least squares fitting of the breakthrough curves (Fig. 3.3). The tortuosity values obtained from matching the breakthrough curves, and average θ_a values above the influx boundary, were used to calculate D_{e_O2} values.

Sulfide oxidation rates were calculated using a simple homogeneous oxidation model (Gibson et al., 1994).

(3.2) $$R = \sqrt{2S'C_0 D_{e\_O2}}$$

Where R [kg (O_2) m^3 s^{-1}] is the overall oxidation rate, S' is the intrinsic oxidation rate (IOR; [kg (O_2) m^{-3} s^{-1}]), C_0 [kg m^3] is the atmospheric oxygen concentration, D_{e_O2} [m^2 s^{-1}] is the effective oxygen diffusion coefficient. Values for S' were derived from humidity cell experiments for both of the sites (Table 3.2; SRK Consulting, 2004; Langman et al., 2014).

3.3 Results

3.3.1 *Measured Rates of Oxygen Diffusion in Matrix Material and Calculated Effective Diffusion Coefficients*

Measurements of the rate of $O_{2(g)}$ transport were conducted for saturations ranging from 0.03 to 0.62, with more rapid rates of $O_{2(g)}$ transport observed from less-saturated matrix material (Fig. 3.4). Concentrations of $O_{2(g)}$ were compared after 16 hours because it was the shortest time interval of a diffusion experiment. Rates of $O_{2(g)}$ diffusion were not conducted for saturations greater than 0.70 because water flowed out of the diffusion ports when opened. Trendlines were fit to the measured wetting and drying data, respectively, to observe differences in $O_{2(g)}$ diffusion between wetting and drying phases (Fig. 3.5). A non-linear regression analysis was used to fit to the data for each of the $O_{2(g)}$ breakthrough curves to develop D_{e_O2} estimate for the corresponding saturation measurement (Fig. 3.6). The intercept for the non-linear regression was forced to zero to represent the appropriate initial condition for each experiment (*i.e.*, 0 kPa O_2 at time zero). Values of D_{e_O2} were also estimated from the breakthrough curves using the numerical model MIN3P. The D_{e_O2} values estimated using MIN3P are similar to the values determined through the non-linear regression analysis of the breakthrough curves (Fig. 3.6). The D_{e_O2} values determined by non-linear regression and using MIN3P are in good agreement with the model proposed by Aachib et al. (2002) (Fig. 3.6). Trendlines were fit to the wetting and

drying data respectively to observe differences in $O_{2(g)}$ diffusion between wetting and drying phases. The D_{e_O2} values determined from MIN3P are plotted as a function of pressure-head values from the MIN3P simulations (Eq. 3.1; Fig. 3.7). Effective diffusion coefficients decreased with increasing negative matric suction (ψ) (*i.e.*, increasing saturation)

3.3.3 *Estimated Sulfide Oxidation Rates*

Overall sulfide-oxidation rates (R) are estimated using the simple homogeneous oxidation model (Gibson et al., 1994). The D_{e_O2} values calculated in this study are combined with $S`$ values determined from laboratory experiments conducted on the Diavik materials (Langman et al., 2014) and from $S`$ values for the Faro materials (SRK Consulting, 2004) (Eq. 3.2; Table 3.2; Fig. 3.7). The estimated values of R range from 6×10^{-9} to 1×10^{-7} kg (O_2) m^{-3} s^{-1} and fall within the range of reported literature values between 10^{-11} and 10^{-5} kg (O_2) m^{-3} s^{-1} (Bennett et al., 2000; Lefebvre et al., 2001b; Ritchie, 2003; Vriens et al., 2018). Sulfide-oxidation rates increase with more negative-ψ values for both materials and vary by one order of magnitude across the range of reported ψ (Fig. 3.8).

3.4 Discussion

3.4.1 *Influence of Saturation on Effective Diffusion Coefficients*

Measurements made under wetting and drying conditions, at similar saturation, indicate more rapid diffusion under drying conditions than under wetting conditions. Simulation fit to the Faro material experiment resulted in larger residuals with a least squares difference of 25.75 compared to Diavik material experiment and simulation with a least squares difference of 10.78. Matrix material from Faro was more poorly sorted and coarser than the Diavik material, which

results in greater pore-size variation leading to greater variation in diffusion pathways (Rouf et al. 2012).

Oxygen diffusion is strongly dependent on the moisture content of the material. The measured $O_{2(g)}$ concentration after 16 hours shows an overall reduction in $O_{2(g)}$ concentration with an increase in saturation. Variations in $O_{2(g)}$ concentrations after 16 hours into each diffusion apparatus experiment could be affected by the difference in the level of ports used for diffusion due to variability in the saturation profile and heterogeneity of the matrix material between levels of diffusion ports. Overall, the rates of $O_{2(g)}$ diffusion in the Faro material were on average greater than rates measured from Diavik material across all saturations. This is attributed to Faro matrix material having a larger ϕ (0.3) than Diavik matrix material (0.22) which is associated with a shorter and wider diffusion path causing $O_{2(g)}$ to diffuse more rapidly through the pore spaces. Values of $O_{2(g)}$ concentrations plateau at lower values of saturation as primary diffusion pathways are established leading to less variability in the $O_{2(g)}$ diffusion pathway. Diavik material begins to show a sharp decrease in $O_{2(g)}$ concentrations around a saturation of 0.3. Faro material shows a decline in concentration around 0.3 saturation however the decline is less defined compared to Diavik. The tails of both trendlines approach an $O_{2(g)}$ concentration of 0.0 kPa at high saturations because the diffusion pathway becomes extremely tortuous and diffusion through water-filled voids begins to dominate.

3.4.2 *Variability of Effective Diffusion Coefficients in Matrix Material*

Effective diffusion coefficients for the experimental measurements were calculated using the parameters derived from MIN3P simulations (Fig. 3.7). The range of ψ values corresponded to saturation values ranging from 3 to 62%. Over this range of ψ, calculated D_{e_O2} values varied up to two orders of magnitude for both Faro and Diavik matrix materials. The trend in calculated

D_{e_O2} values is consistent with a strong dependence on moisture content (Aachib et al. 2002; Collin and Rasmuson; 1988; Millington and Shearer, 1971). At near-zero ψ values, pore spaces are water-filled creating discontinuities between the air-filled gas diffusion pathways. As negative ψ increases, the pore spaces drain, creating greater continuity between air-filled pores. Around a ψ value of -5.0 m, the rate of increase in D_{e_O2} is slowed due to preferential diffusion pathways at low saturation values. The decline in the rate of increase in D_{e_O2} values was also reflected in the measured $O_{2(g)}$ concentrations that plateaued at low values of saturation.

Effective diffusion coefficients were calculated for both wetting and drying phases of waste-rock matrix material to assess the influence of hysteresis on $O_{2(g)}$ diffusion (Fig 3.7). Calculated D_{e_O2} values showed no observable differences between wetting and drying phases for the range of ψ values measured in this study. The D_{e_O2} values determined using the saturation-diffusion apparatus and MIN3P model calculations showed good agreement with the D_{e_O2} values estimated from SWCC measurements over the range of ψ from -0.5 m to -38 m and saturations from 0.03 to 0.63 (Chapter 2; Fig. 3.9). The greatest difference in estimated D_{e_O2} values occurred at near-zero values of negative ψ, which reflect high degrees of saturation. These saturation levels were not attained from the saturation-diffusion apparatus due to limitations in the experimental design, which restricted the potential for measurements at high degrees of saturation (> 0.70). Calculated values of D_{e_O2} at higher negative pressures, corresponding to lower moisture contents, were attained using the saturation-diffusion apparatus relative to the values estimated from the SWCC measurements because air drying and evaporation of samples contained in the saturation-diffusion apparatus provided lower moisture contents than were available from SWCC measurements.

The moisture-content profile of a waste-rock pile depends on the local climate and heterogeneity of the waste rock. Generally, moisture content in a waste-rock pile increases with depth from the surface (Blowes, 1997). Based on the results of this study, zones of lower moisture content will generally have more rapid rates of $O_{2(g)}$ diffusion and lower variability in D_{e_O2}. Preferential diffusion pathways of $O_{2(g)}$ are established throughout the coarser zones of the matrix material because the residual moisture content is retained only in the non-interconnected pore spaces of finer-grainer matrix due to capillary forces. Variability in D_{e_O2} values increase near complete saturation due to elimination of preferential pathways and discontinuities in the air-filled pathway caused by water-filled voids.

The influence of hysteresis is anticipated in the near-zero values of ψ, which reflect the zone of tension saturation (capillary fringe) of a waste-rock pile. Moisture content from the water table can be redistributed upwards through the matrix material resulting in a more extensive zone of tension saturation within the finer particle-size portion. Fluctuations in the height of the water table are dependent on the quantity of infiltration and the infiltration rate (Smith et al., 1995). Small changes in moisture content greatly impact the continuity of the air-filled pathway at high degrees of saturation. Based on the results of this study, substantial differences in D_{e_O2} values between wetting and drying phases can occur at near-zero values of ψ corresponding to high saturations. This result is consistent with previous studies and numerous diffusion coefficient models have illustrated the more rapid increase in D_e with smaller decreases in moisture content at high degrees of saturation (Aachib et al. 2002; Collin and Rasmuson; 1988; Millington and Shearer, 1971). The difference in D_{e_O2} values between wetting and drying phases is the result of large differences in saturation between phases, where full saturation is not achieved by rewetting due to entrapped air (Rouf et al., 2012). Molecular diffusion through air-filled voids is the most

important mechanism for diffusive $O_{2(g)}$ transport in porous media (Curie, 1962; Collin and Rasmuson, 1981; Millington and Shearer, 1971; Elberling et al., 1994; Nicholson et al., 1989).

3.4.3 *The Influence of Hysteresis on Sulfide Oxidation Rates in Waste Rock*

Several studies have concluded that the sulfide-oxidation rate in a waste-rock pile is controlled by the D_{e_O2} of the material which is inversely proportional to the local moisture content (Collin and Rasmuson, 1988; Elberling et al., 1994; Blowes, 1997; Molson et al., 2005; Gunsinger et al., 2006). Higher moisture contents, corresponding with more negative-ψ values, result in a slower rate of $O_{2(g)}$ diffusion. In turn, less $O_{2(g)}$ is available to oxidize sulfide minerals. Based on the results of this study, higher R values are estimated in shallower, less saturated, zones of waste rock, where more rapid rates of $O_{2(g)}$ diffusion are expected. As sulfide minerals within the shallow portion of waste rock are consumed, the rate of sulfide oxidation decreases with depth due to longer diffusion distance and higher moisture content (Elberling et al., 1994; Blowes, 1997).

Matrix material from Faro is estimated to have higher R values compared to Diavik material because of a greater IOR and larger ϕ contributing to more rapid rates of $O_{2(g)}$ diffusion (Table 3.2; Fig. 3.8). Faro material exhibited a smaller ψ range corresponding to the same saturation range for Diavik material because the coarser-textured material produced lower saturation values at less-negative pressures. Estimated R values from calculated D_{e_O2} values using the saturation-diffusion apparatus were compared to R values estimated from D_{e_O2} values determined from SWCC measurements (Chapter 2; Fig. 3.10). The comparison between these two methods shows good agreement for the range of ψ values determined from numerical modeling. Estimated R values show negligible differences between wetting and drying curves for the ψ range (-0.5 m to -40 m) measured using the saturation-diffusion apparatus.

3.5 Conclusions

Laboratory measurements of diffusive rates of $O_{2(g)}$ through variably-saturated matrix material were completed using the saturation-diffusion apparatus. An inverse relationship exists between measured $O_{2(g)}$ concentrations in the headspace of the apparatus and the moisture content of the matrix material. On average, the coarser matrix material from Faro displayed higher concentrations of $O_{2(g)}$ in the headspace after 16 hours relative to Diavik matrix material, reflecting more rapid rates of $O_{2(g)}$ diffusion.

Parameters derived from SWCC measurements (Chapter 2) provide an adequate estimation of D_{e_O2} values in mine-waste matrix material. However, the effects of evaporation and air drying on *in situ* mine-waste matrix material were not included in SWCC measurements because these mechanisms would result in saturation values below residual saturation. The effect of reducing the moisture content below residual saturation had a minimal influence on D_{e_O2} values because preferential $O_{2(g)}$ diffusion pathways were established within the matrix material. Increasing saturation values above residual reflects an increase in tortuosity of the air-filled diffusion pathway resulting in a decrease in $O_{2(g)}$ concentration in the headspace.

Sulfide oxidation rates determined from reactive transport simulation derived D_{e_O2} values, corresponding to laboratory diffusion tests, show reasonable agreement to R values determined from D_{e_O2} values estimated from SWCC measurements (Chapter 2). Higher estimated R values are anticipated in conjunction with more negative-ψ values, corresponding to lower moisture contents. Estimated R values determined for the coarser Faro matrix material had approximately one order of magnitude greater than R values estimated for the matrix material from Diavik.

The effect of hysteresis on both numerically calculated D_{e_O2} values and resulting estimated R values was found to be minimal for the range of ψ values examined in this study. The potential for the influence of hysteresis on R values occurs at higher saturations, where greater variations in D_{e_O2} values are estimated. Estimated R values corresponding to near-zero ψ reflect the potential effect of hysteresis. Overall, the effect of hysteresis was not experimentally observed over the range of ψ measured for either matrix materials, indicating that the effect of hysteresis on inter-particle diffusion coefficients in mine waste-rock matrix material was negligible within regions of low moisture content and high-negative ψ.

FIGURES

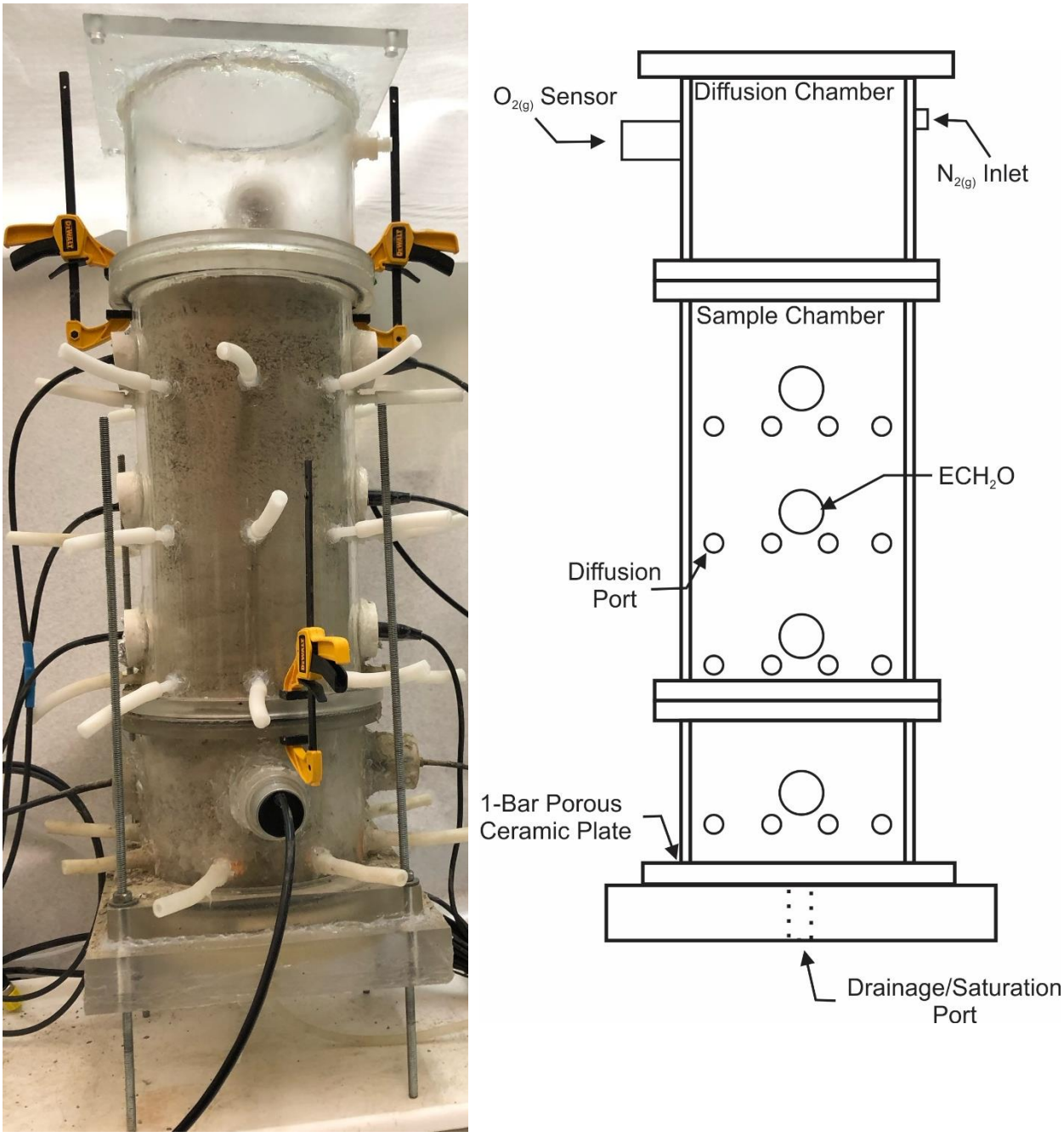

Fig. 3.1 Laboratory saturation-diffusion apparatus used to measure diffusive rates of $O_{2(g)}$ through variably saturated mine waste-rock matrix material.

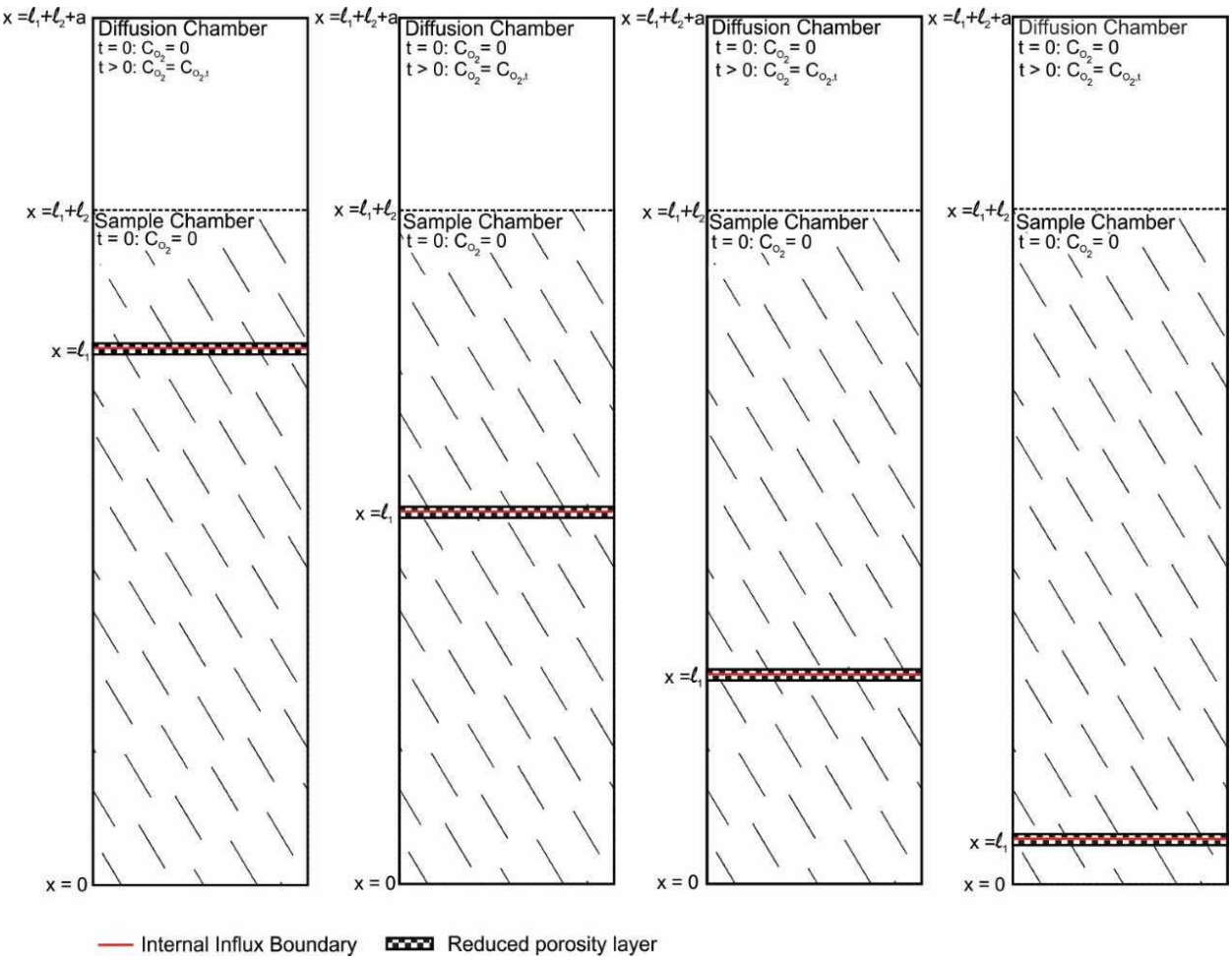

Fig. 3.2 Conceptual model for the 1-D numerical model used to calculate effective diffusion coefficients.

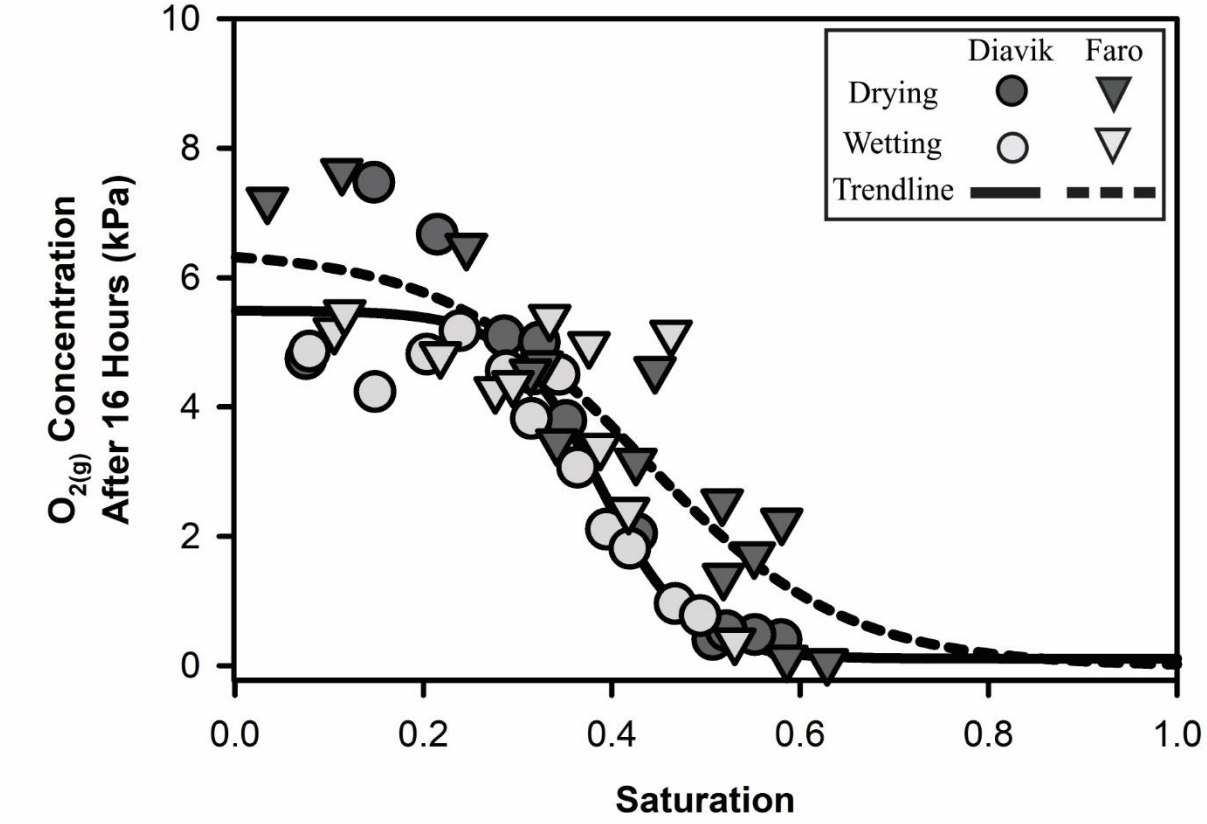

Fig. 3.3 Oxygen gas concentrations measured in the headspace after 16 hours of diffusion.

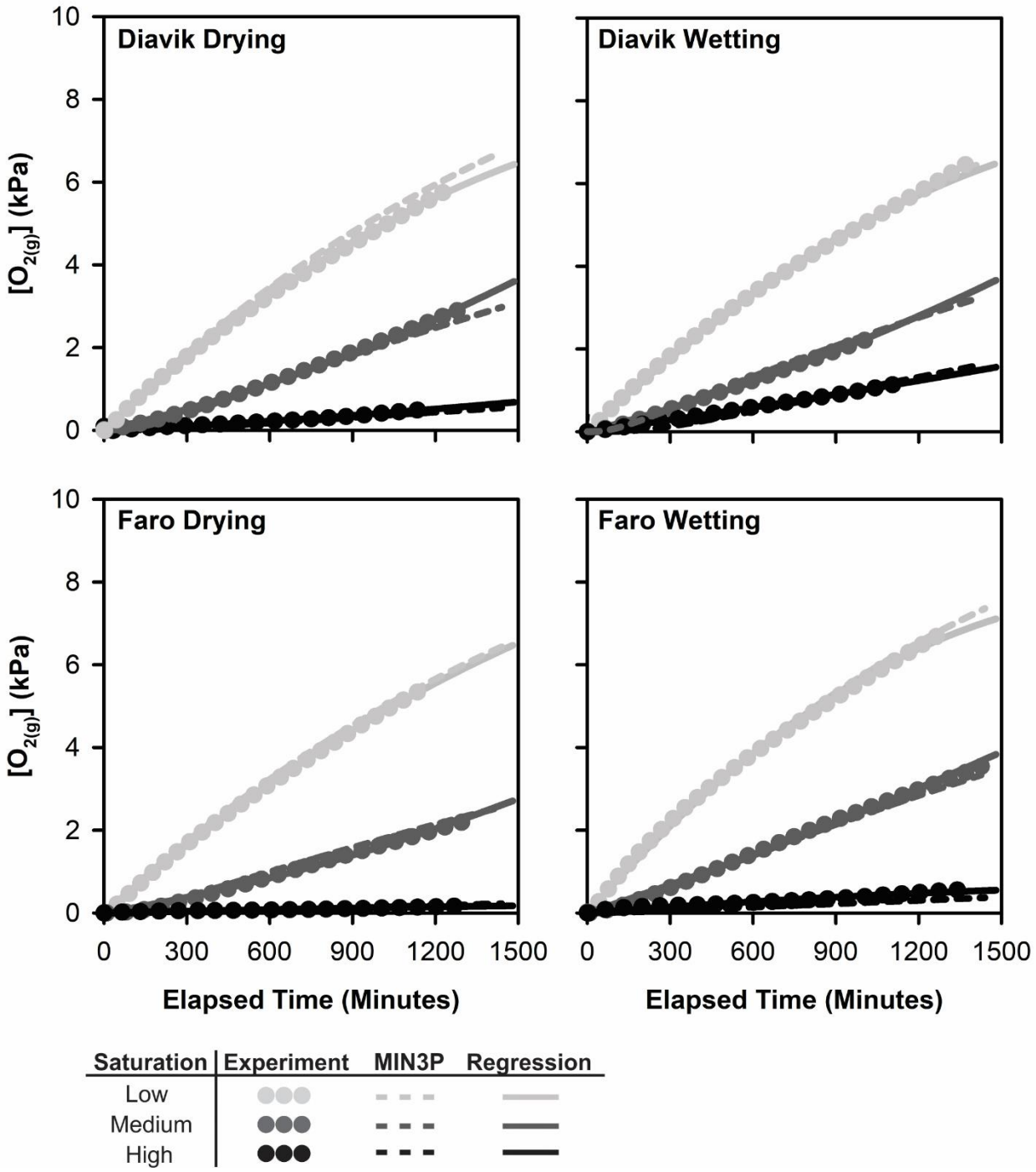

Fig. 3.4 Comparison of measured breakthrough curves to MIN3P simulated and non-linear regression analysis breakthrough curves for high, medium and low-saturation matrix material.

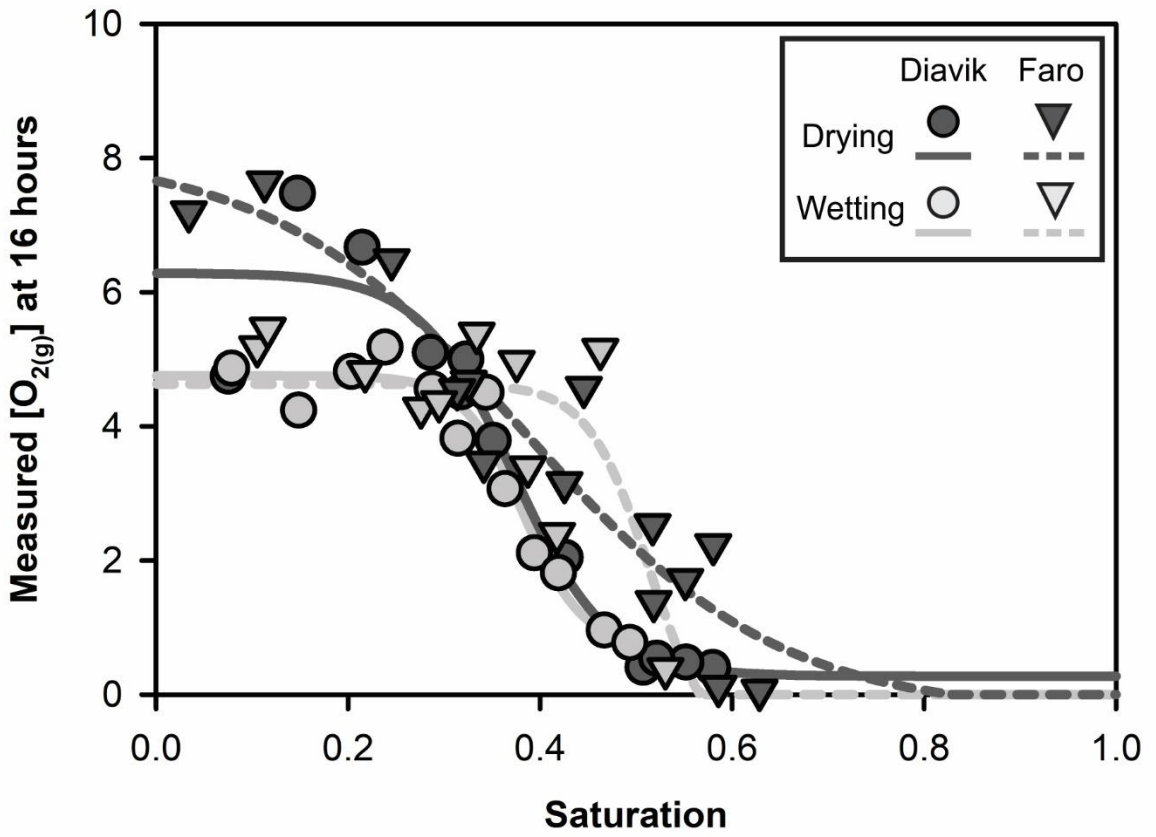

Fig. 3.5 Oxygen gas concentrations measured in the headspace after 16 hours of diffusion. Trendlines were fit to the wetting and drying data respectively to observe differences in $O_{2(g)}$ diffusion between wetting and drying phases.

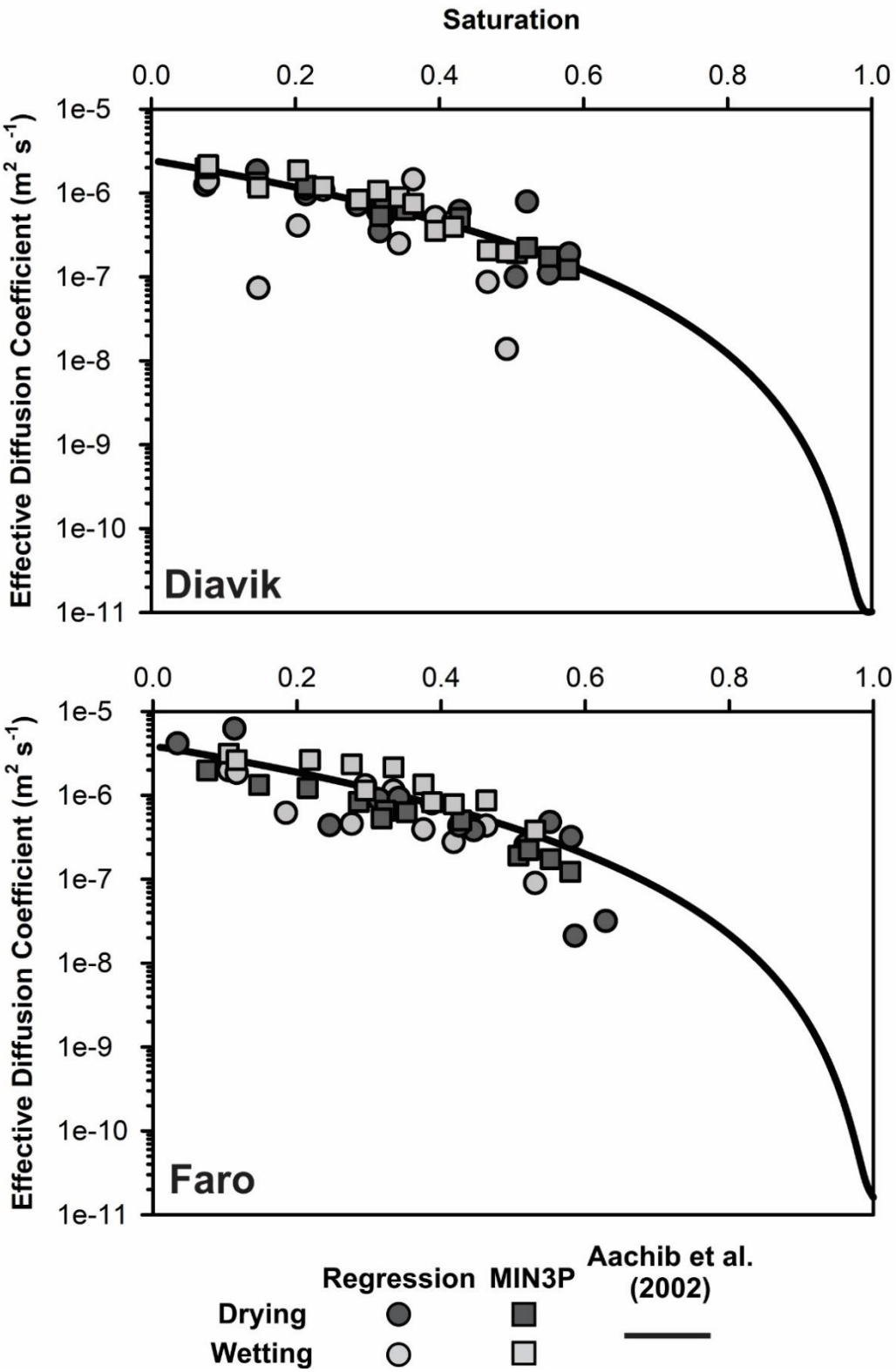

Fig. 3.6 D_{e_O2} values determined from MIN3P parameters compared to D_{e_O2} values from non-linear regression analysis and the Aachib et al. (2002) model.

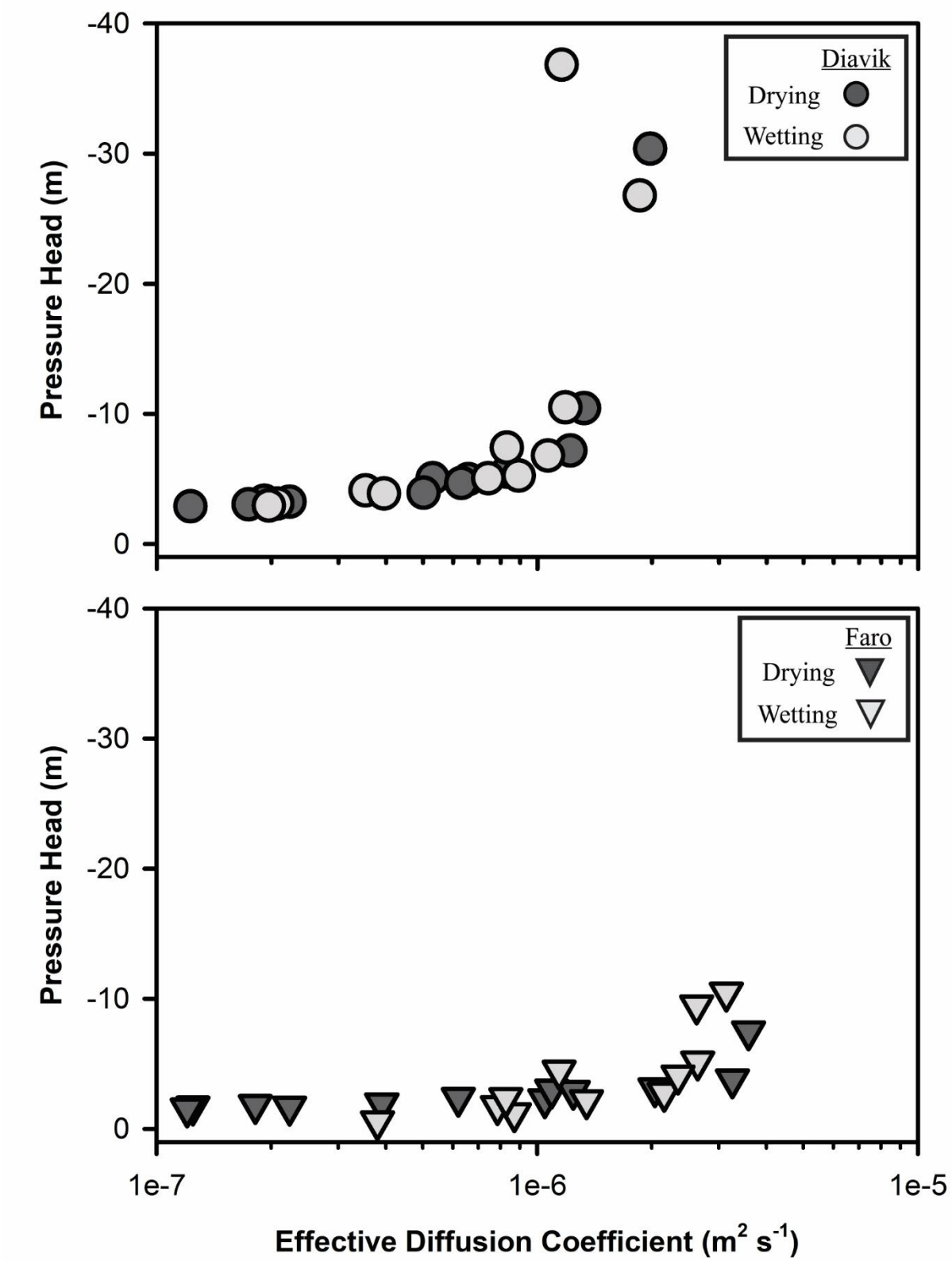

Fig. 3.7 Numerically calculated D_{e_O2} values as a function of ψ.

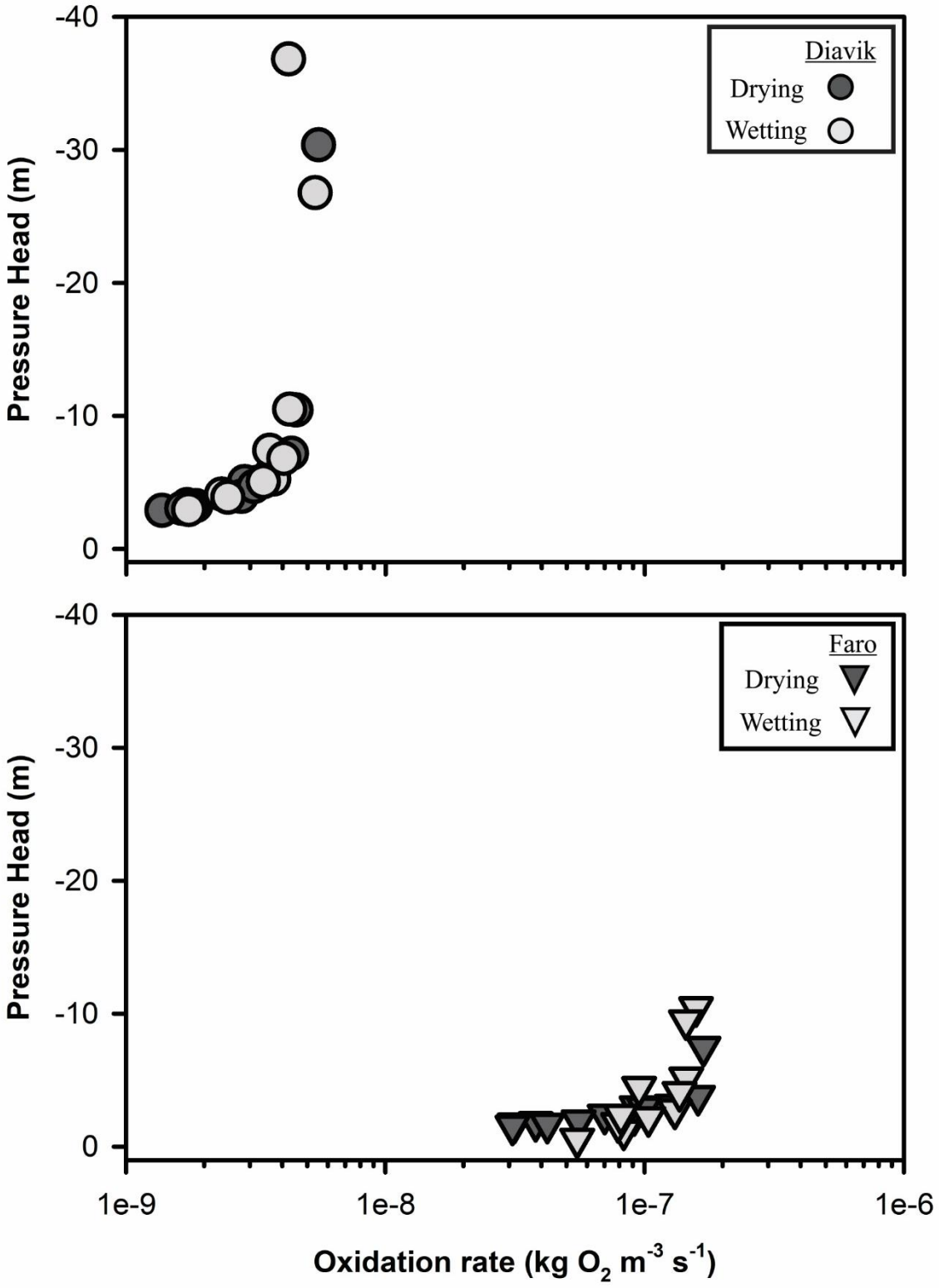

Fig. 3.8 Estimated *R* values based on calculated D_{e_O2} values.

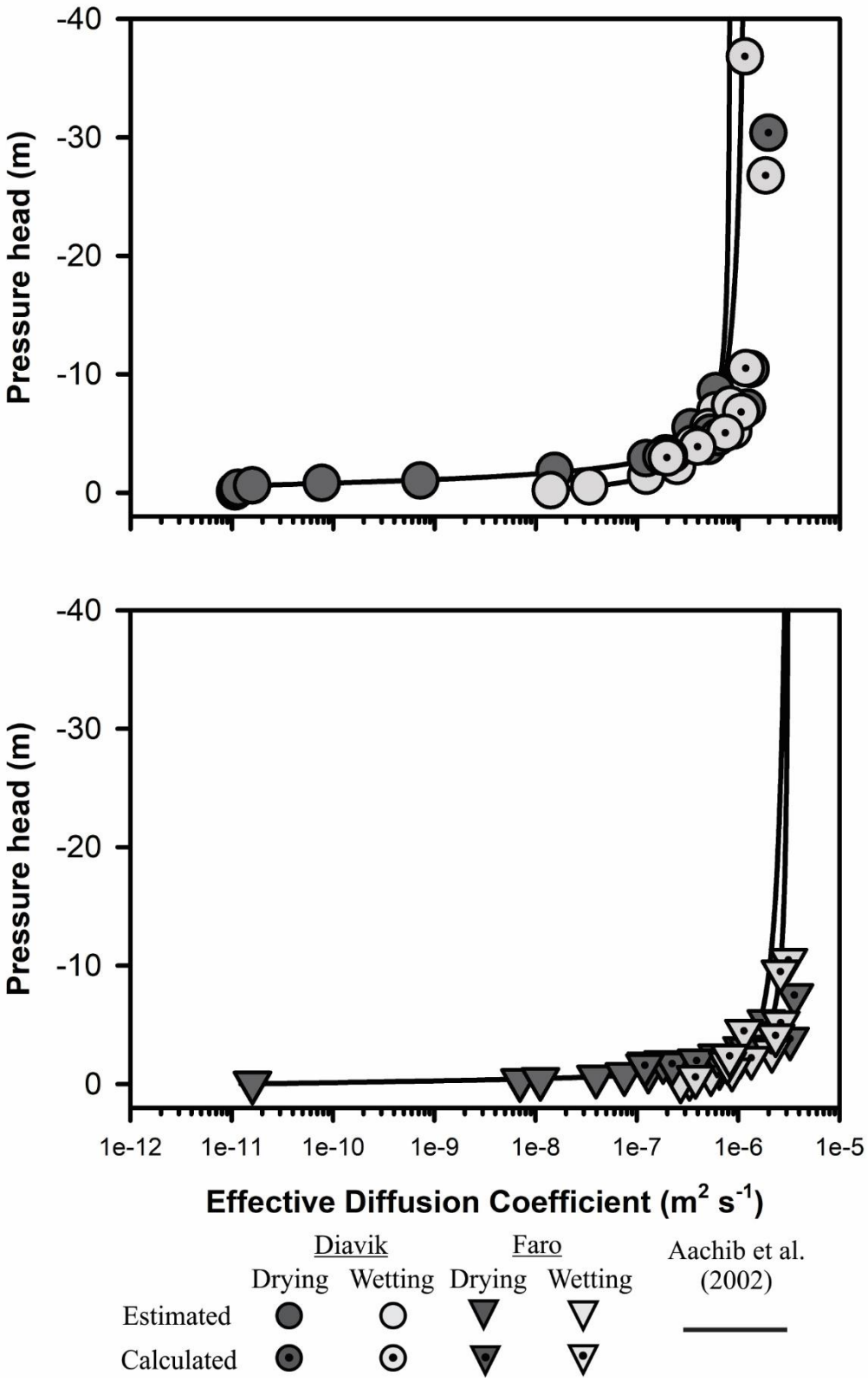

Fig. 3.9 Comparison between numerically calculated D_{e_O2} values using the saturation diffusion apparatus and D_{e_O2} values estimated from SWCC parameters determined in chapter 2.

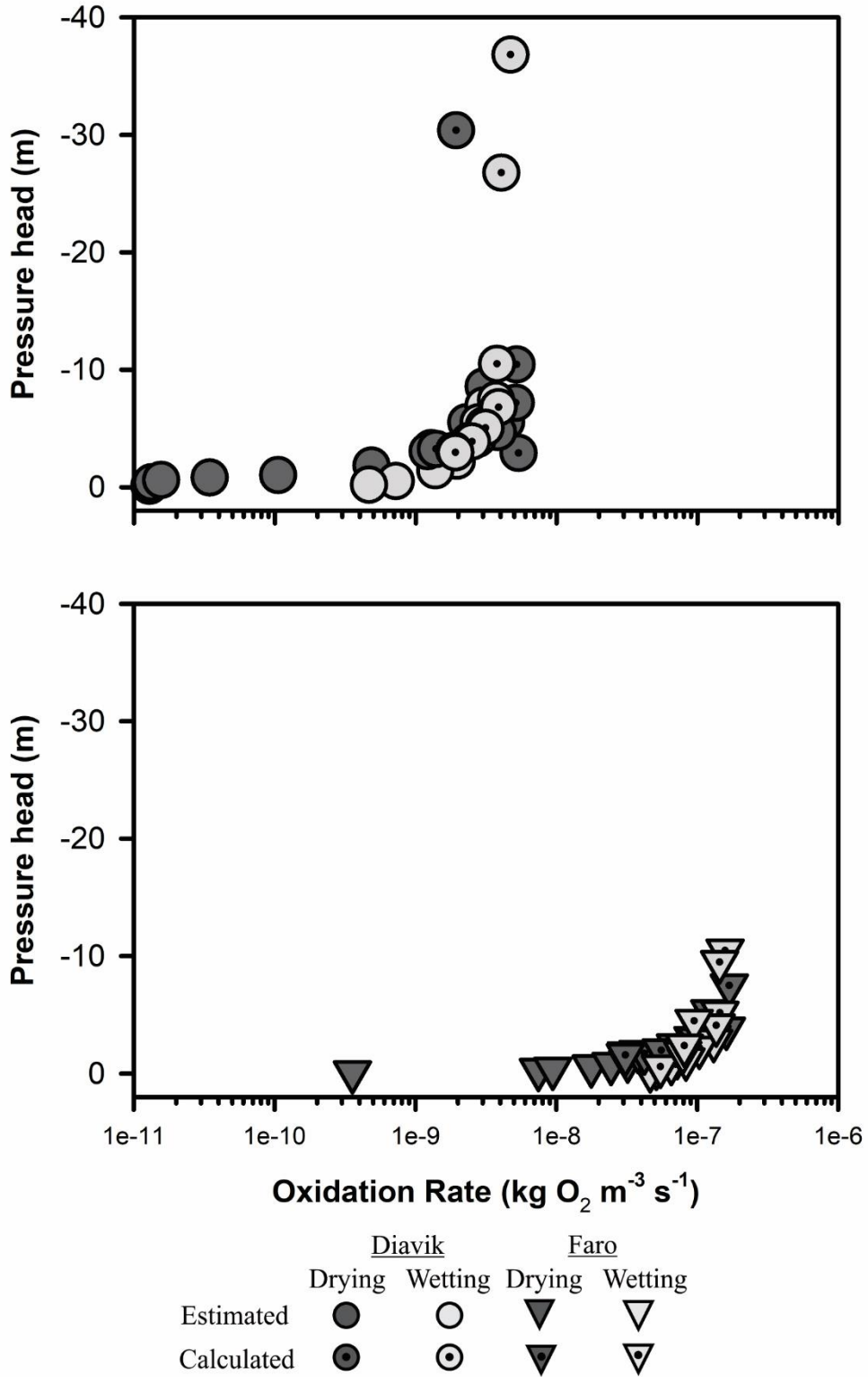

Fig. 3.10 Comparison of *R* values based on calculated D_{e_O2} values from the saturation-diffusion apparatus and *R* values estimated from D_{e_O2} values determined from measured SWCCs (Chapter 2).

TABLES

Table 3.1 Adjusted van Genuchten parameters used in MIN3P compared to van Genuchten parameters fit to soil-water characteristic curve measurements.

Parameter	Diavik				Faro			
	Measured		Adjusted		Measured		Adjusted	
	Drying	Wetting	Drying	Wetting	Drying	Wetting	Drying	Wetting
θ_r	0.063	0.032	0.001	0.001	1.60E-02	3.00E-06	1.60E-02	2.00E-02
α	0.054	0.114	50	1.114	0.142	0.182	0.650	0.182
n	2.64	1.60	2.64	1.60	1.95	1.31	2.50	3.25

Table 3.2 Parameters used to calculate overall oxidation rate using a simple homogeneous oxidation model (Gibson et al., 1994).

Parameter	Diavik	Faro
S' (kg (O_2) m^3 s^{-1})	1.7×10^{-9}	1.5×10^{-7}
C_0 (kg m^3)	0.265	0.265
D_{e_O2} (m^2 s^{-1})	1×10^{-7} to 2×10^{-6}	1×10^{-7} to 4×10^{-6}
n	1	1

CHAPTER 4

CONCLUSIONS

4.1 Conclusions

The *in situ* characterization of mine wastes is complicated by diverse mineralogy, variable climate and structural heterogeneity within the pile. Laboratory characterization techniques provide a more cost effective and controlled environment for the determination of empirical parameters used to model the rate and extent of AMD. Waste-rock matrix material (<4.75 mm in particle diameter) is associated with an increased surface area of sulfide minerals and longer residences times of water due to capillary forces that result in a greater release of sulfates and metal(loid)s and increased solute loadings in porewater. The research presented in this study focused on the unsaturated characterization of waste-rock matrix material from three mine sites: Faro Mine Complex, YT; the Detour Lake Gold Mine, ON; and Diavik Diamond Mine, NT.

Particle-size analysis and measurement of SWCCs were completed for the waste-rock matrix materials to evaluate the impact of particle-size distribution on SWCC morphology and the degree of hysteresis in the matrix material from waste-rock piles. The matrix materials were classified as poorly-sorted materials with ϕ values ranging from 0.22 to 0.30. Soil-water characteristic curves ranging up to 100 kPa were measured using Tempe cells and were fit with models proposed by van Genuchten (1980) and Fredlund & Xing (1994) which provided excellent fits to the SWCC data for waste-rock matrix material. The maximum difference in θ between the wetting and drying stages ranged between 0.047 [m^3m^{-3}] for Detour matrix material and 0.135 [m^3m^{-3}] for Faro matrix material. Diavik and Faro matrix materials were determined to

have greater degrees of hysteresis (*r*) values than the more poorly-sorted finer-grained matrix material from Detour. Calculated *r* values for the matrix materials were close to and outside the upper range of *r* values determined for six soils by Konyai (2009). The results show that waste-rock matrix material has the potential to be strongly hysteretic, resulting in large variability in moisture content between wetting and drying stages.

Rates of $O_{2(g)}$ diffusion through variably-saturated waste-rock matrix material were measured using a laboratory saturation-diffusion apparatus. Measured $O_{2(g)}$ concentrations after 16 hours of diffusion were fit with trendlines following a non-linear regression analysis. The trendline illustrated the effect of moisture content on $O_{2(g)}$ diffusion, where lower moisture content corresponded to more rapid rates of diffusion. The trendline fit to the Faro matrix material indicated greater $O_{2(g)}$ concentrations across the range of measured moisture contents compared to Diavik matrix material.

Experimentally measured $O_{2(g)}$ breakthrough curves were numerically modeled using the reactive transport code of MIN3P to derive D_{e_O2} values. Calculated D_{e_O2} values for both wetting and drying curves were compared with D_{e_O2} values estimated from parameters derived from SWCC measurements and show good agreement. The trends of both the estimated and calculated D_{e_O2} values correspond to the trend of the measured $O_{2(g)}$ concentrations, where lower D_{e_O2} values reflect higher moisture contents and lower negative ψ values. The trend shows that D_{e_O2} values change more rapidly in response to changes in moisture content at near-zero values of ψ compared to D_{e_O2} values at higher negative ψ.

Sulfide oxidation rates were estimated using a simple homogeneous oxidation model (Gibson et al., 1994) implementing both the calculated and estimated D_{e_O2} values. Estimated *R* values follow a similar trend to the D_{e_O2} values, reflecting the importance of determining D_{e_O2}

values in mine wastes. The results from these studies indicate that the effect of hysteresis on D_{e_O2} values and R values is negligible within low moisture content / high negative ψ zones of mine waste. The potential for hysteretic impact on D_{e_O2} values and R values is estimated to occur in near-zero values of ψ; where the degree of hysteresis is the greatest and changes in moisture content have a greater effect on D_{e_O2} values.

4.2 Considerations for Future Work

- Gaseous diffusion could instead be measured with an inert gas to limit the effect of sulfide oxidation on $O_{2(g)}$ concentrations in the headspace. Oxygen consumption tests were run for Diavik and Faro matrix materials and the decline of $O_{2(g)}$ over a 24-hour period was found to be minimal, however, $O_{2(g)}$ consumption tests using the Detour material indicate significant rates of $O_{2(g)}$ depletion.
- Implementation of a constant boundary for diffusion open to the atmosphere instead of randomly perforated tubes.
- A smaller-diameter column to reduce the amount of pumping and pressure required to obtain lower moisture contents.
- Measure diffusion rates at high degrees of saturation for both curves to observe if there is a hysteretic effect.
- Additional SWCC measurements to better characterize waste-rock matrix material.
- Higher pressure SWCC measurements to measure residual saturation of the matrix materials.

REFERENCES

Aachib, M., Aubertin, M., and Mbonimpa, M. 2002. Laboratory measurements and predictive equations for gas diffusion coefficient of unsaturated soils. In Proceedings of the 55th Canadian Geotechnical Conference and the 3rd Joint IAH–CNC and CGSGroundwater Speciality Conference, Niagara Falls, October 2002.Edited by D. Stolle, A.R. Pigott, and J.J. Crauder. pp. 163–171.

Aachib, M., Mbonimpa, M., and Aubertin, M. 2004. Measurement and prediction of the oxygen diffusion coefficient in unsaturated media, with applications to soil covers. Water, Air, and Soil Pollution, **156**(1): 163-193.

Amos, R. T., Blowes, D. W., Bailey, B. L., Sego, D. C., Smith, L., and Ritchie, A. 2015. Waste-rock hydrogeology and geochemistry. Applied Geochemistry, **57**: 140-156.

Apogee Instruments Owner's Manual. 2020. Apogee Instruments Owner's Manual Oxygen Sensor; Models SO-110, SO-120, SO-210, SO-220. Apogee Instruments Inc. Logan, Utah.

ASTM. 2006. Standard Practice for Classification of Soils for Engineering Purposes (Unified Soil Classification System. ASTM Standard D2487-06. ASTM International, West Conshohocken, PA.

ASTM. 2016. Standard test method for determination of the soil water characteristic curve for desorption using hanging column, pressure extractor, chilled mirror hygrometer, or centrifuge. ASTM standard D6836-16. ASTM International, West Conshohocken, PA. doi:10.1520/D6836-16.

ASTM. 2017. Standard Test Methods for Particle-Size Distribution (Gradation) of Soils Using Sieve Analysis. ASTM standard D6913/D6913M-17. ASTM International, West Conshohocken, PA. doi:10.1520/D6913_D6913M-17.

Aubertin, M., Ricard, J.F., and Chapuis, R.P. 1998. A predictive model for the water retention curve: application to tailings from hard-rock mines. Canadian Geotechnical Journal, **35**(1): 55–69. doi:10.1139/t97-080.

Aubertin, M., Mbonimpa, M., Bussière, B., and Chapuis, R.P. 2003. A model to predict the water retention curve from basic geotechnical properties. Canadian Geotechnical Journal, **40**(6): 1104–1122. doi:10.1139/t03-054.

Aung, K.K., Rahardjo, H., Leong, E.C., and Toll, D.G. 2001. Relationship between porosimetry measurement and soil-water characteristic curve for an unsaturated residual soil. Geotechnical and Geological Engineering, **19**(3–4): 401–416. doi:10.1023/A:1013125600962.

Azam, S., Wilson, W.G., Herasymuik, G., Nichol, C., and Barbour, L.S. 2007. Hydrogeological behaviour of an unsaturated waste rock pile: A case study at the Golden Sunlight Mine, Montana, USA. Bulletin of Engineering Geology and the Environment, **66**(3): 259–268. doi:10.1007/s10064-006-0077-7.

Azmi, M., Ramli, M.H., Hezmi, M.A., Mohd Yusoff, S.A.N., and Alel, M.N.A. 2019. Estimation of Soil Water Characteristic Curves (SWCC) of mining sand using soil suction modelling. In IOP Conference Series: Materials Science and Engineering, **527**(1). doi:10.1088/1757-899X/527/1/012016.

Bao, Z., Blowes, D. W., Ptacek, C. J., Bain, J., Holland, S. P., Wilson, D. et al. 2020. Faro Waste Rock Project: Characterizing variably saturated flow behavior through full-scale waste-

rock dumps in the continental subarctic region of Northern Canada using field measurements and stable isotopes of water. Water Resources Research, **56**(3). doi:10.1029/2019WR026374.

Barbour, S. L. 1998. The soil-water characteristic curve: a historical perspective. Canadian Geotechnical Journal, **35**(5): 873–894. doi:10.1139/t98-040.

Bennett, J.W., M.J. Comarmond, and J.J. Jeffery. 2000. Comparison of oxidation rates of sulfidic mine wastes measured in the laboratory and field. Aust. Ctr. Min. Environ. Res., Kenmore, QLD, Australia.

Benson, C. H., Chiang, I., Chalermyanont, T., and Sawangsuriya, A. 2014. Estimating van Genuchten Parameters α and n for Clean Sands from Particle Size Distribution Data, **1**(1): 410–427. doi:10.1061/9780784413265.033.

Blowes, D. W. 1997. The Environmental Effects of Mine Wastes. Mapping and Monitoring the Mine Environment In Proceedings of Exploration, **97**: 887-892.

Blowes, D.W., and Jambor, J.L. 1990. The pore-water geochemistry and the mineralogy of the vadose zone of sulfide tailings, Waite Amulet, Quebec, Canada. Appl. Geochem. **5**: 327–346.

Blowes, D.W. and Logsdon, M.J. 1988. Diavik Geochemistry Baseline Report; Canadian Environmental Assessment Agency: Ottawa, ON, Canada.

Brooks, R.H., and A.T. Corey, 1964. Hydraulic properties of porous media, Hydrology Papers, No.3, Colorado State University, Fort Collins, Colorado.

Cash, A. 2014. Structural and hydrologic characterization of two historic waste rock piles. University of Alberta: Msc dissertation.

Collin, M., and Rasmuson, A. 1988. A comparison of gas diffusivity models for unsaturated porous media, Soil Science Society America Journal, **52**: 1559-1565.

Curie, J. A. 1961. Gaseous Diffusion in Porous Media. Part 3. Wet granular materials. Br. Jr. Appl. Phys. **12**:275-281.

Davies, G.B., Ritchie, A.I.M. 1986. A model of oxidation in pyritic mine wastes: I. Equations and approximated solutions. Appl. Math. Model. **10**: 314–322.

Demers, I., Bussiére, B., Mbonimpa, M., and Benzaazoua, M. 2009. Oxygen diffusion and consumption in low-sulphide tailings covers. Canadian Geotechnical Journal, **46**(4): 454–469. doi:10.1139/T08-132.

Demers, I., J. Molson, B. Bussière, and D. Laflamme. 2013. Numerical modeling of contaminated neutral drainage from a waste-rock field test cell. Appl. Geochem. **33**:346–356. doi:10.1016/j.apgeochem.2013.02.025.

Dettrick, D., Costelloe, J., Arora, M., and Yuen, S. 2019. A comparison of measured and predicted diffusion coefficients applied to sand and silt sized acid mine drainage materials. Journal of Environmental Management, **231**: 1106-1116. doi:10.1016/j.jenvman.2018.08.011.

Elberling, B., Nicholson, R.V., Reardon, E.J., and Tibble, P. 1994. Evaluation of sulphide oxidation rates: a laboratory study com-paring oxygen fluxes and rates of oxidation product release. Canadian Geotechnical Journal, **31**: 375–383.

Ellithy, G. 2017. A Spreadsheet for Estimating Soil Water Characteristic Curves (SWCC). May 2017. ERDC/GSL TN-17-1.

Folk, R.L., and Ward, W.C., 1957. Brazos River Bar: a study in the significance of grain size parameters. J. Sediment. Petrol, **27**: 3–26.

Fredlund, D.G. 2019. State of practice for use of the soil-water characteristic curve (SWCC) in geotechnical engineering. Canadian Geotechnical Journal, **56**: 1059-1069: doi:10.1139/cgj-2018-0434.

Fredlund, D. G., and Rahardjo, H. 1993. Soil Mechanics for Unsaturated Soils: John Wiley & Sons.

Fredlund, D.G., and Xing, A. 1994. Equations for the soil-water characteristic curve. Canadian Geotechnical Journal, **31**: 521–532. doi:10.1139/t94-061.

Fredlund, D. G., Rahardjo, H., and Fredlund, M. D. 2012. Soil-Water Characteristic Curves for Unsaturated Soils. Unsaturated Soil Mechanics in Engineering Practice, 184–272. doi:10.1002/9781118280492.ch5.

Fredlund, M.D., Wilson, G.W., and Fredlund, D.G. 2002. Use of the grain-size distribution for estimation of the soil-water characteristic curve. Canadian Geotechnical Journal, **39**(5): 1103–1117. doi:10.1139/t02-049.

Gallage, C. P. K., and Uchimura, T. 2010. Effects of dry density and grain size distribution on soil-water characteristic curves of sandy soils. Soils and Foundations, **50**(1): 161–172. doi:10.3208/sandf.50.161.

Gallage, C., Kodikara, J., and Uchimura, T. 2013. Laboratory measurement of hydraulic conductivity functions of two unsaturated sandy soils during drying and wetting processes. Soils and Foundations, **53**(3): 417-430. doi:10.1016/j.sandf.2013.04.004.

Gebrenegus, T., and Ghezzehei, T.A. 2011. An Index for Degree of Hysteresis in Water Retention. Soil Science Society of America Journal, **75**(6): 2122–2127. doi:10.2136/sssaj2011.0082n.

Geo-Slope. 2012. Seepage modeling with SEEP/W, an engineering methodology. Calgary, Alberta, Canada.

Gibson, D. K., Pantelis, G., and Ritchie, A. I. M. 1994. The Relevance of the Intrinsic Oxidation Rate to the Evolution of Polluted Drainage from a Pyritic Waste Rock Dump. Journal American Society of Mining and Reclamation, 1994(2): 258–264. doi:10.21000/jasmr94020258.

Godin, E. 1991. Canadian Minerals Yearbook—Review and Outlook. Energy, Mines and Resources, Ottawa, Canada

Gunsinger, M.R., Ptacek, C.J., Blowes, D.W., and Jambor, J.L. 2006. Evaluation of long-term sulfide oxidation processes within pyrrhotite-rich tailings, Lynn Lake, Manitoba. Journal of Contaminant Hydrology, **83**(3-4): 149-170. doi:10.1016/j.jconhyd.2005.10.013.

Henry, W. 1803. Experiments on the quantity of gases absorbed by water, at different temperatures and under different pressures. Philosophical Transactions of the Royal Society of London, **93**(0), 29.

Horvath, J. 2011. Development and Implementation of a Closure and Remediation Plan: A Case Study of the Faro Mine Closure Project, YT.

Huang, Y. 1994. Effects of Suction on Strength and Deformation Behavior of Unsaturated Collapsible Soils. Ph.D. Thesis, University of Tokyo, Japan.

Jambor, J. L. 1997. Mineralogy of the Diavik Lac de Gras Kimberlites and Host Rocks. Prepared by Leslie Investment Ltd. For Diavik Diamond Mines Ltd and Environmental Assessment Agency, 187. Ottawa, ON, Canada.

Jensen, Ingrid. “Weather Statistics for Detour Lake.” Yr.no, Norwegian Meteorological Institute and Norwegian Broadcasting Corporatio, 2018. www.yr.no/place/Canada/Ontario/Detour_Lake~5938325/statistics.html.

Jones, S. B., Or, D., and Bingham, G. E. 2003. Gas Diffusion Measurement and Modeling in Coarse-Textured Porous Media. Vadose Zone Journal, **2**: 602-610.

Konyai, S., Sriboonlue, V., and Trelo-Ges, V. 2009. The Effect of Air Entry Values on Hysteresis of Water Retention Curve in Saline Soil. In American Journal of Environmental Sciences, **5**(3): 341-345.

Kovács, C. 1981. “Seepage Hydraulics.” *Elsevier Science Publishers*, Amsterdam.

Langman, J. B., Moore, M. L., Ptacek, C. J., Smith, L., Sego, D., and Blowes, D. W. 2014. Diavik waste rock project: Evolution of mineral weathering, element release, and acid generation and neutralization during a five-year humidity cell experiment. Minerals, **4**(2): 257–278. doi:10.3390/min4020257.

Lau, S. 2016. Investigating Gas Diffusivities at Varying Saturation Conditions in Waste Rock from the Diavik Diamond Mine, NWT, Canada. Undergraduate Thesis, University of Waterloo, Waterloo, ON, Canada.

Lefebvre, R., D. Hockley, J. Smolensky, and A. Lamontagne. 2001b. Multiphase transfer processes in waste rock piles producing acid mine drainage: 2. Applications of numerical simulation. J. Contam. Hydrol, **52**: 165–186. doi:10.1016/S0169-7722(01)00157-7.

Maqsoud, A., Bussière, B., Aubertin, M., and Mbonimpa, M. 2006. Modification of the predictive MK model to integrate hysteresis of the water retention curve. In Unsaturated

Soils 2006: Proceedings of the Fourth International Conference on Unsaturated Soils, Carefree, Arizona, 2–6 April 2006.

Maqsoud, A., Bussiere, B., Aubertin, M., and Mbonimpa, M. 2012. Predicting hysteresis of the water retention curve from basic properties of granular soils. Geotech. Geol. Eng., **30**(5), 1147–1159.

Martin, V., Aubertin, M., Bussière, B., and Chapuis, R.P. 2004. Evaluation of Unsaturated Flow in Mine Waste Rock. 57th Canadian Geotechnical Conference and the 5th joint CGS-IAH Conference, Canadian Geotechnical Society, 24–27 October 2004, Quebec City, pp. 24-27.

Mayer, K. U., Frind, E. O., & Blowes, D. W. 2002. Multicomponent reactive transport modeling in variably saturated porous media using a generalized formulation for kinetically controlled reactions. Water Resources Research, **38**(9), 13-1-13–21. doi.org/10.1029/2001wr000862.

Mayer, K. U., Gerard, F., Maier, U. 2010. MIN3P V2.0 User Guide.

Mbonimpa, M., Aubertin, M., Aachib, M., & Bussière, B. 2003. Diffusion and consumption of oxygen in unsaturated cover materials. Canadian Geotechnical Journal, **40**(5), 916-932.

Millington, R. J. 1959. Gas Diffusion in Porous Media. American Association for the Advancement of Science (New York, N.Y.), **130**(3367), 100–102.

Millington, R.J., and Shearer, R.C. 1971. Diffusion in aggregated porous media. Soil Science, **111**: 372-378.

Molson, J. W., Fala, O., Aubertin, M., & Bussière, B. 2005. Numerical simulations of pyrite oxidation and acid mine drainage in unsaturated waste rock piles. Journal of Contaminant Hydrology, **78**(4), 343–371. https://doi.org/10.1016/j.jconhyd.2005.06.005.

Molins S., Mayer K. U., Scheutz C., and Kjeldsen P. 2008. Transport and reaction processes affecting the attenuation of landfill gas in cover soils. Journal of Environmental Quality **37**, 459-468.

Neuner, M., Smith, L., Blowes, D.W., Sego, D.C., Smith, L.J.D., Fretz, N., and Gupton, M., 2013. The Diavik waste rock project: Water flow through mine waste rock in a permafrost terrain. Applied Geochemistry, **36** (1): 222–233. doi:10.1016/j.apgeochem.2012.03.01.

Oliver, J., Ayer, J., Dube, B., Aubertin, R., Burson, M., Panneton, G., Friedman, R., Hamilton, M. 2011. Structure, stratigraphy, U-Pb geochronology and alteration characteristics of gold mineralization at the Detour Lake gold deposit, Ontario, Canada. Exploration and Mining Geology **20**, 1-30.

Panneton, G., Aubertin, R., Donovan, P. 2009. Detour Lake: Discovery of a world class gold deposit in Ontario, Canada. 2009 NewGenGold Conference, 23-24 November 2009

Pantelis, G., Ritchie, A.I.M. 1992. Rate limiting factors in dump leaching of pyriticores. Appl. Math. Model, **16**: 553–560.

Penman, H.L. 1940a. Gas and Vapour Movements in the Soil: I. The diffusion of vapours through porous solids. Journal of Agricultural Science, **30**: 437-462.

Pham, H. Q., Fredlund, D. G., and Barbour, S. L. 2005. A study of hysteresis models for soil-water characteristic curves. Canadian Geotechnical Journal, **42**(6): 1548–1568. doi: 10.1139/t05-071.

Philip, J.R. 1964. Similarity hypothesis for capillary hysteresis in porous materials. Journal of Geophysical Research, **69**: 1553-1562.

Rahardjo, H., Satyanaga, A., Mohamed, H. et al. 2019. Comparison of Soil–Water Characteristic Curves from Conventional Testing and Combination of Small-Scale Centrifuge and Dew Point Methods. Geotech Geol Eng, **37**: 659–672 (2019). doi:10.1007/s10706-018-0636.

Rassam, D. W., and Williams, D. J. 2000. A Dynamic Method for Determining the Soil Water Characteristic Curve for Coarse-Grained Soils. Geotechnical Testing Journal, **23**(1): 67–71.

Ritchie, A.I.M. 2003. Oxidation and gas transport in piles of sulfidic material. In: J.L. Jambor et al., editors, Environmental aspects of mine wastes. Short Course Handb. 31. Mineral. Assoc. Canada, Quebec City, QC. p. 73–94.

Robertson, J., Barazzuol, L., and Day, S. 2012. Extraction of ARD/ML Information from a Brownfield Site for Development of an ARD/ML Plan at the Detour Gold Mine, Ontario, Canada.

Rouf, M. A., Hamamoto, S., Kawamoto, K., Sakaki, T., Komatsu, T., and Moldrup, P. 2012. Unified measurement system with suction control for measuring hysteresis in soil- gas transport parameters. Water Resources Research, **48**(2). doi:10.1029/2011WR010615

Scharer, J.M., Annable, W.K., and Nicholson, R.V. 1993. WATAIL1.0 user's manual. Institute for Groundwater Research, Univer-sity of Waterloo, Waterloo, Ont.

Seki, K. 2007. SWRC fit - a nonlinear fitting program with a water retention curve for soils having unimodal and bimodal pore structure. Hydrol. Earth Syst. Sci. Discuss., **4**: 407-437. doi:10.5194/hessd-4-407-2007.

Sjoberg, B.D. 2002. Evaluation of the Effectiveness of a Desulphurized Tailings Cover at Detour Lake Mine. MSc thesis, University of Saskatchewan, Saskatoon, SK, Canada.

Smith, L. and Beckie, R. 2003. Hydrological and geochemical transport processes in mine waste rock. In: Environmental Aspects of Mine Wastes, Short Course vol. 31, Mineralogical Association of Canada, pp. 51 – 72 (Chapter 3).

Smith, L. J. D., Blowes, D. W., Jambor, J. L., Smith, L., Sego, D. C., and Neuner, M. 2013. The diavik waste rock project: Particle size distribution and sulfur characteristics of low-sulfide waste rock. Applied Geochemistry, **36**: 200–209. doi:10.1016/j.apgeochem.2013.05.006.

Smith, L., López, D.L., Beckie, R., Morin, K., Dawson, R., and Price, W. 1995. Hydrogeology of waste rock dumps - Mend Associate Project PA-1. (July): 115.

SRK Consulting. 2004. Geochemical studies of waste rock at the Anvil Range Mining Complex (Phase 3 Report).

Stockwell J., Smith L., Jambor J.L., and Beckie R. 2006. The relationship between fluid flow and mineral weathering in heterogeneous unsaturated porous media: A physical and geochemical characterization of a waste-rock pile. Applied Geochemistry, **21** (8), pp. 1347-1361.

Swanson, D.A., Savci, G., Danziger, G., Mohr, R.N., and Weiskopf, T. 1999. Predicting the soil water characteristics of mine soils. Tailings and Mine Waste: 345–349. Available from http://www.savci-env.com/documents/SETminewasteconf.pdf.

Tang, M.S.M. 2011. Delineation of Groundwater Capture Zone for the Faro Mine, Faro Mine Complex, Yukon Territory. Undergraduate Honours Thesis. Department of Earth and Ocean Sciences. University of British Columbia.

Tokunaga, T. K., Wan, J., and Olson, K. R. 2002. Saturation-matric potential relations in gravel. Water Resources Research, **38**(10): 32-1-32–37. doi:10.1029/2001wr001242.

Tuller, M., and Or, D. 2004. Water retention and characteristic curve. Encyclopedia of Soils in the Environment, **4**: 278– 289, Elsevier, Oxford, U. K., doi:10.1016/B0-12-348530-4/00376-3.

Watson, I., and Burnett, A. 1995. Hydrology, an Environmental Approach: Theory and Applications of Ground Water and Surface Water for Engineers and Geologists.

Wickland, B., Wilson, W., Wijewickreme, D., and Fredlund, D. 2006. Mixtures of Waste Rock and Tailings: Resistance To Acid Rock Drainage. Journal American Society of Mining and Reclamation, **2006**(2): 2369–2376. doi:10.21000/jasmr06022369.

Williams, D. J. 2010. Laboratory versus field SWCC Data. Unsaturated Soils – Buzzi, Fityus & Sheng (eds). Taylor & Francis Group, London, ISBN 978-0-415-80480-6.

van Genuchten, M.T. 1980. A closed-form equation for predicting the hydraulic conductivity of unsaturated soils. Soil Science Society of America Journal, **44**: 892–898. doi:10.2136/sssaj1980.03615995004400050002x.

Vriens, B., Arnault, M. st., Laurenzi, L., Smith, L., Mayer, K. U., and Beckie, R. D. 2018. Localized Sulfide Oxidation Limited by Oxygen Supply in a Full-Scale Waste-Rock Pile. Vadose Zone Journal, **17**(1): 180119. doi:10.2136/vzj2018.06.0119.

Wunderly, M.D., Blowes, D.W., Frind, E.O., Ptacek, C.J. 1996. Sulfide mineral oxidation and subsequent reactive transport of oxidation products in mine tailings impoundments: a numerical model. Water Resour. Res. **32**, 3173–3187.

Yang, H., Rahardjo, H., Leong, E.C., and Fredlund, D.G. 2004. Factors affecting drying and wetting soil-water characteristic curves of sandy soils. Canadian Geotechnical Journal, **41**(5): 908–920. doi:10.1139/T04-042.

Yazdani, J., Barbour, L, and Wilson, G.W. 2000. Soil-water characteristic curve for mine waste rock containing coarse material, from Proceedings of the 6th Environmental Engineering Specialty Conference of the Canadian Society of Civil Engineers, London, ON, Canada.

Yip, C. G., & Thompson, K. S. 2015. Diavik Diamond Mine. Yellowknife, NT: Diavik Diamond Mine Inc.

Zhai, Q., and Rahardjo, H. 2012. Determination of soil-water characteristic curve variables. Computers and Geotechnics, **42** 37–43. doi:10.1016/j.compgeo.2011.11.010.

Appendix A

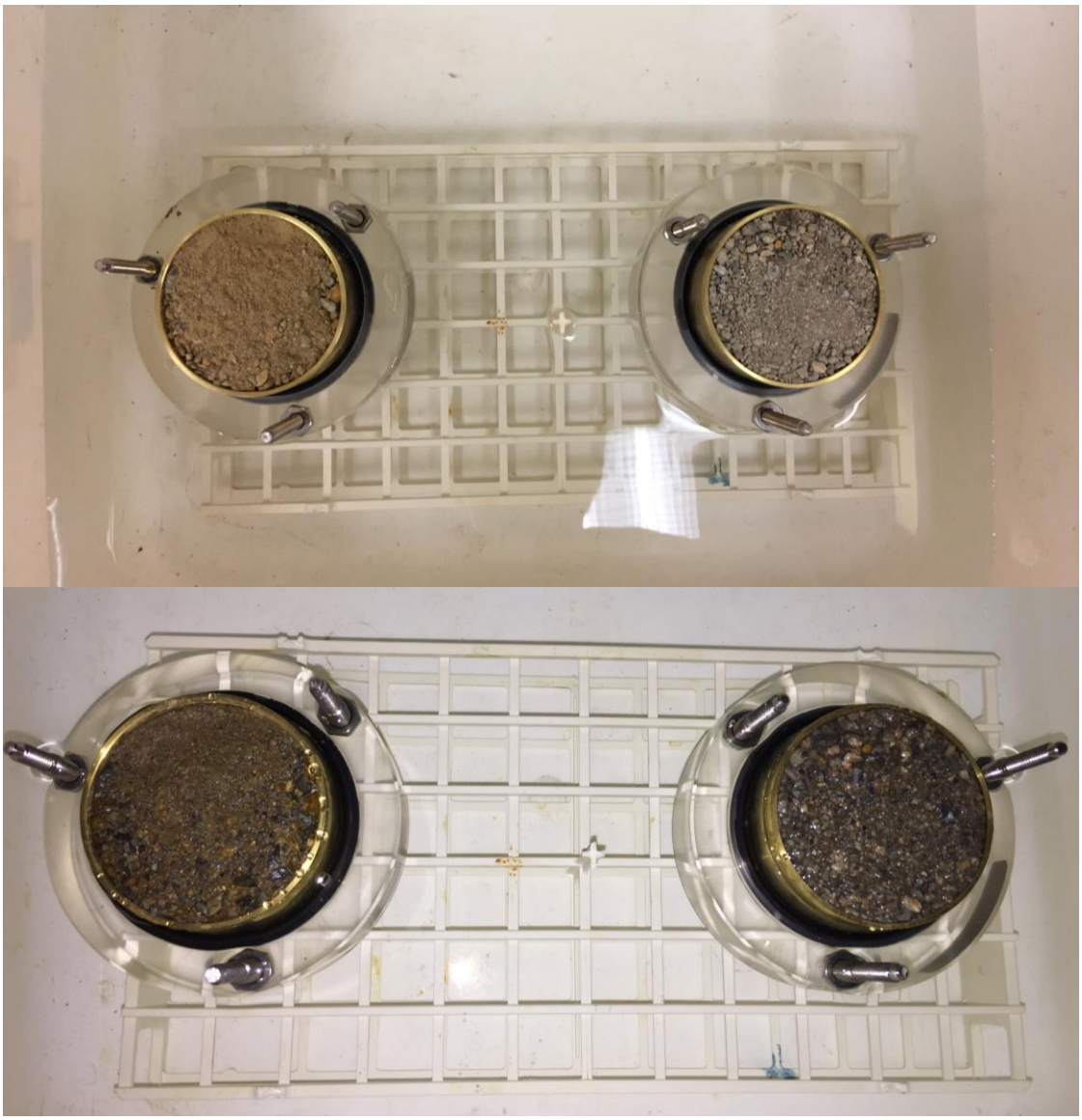

Fig. A.1 Matrix material in Tempe cells before (top) and after saturation (bottom).

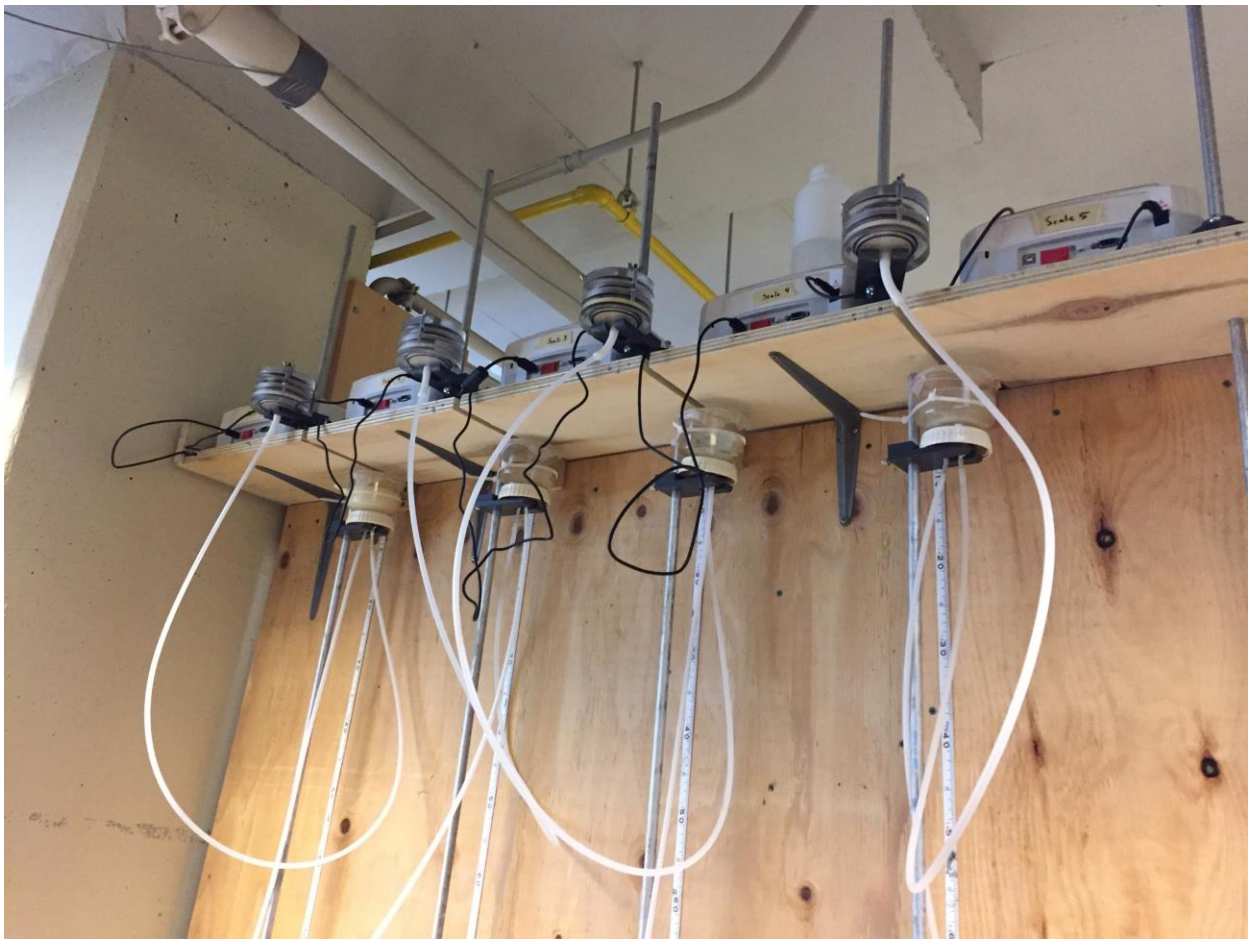

Fig. A.2 Hanging water column used to measure soil-water characteristic curves.

Table A.1 Diavik Measured gravimetric weight at different applied pressures used to develop soil-water characteristic curves

Drying Curve				
Pressure (kPa)	**Diavik Tempe Cell Weight (g)**	**Weight of Sample without Tempe cell (g)**	**Gravimetric Water Content ($m\ m^{-1}$)**	**Volumetric Water Content ($m^3\ m^{-3}$)**
1	529.32	131.51	0.1326	0.2161
2	529.18	131.37	0.1314	0.2141
4	529.12	131.31	0.1309	0.2133
6	529.00	131.19	0.1299	0.2116
8	528.65	130.84	0.1269	0.2067
10	527.96	130.15	0.1209	0.1970
18	524.98	127.17	0.0953	0.1552
28	522.63	124.82	0.0750	0.1222
54	520.70	122.89	0.0584	0.0951
84	519.09	121.28	0.0445	0.0725

Wetting Curve				
Pressure (kPa)	**Diavik Tempe Cell Weight (g)**	**Weight of Sample without Tempe cell (g)**	**Gravimetric Water Content ($m\ m^{-1}$)**	**Volumetric Water Content ($m^3\ m^{-3}$)**
68	519.11	121.30	0.0447	0.0728
54	519.83	122.02	0.0509	0.0829
22	521.45	123.64	0.0649	0.1056
14	522.95	125.14	0.0778	0.1267
5	525.00	127.19	0.0954	0.1555
2	526.64	128.83	0.1096	0.1785

Table A.2 Detour Measured gravimetric weight at different applied pressures used to develop soil-water characteristic curves

Drying Curve				
Pressure (kPa)	**Detour Tempe Cell Weight (g)**	**Weight of Sample without Tempe cell (g)**	**Gravimetric Water Content ($m\ m^{-1}$)**	**Volumetric Water Content ($m^3\ m^{-3}$)**
1	532.84	132.54	0.1397	0.2280
3	532.39	132.09	0.1359	0.2217
4	532.13	131.83	0.1336	0.2180
6	531.70	131.40	0.1299	0.2120
8	531.10	130.80	0.1248	0.2036
10	530.41	130.11	0.1188	0.1939
13	528.99	128.69	0.1066	0.1740
25	526.65	126.35	0.0865	0.1411
44	523.20	122.90	0.0568	0.0927
60	521.90	121.60	0.0457	0.0745
76	521.44	121.14	0.0417	0.0680
90	520.78	120.48	0.0360	0.0588

Wetting Curve				
Pressure (kPa)	**Detour Tempe Cell Weight (g)**	**Weight of Sample without Tempe cell (g)**	**Gravimetric Water Content ($m\ m^{-1}$)**	**Volumetric Water Content ($m^3\ m^{-3}$)**
72	521.85	121.55	0.0452	0.0738
60	522.06	121.76	0.0470	0.0767
42	522.74	122.44	0.0529	0.0863
18	527.04	126.74	0.0899	0.1466
8	528.42	128.12	0.1017	0.1660
4	528.96	128.66	0.1064	0.1736
2	529.47	129.17	0.1108	0.1807

Table A.3 Faro Measured gravimetric weight at different applied pressures used to develop soil-water characteristic curves

Drying Curve				
Pressure (kPa)	Faro Tempe Cell Weight (g)	Weight of Sample without Tempe cell (g)	Gravimetric Water Content ($m\ m^{-1}$)	Volumetric Water Content ($m^3\ m^{-3}$)
1	527.82	130.01	0.2097	0.3162
3	524.53	126.72	0.1791	0.2701
4	524.03	126.22	0.1745	0.2631
6	522.27	124.46	0.1581	0.2384
8	521.07	123.26	0.1469	0.2215
10	519.86	122.05	0.1357	0.2046
13	518.25	120.44	0.1207	0.1820
25	516.27	118.46	0.1023	0.1542
52	508.61	110.80	0.0310	0.0467

Wetting Curve				
Pressure (kPa)	Faro Tempe Cell Weight (g)	Weight of Sample without Tempe cell (g)	Gravimetric Water Content ($m\ m^{-1}$)	Volumetric Water Content ($m^3\ m^{-3}$)
42	510.78	112.97	0.0512	0.0772
18	514.76	116.95	0.0882	0.1330
8	516.00	118.19	0.0997	0.1504
4	516.68	118.87	0.1061	0.1599
2	517.30	119.49	0.1118	0.1686

Appendix B

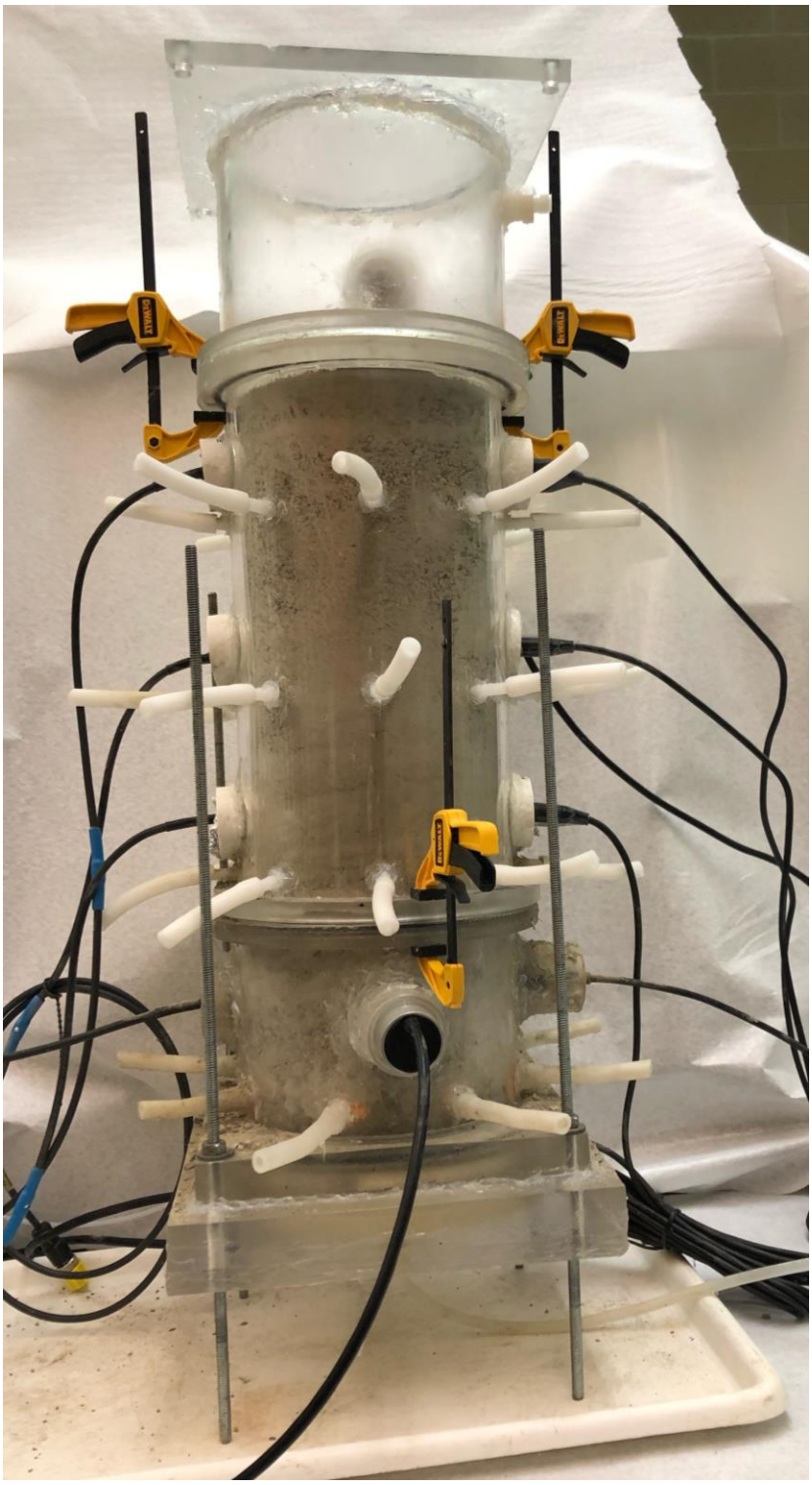

Fig. B.1 Saturation Diffusion apparatus with all ports open.

Fig. B.2 Single diffusion port (10 cm length) to allow for gaseous diffusion into the column. Polyethylene tubing perforated radially along the length (6 cm) of the tube with a thumb tac.

Fig. B.3 Wetting front during the initial saturation of Diavik matrix material.

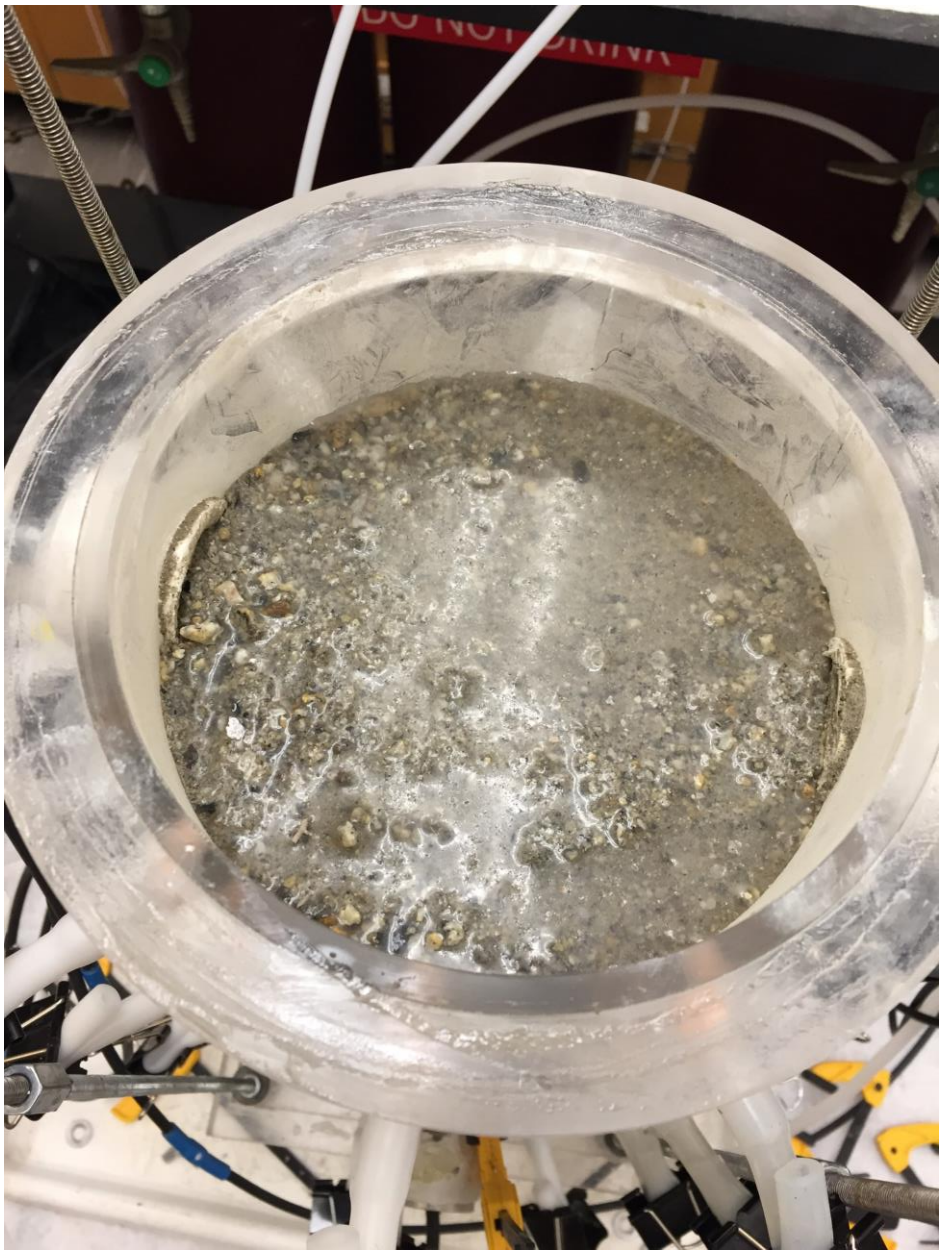

Fig. B.4 Standing water at the top of Diavik matrix material in the column during the end of the initial wetting process.

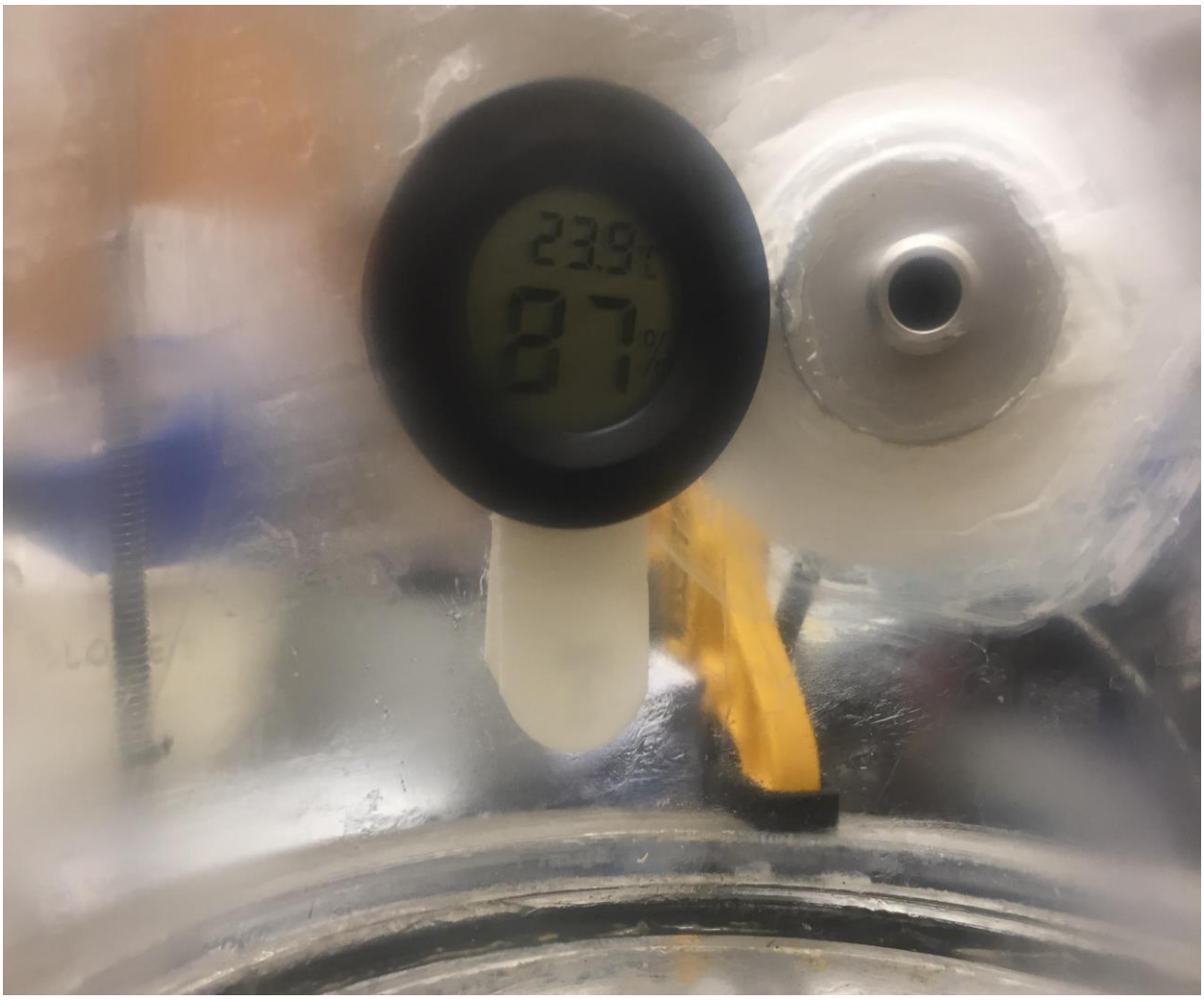

Fig. B.5 Kiyanco mini hygrometer placed inside the diffusion chamber to measure relative humidity and temperature to calibrate the oxygen sensor.

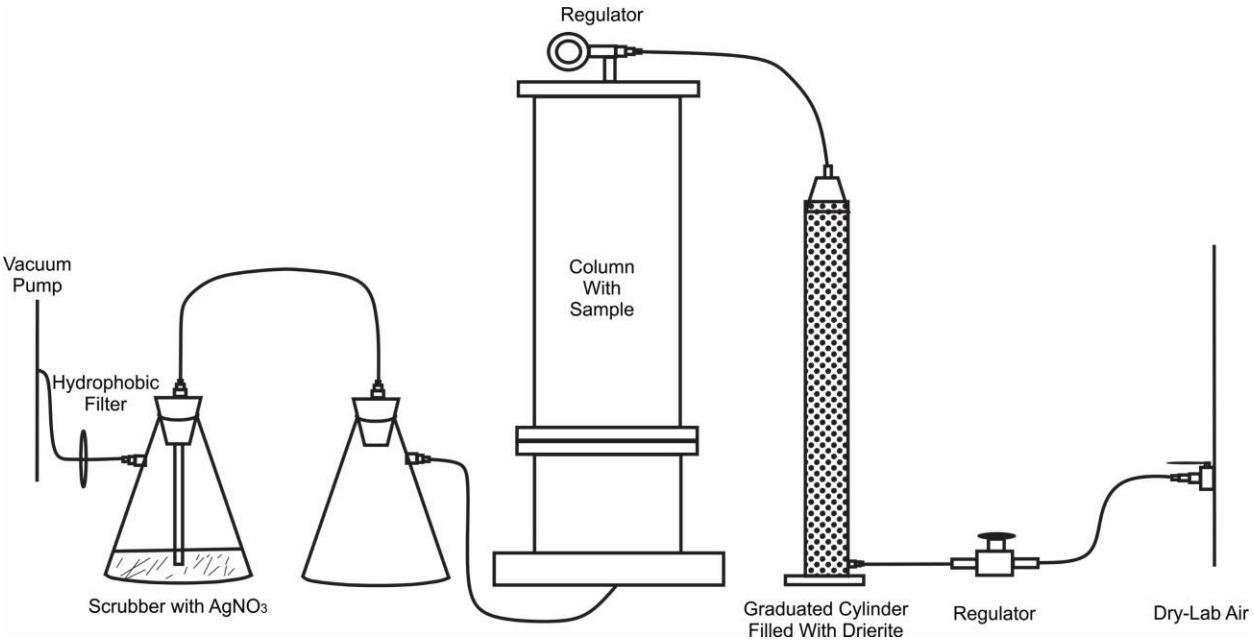

Fig. B.6 Vacuum pump set up connected to dry lab air to decrease saturation of the matrix material within the column.

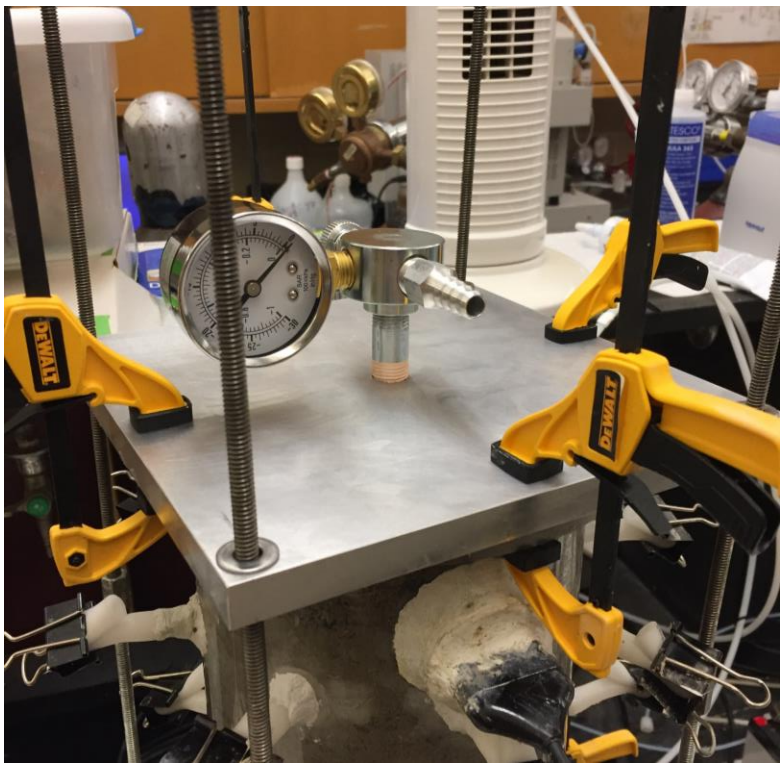

Fig. B.6 Vacuum pump regulator (0 to 30" Hg, 2 cfm max capacity; Cole Parmer) on top of the column to control suction from the vacuum pump.

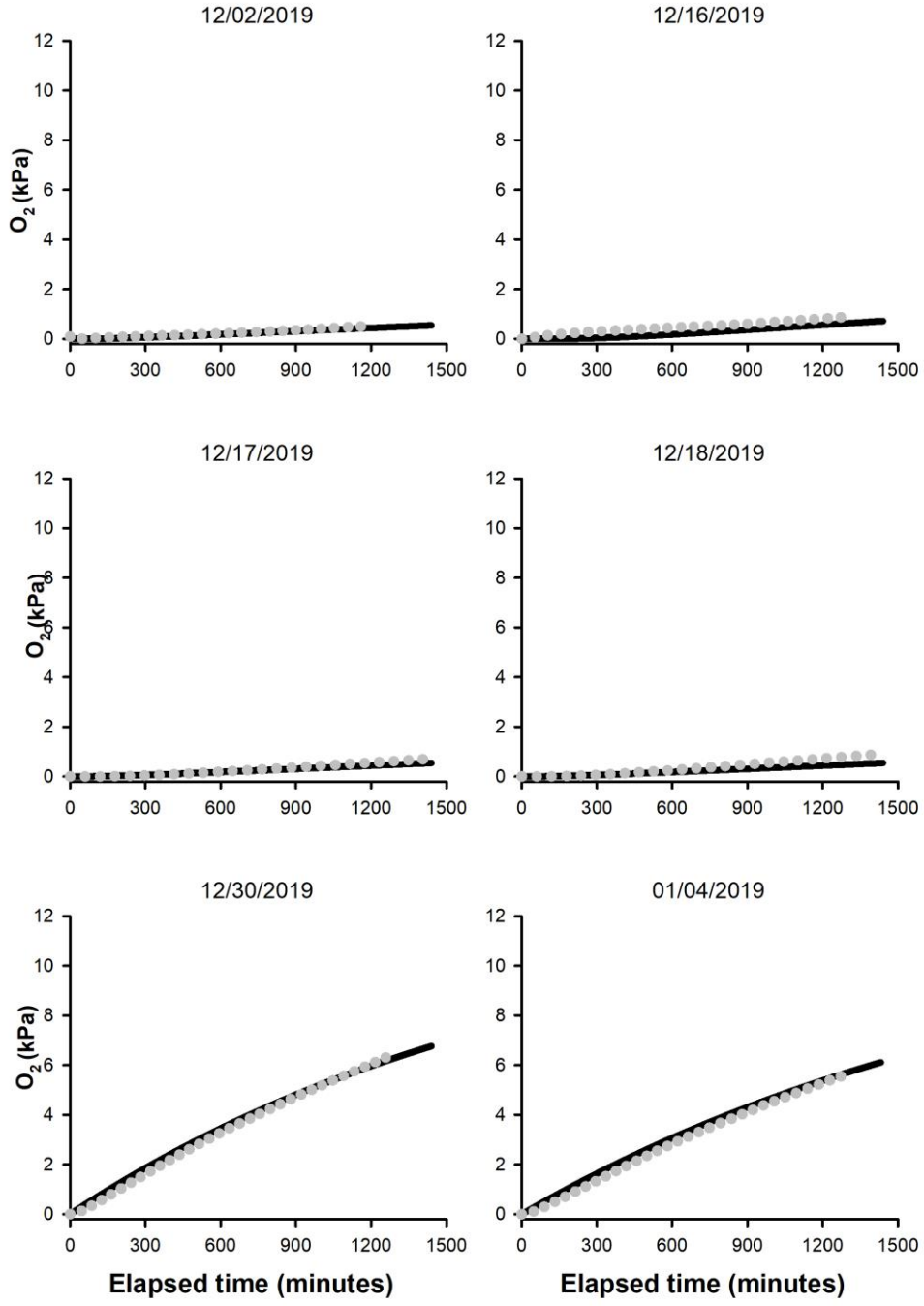

Fig. B.7.1 Diavik Drying. Measured $O_{2(g)}$ concentration (dotted grey line) compared to MIN3P $O_{2(g)}$ concentrations from MIN3P simulations (black line).

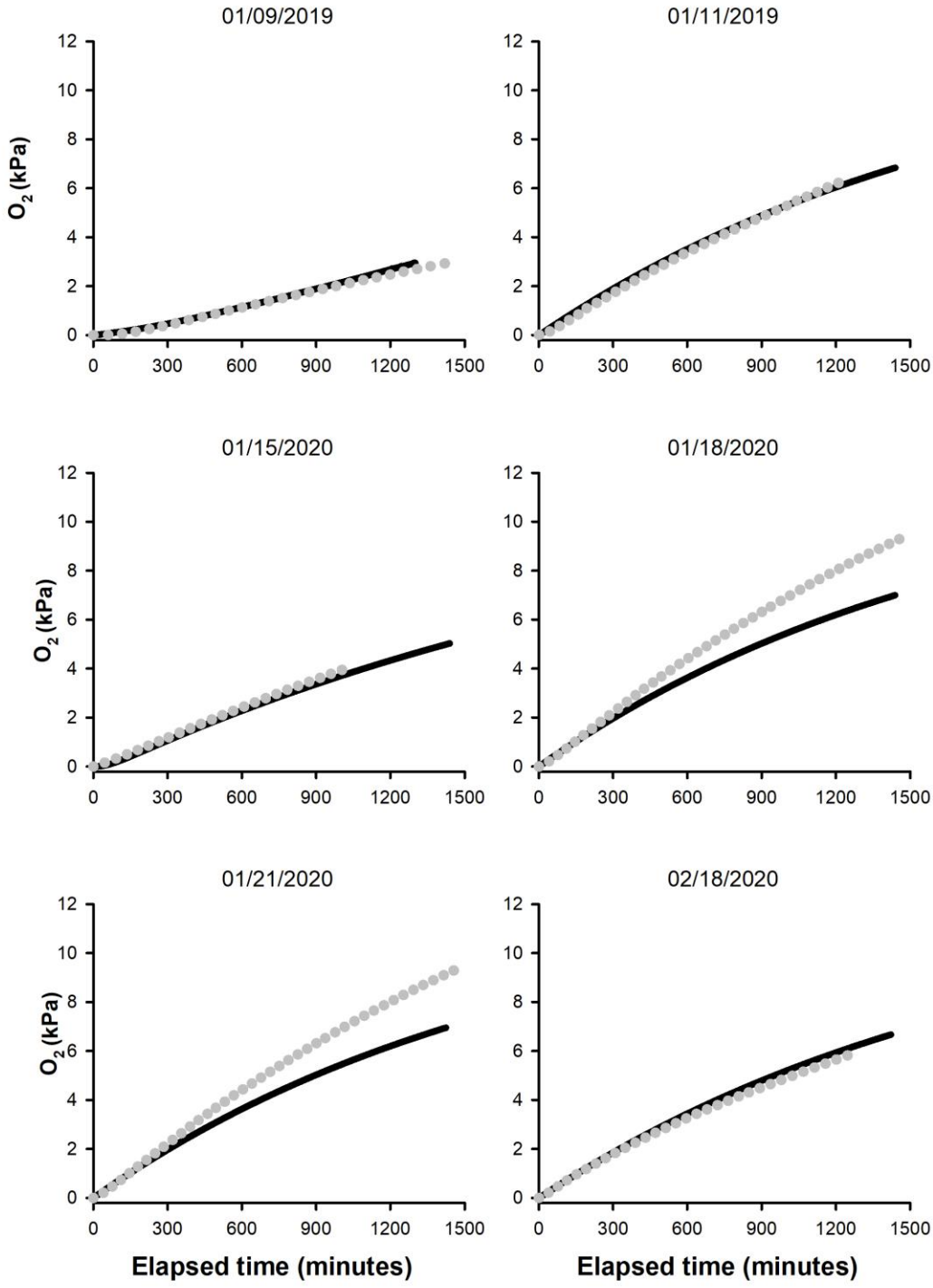

Fig. B.7.2 Diavik Drying. Measured $O_{2(g)}$ concentration (dotted grey line) compared to MIN3P $O_{2(g)}$ concentrations from MIN3P simulations (black line).

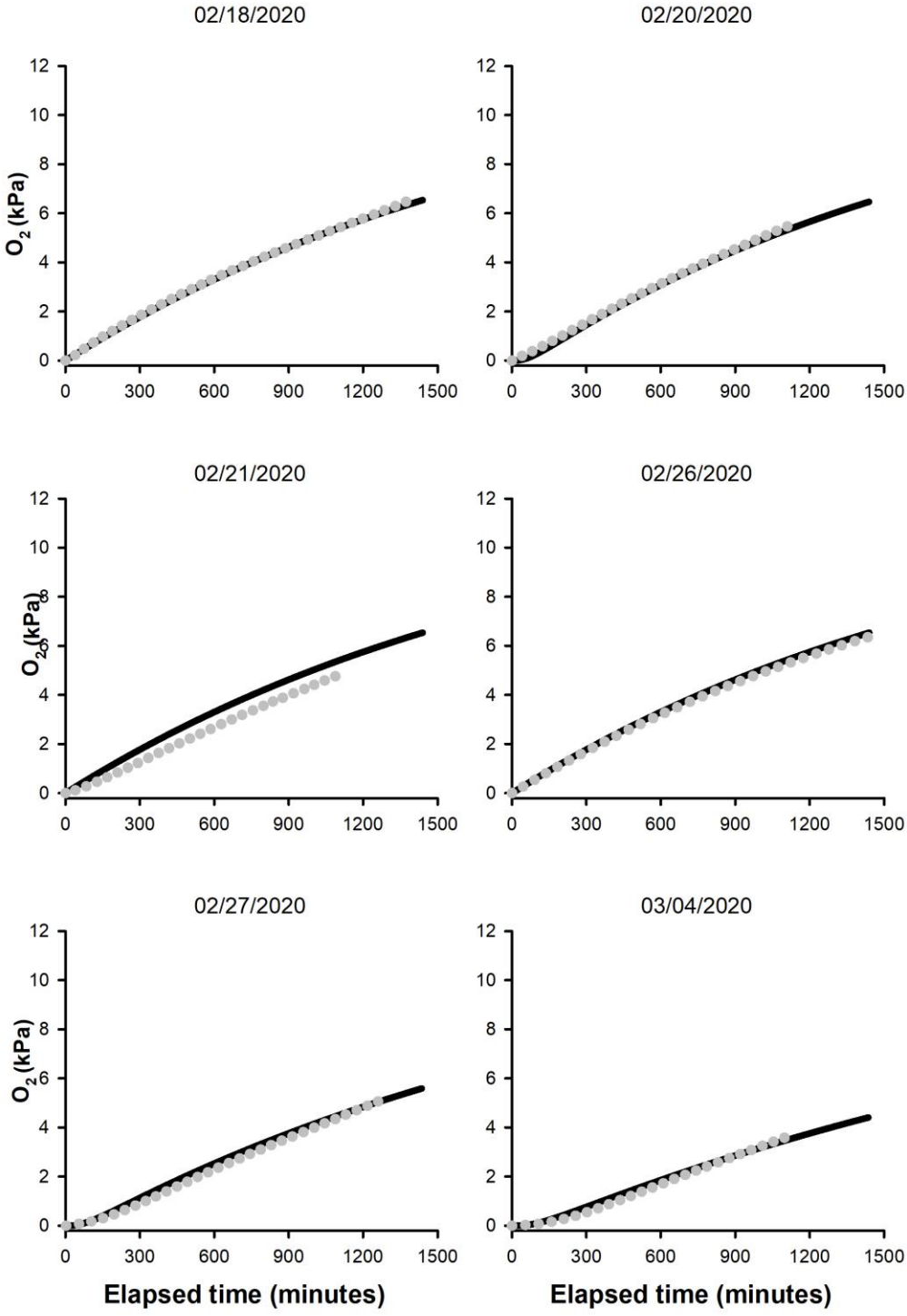

Fig. B.8.1 Diavik Wetting. Measured $O_{2(g)}$ concentration (dotted grey line) compared to MIN3P $O_{2(g)}$ concentrations from MIN3P simulations (black line).

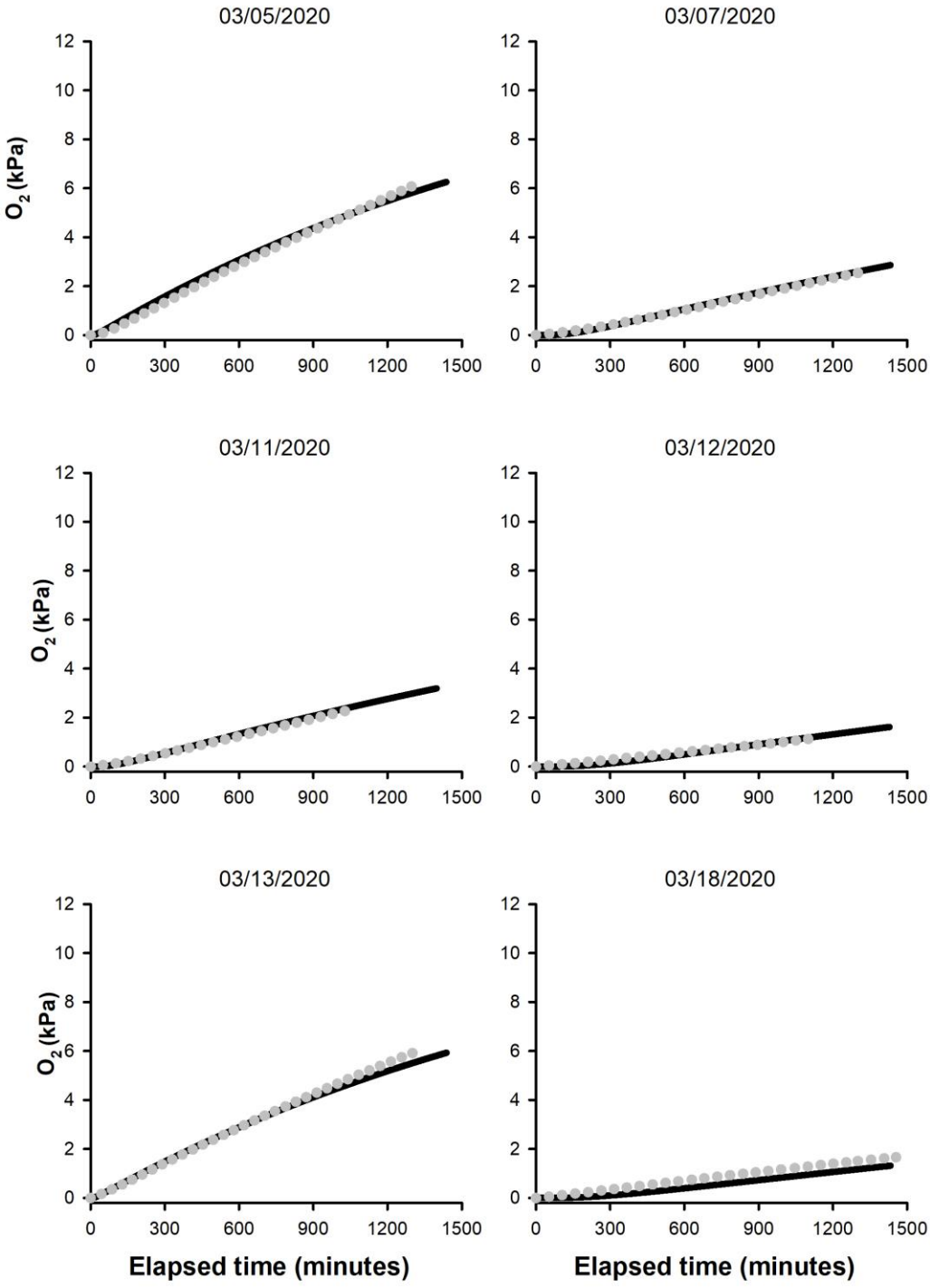

Fig. B.8.2 Diavik Wetting. Measured $O_{2(g)}$ concentration (dotted grey line) compared to MIN3P $O_{2(g)}$ concentrations from MIN3P simulations (black line).

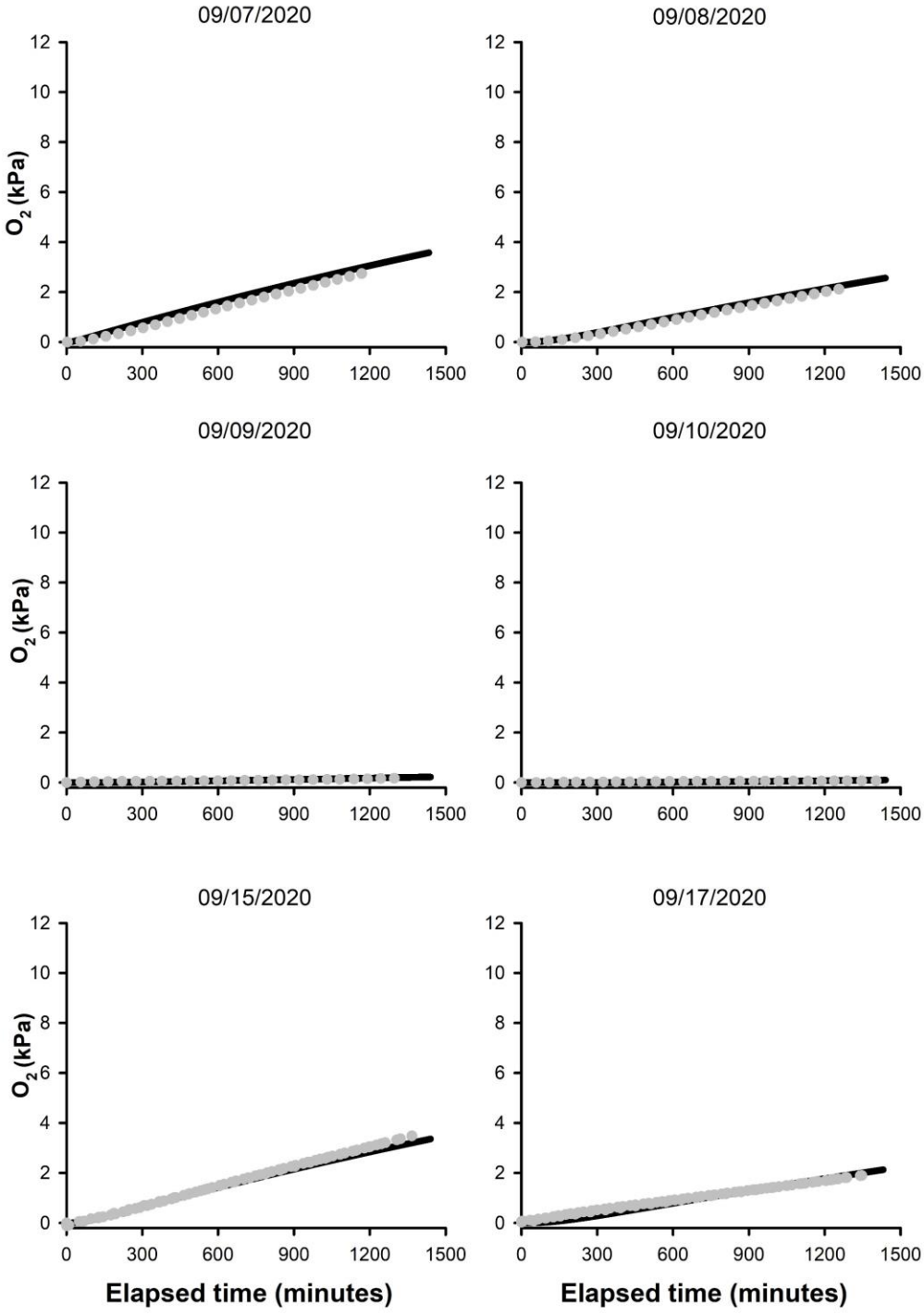

Fig. B.9.1 Faro Drying. Measured $O_{2(g)}$ concentration (dotted grey line) compared to MIN3P $O_{2(g)}$ concentrations from MIN3P simulations (black line).

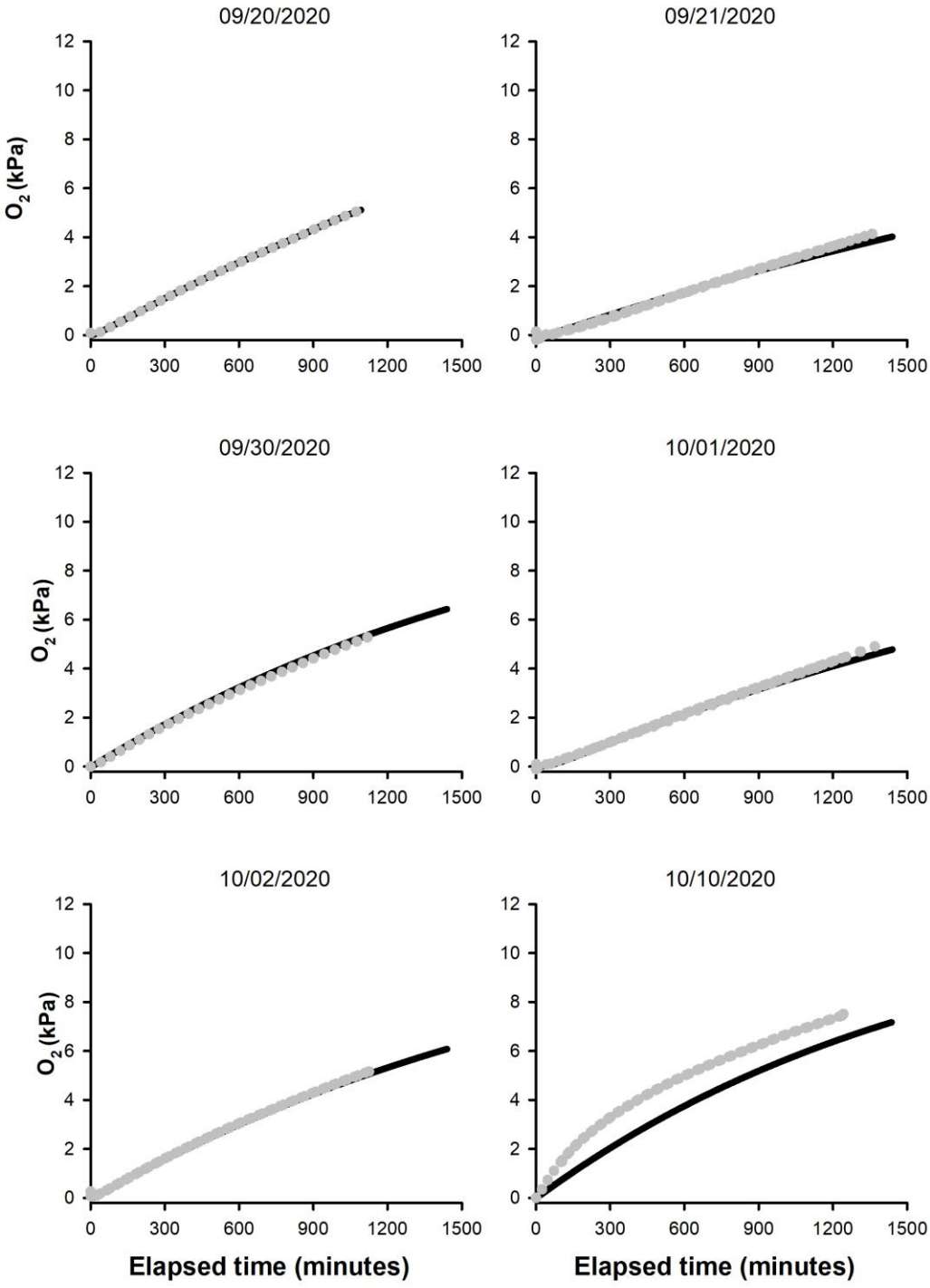

Fig. B.9.2 Faro Drying. Measured $O_{2(g)}$ concentration (dotted grey line) compared to MIN3P $O_{2(g)}$ concentrations from MIN3P simulations (black line).

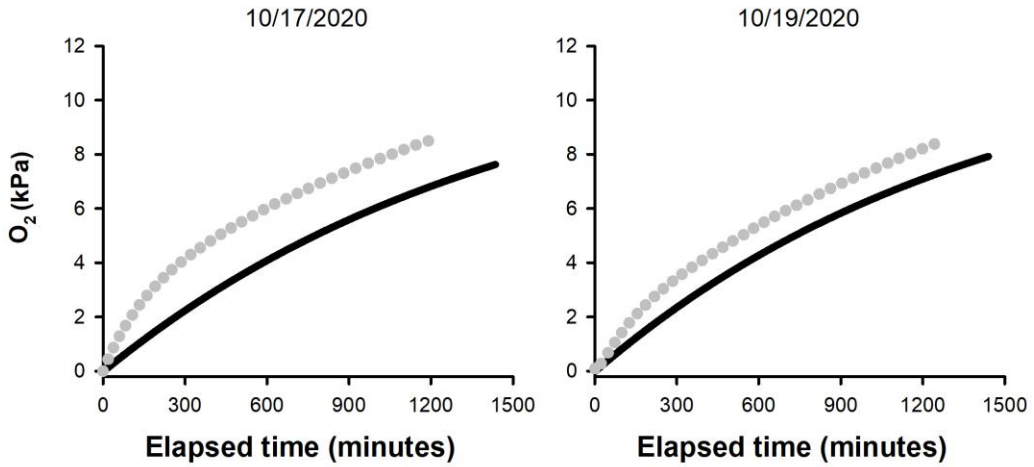

Fig. B.9.3 Faro Drying. Measured $O_{2(g)}$ concentration (dotted grey line) compared to MIN3P $O_{2(g)}$ concentrations from MIN3P simulations (black line).

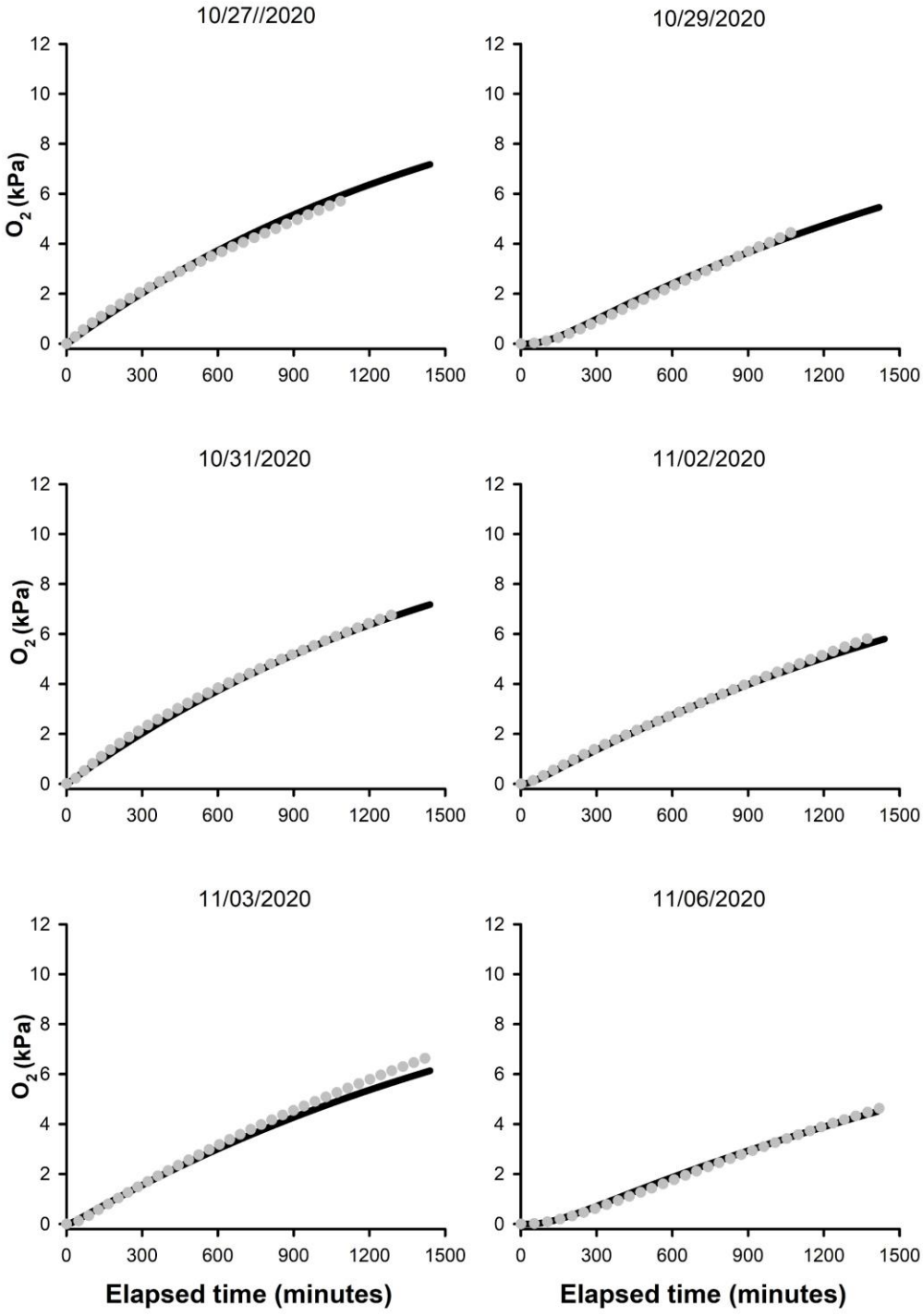

Fig. B.10.1 Faro Wetting. Measured $O_{2(g)}$ concentration (dotted grey line) compared to MIN3P $O_{2(g)}$ concentrations from MIN3P simulations (black line).

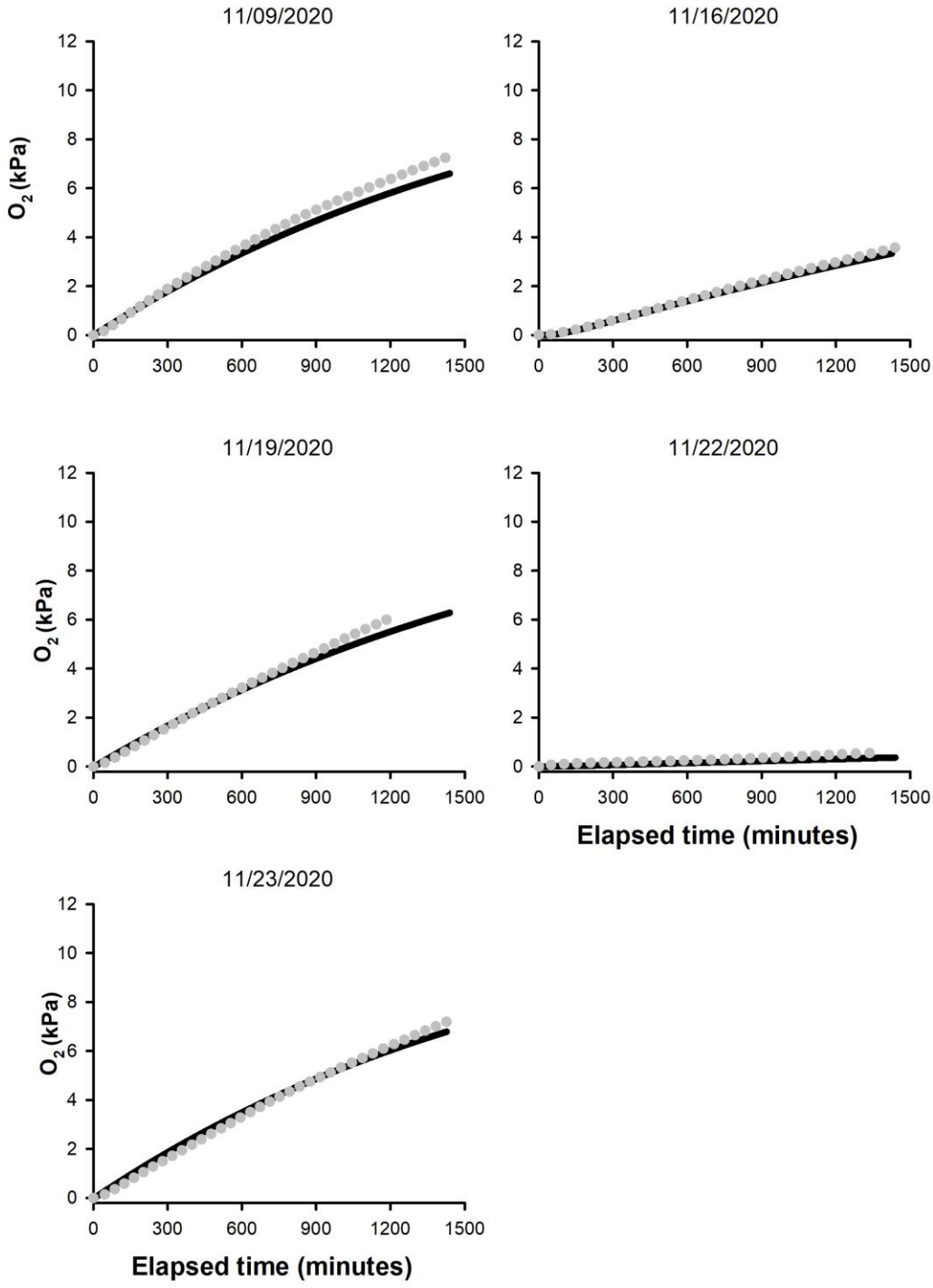

Fig. B.10.1 Faro Wetting. Measured $O_{2(g)}$ concentration (dotted grey line) compared to MIN3P $O_{2(g)}$ concentrations from MIN3P simulations (black line).

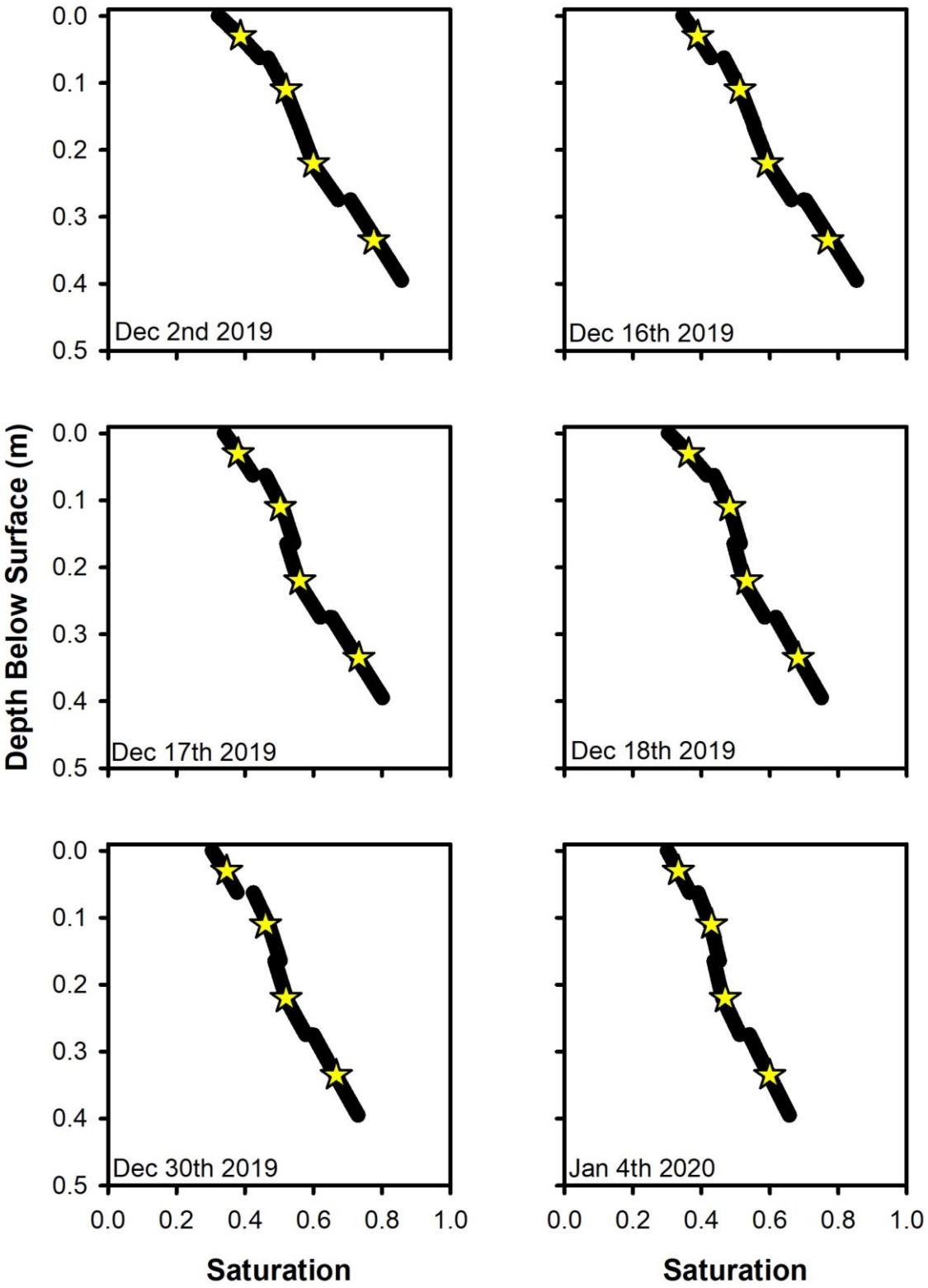

Fig. B.11.1 Diavik Drying. MIN3P simulated moisture content profiles (black line) compared to measured moisture content values from the ECH2Os in the column (yellow stars).

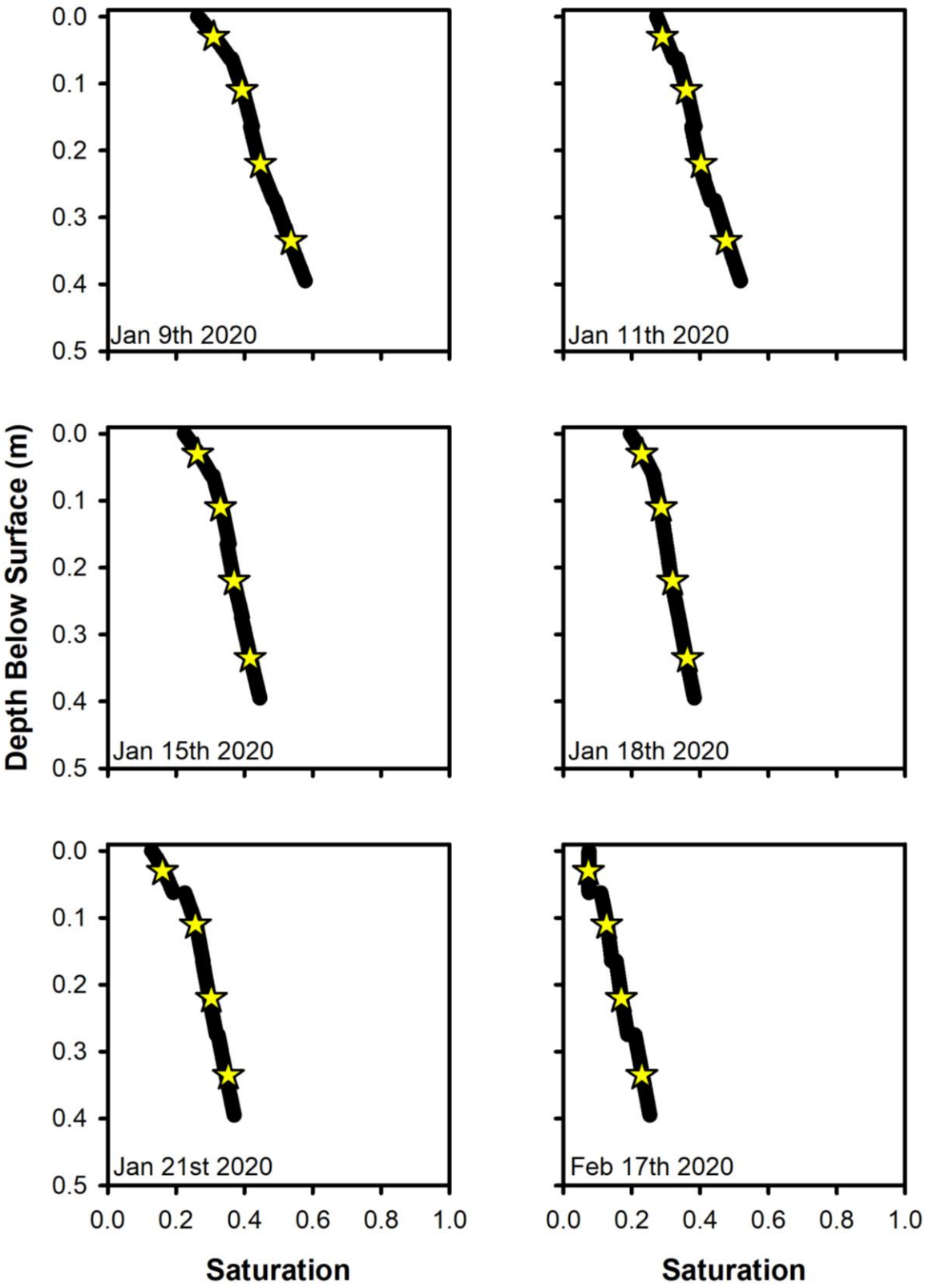

Fig. B.11.2 Diavik Drying. MIN3P simulated moisture content profiles (black line) compared to measured moisture content values from the ECH2Os in the column (yellow stars).

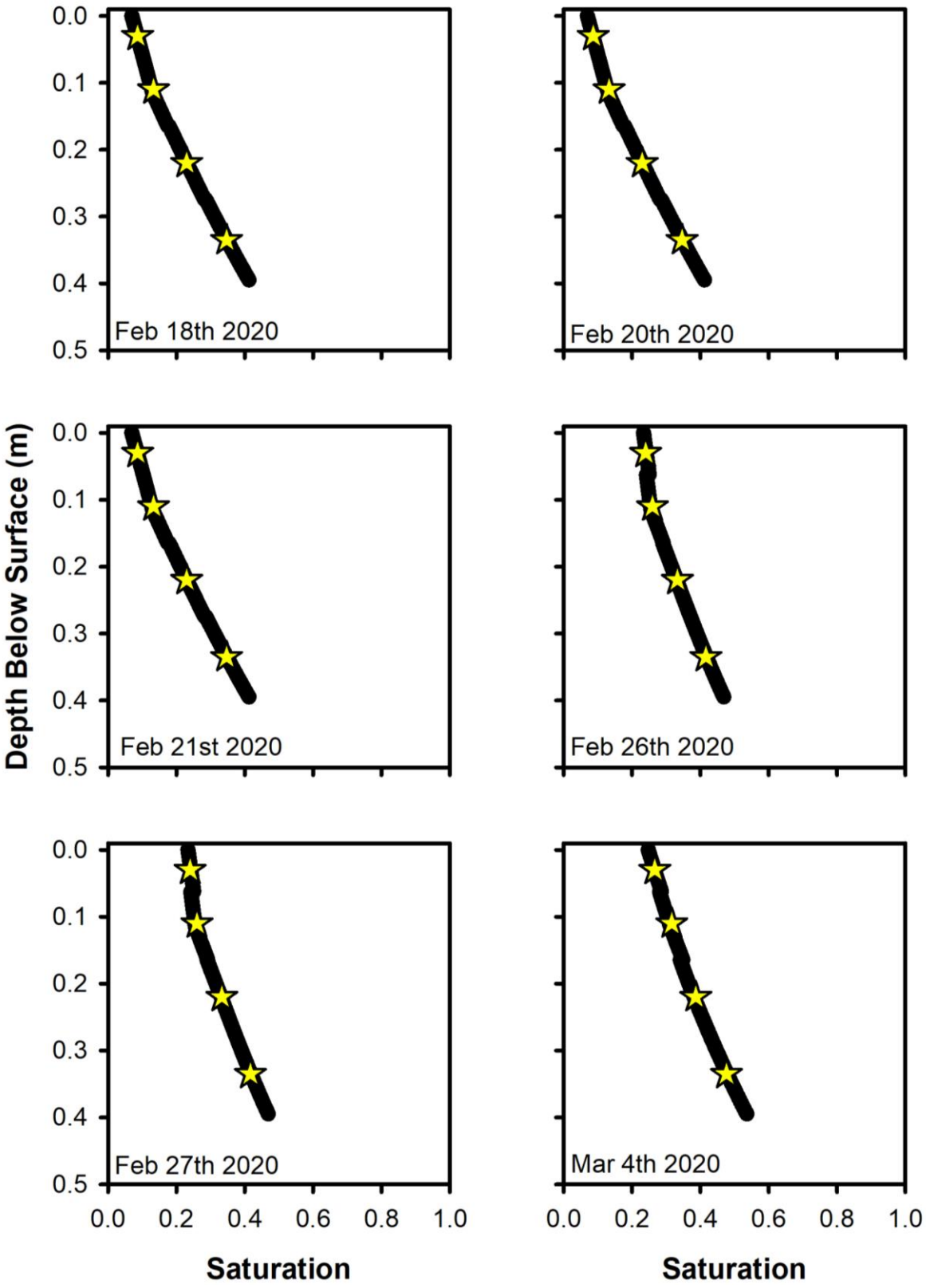

Fig. B.12.1 Diavik Wetting. MIN3P simulated moisture content profiles (black line) compared to measured moisture content values from the ECH2Os in the column (yellow stars).

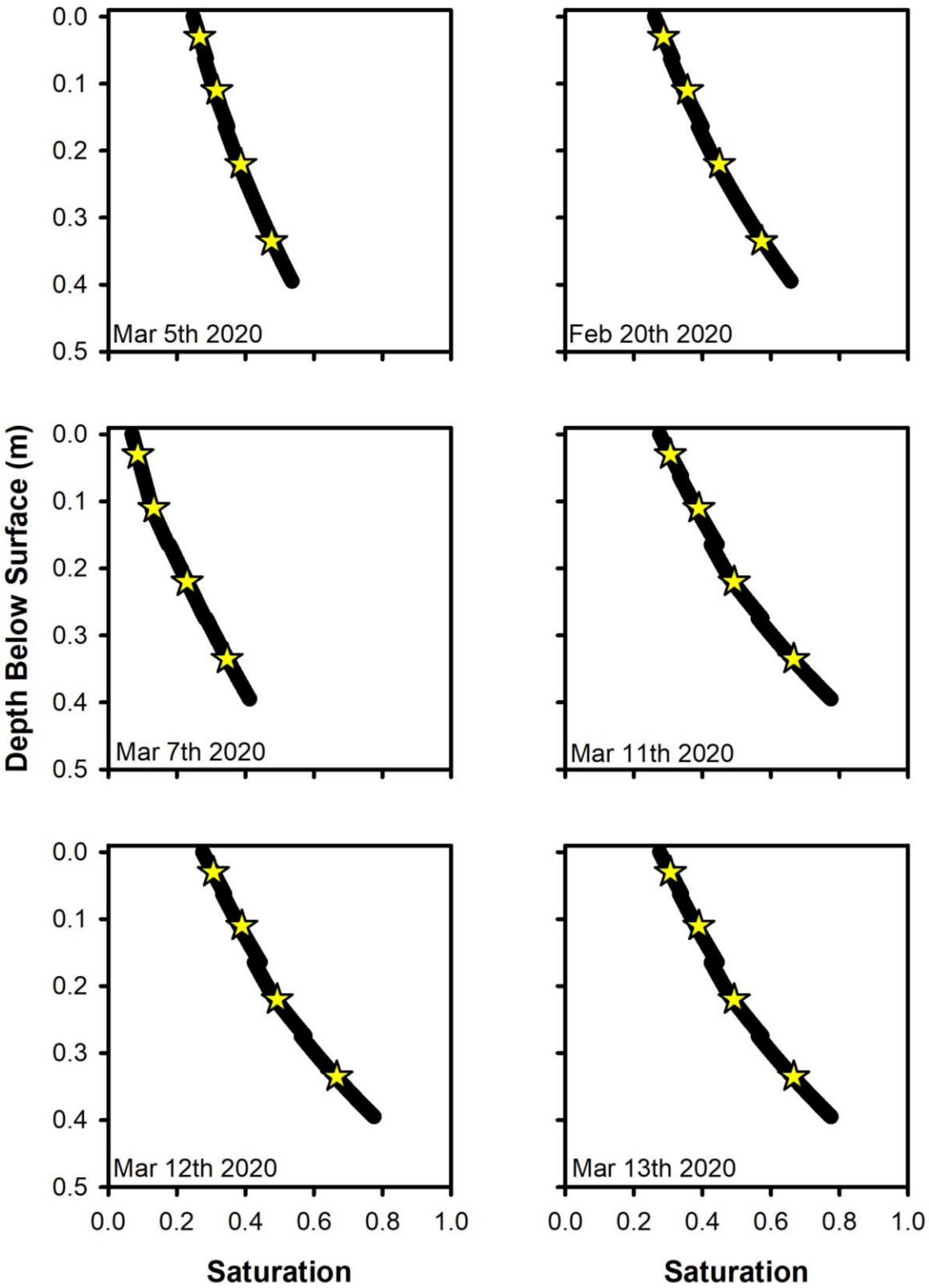

Fig. B.12.2 Diavik Wetting. MIN3P simulated moisture content profiles (black line) compared to measured moisture content values from the ECH2Os in the column (yellow stars).

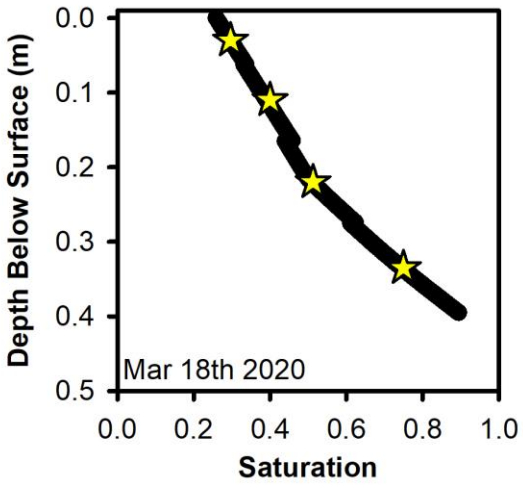

Fig. B.12.3 Diavik Wetting. MIN3P simulated moisture content profiles (black line) compared to measured moisture content values from the ECH*2*Os in the column (yellow stars).

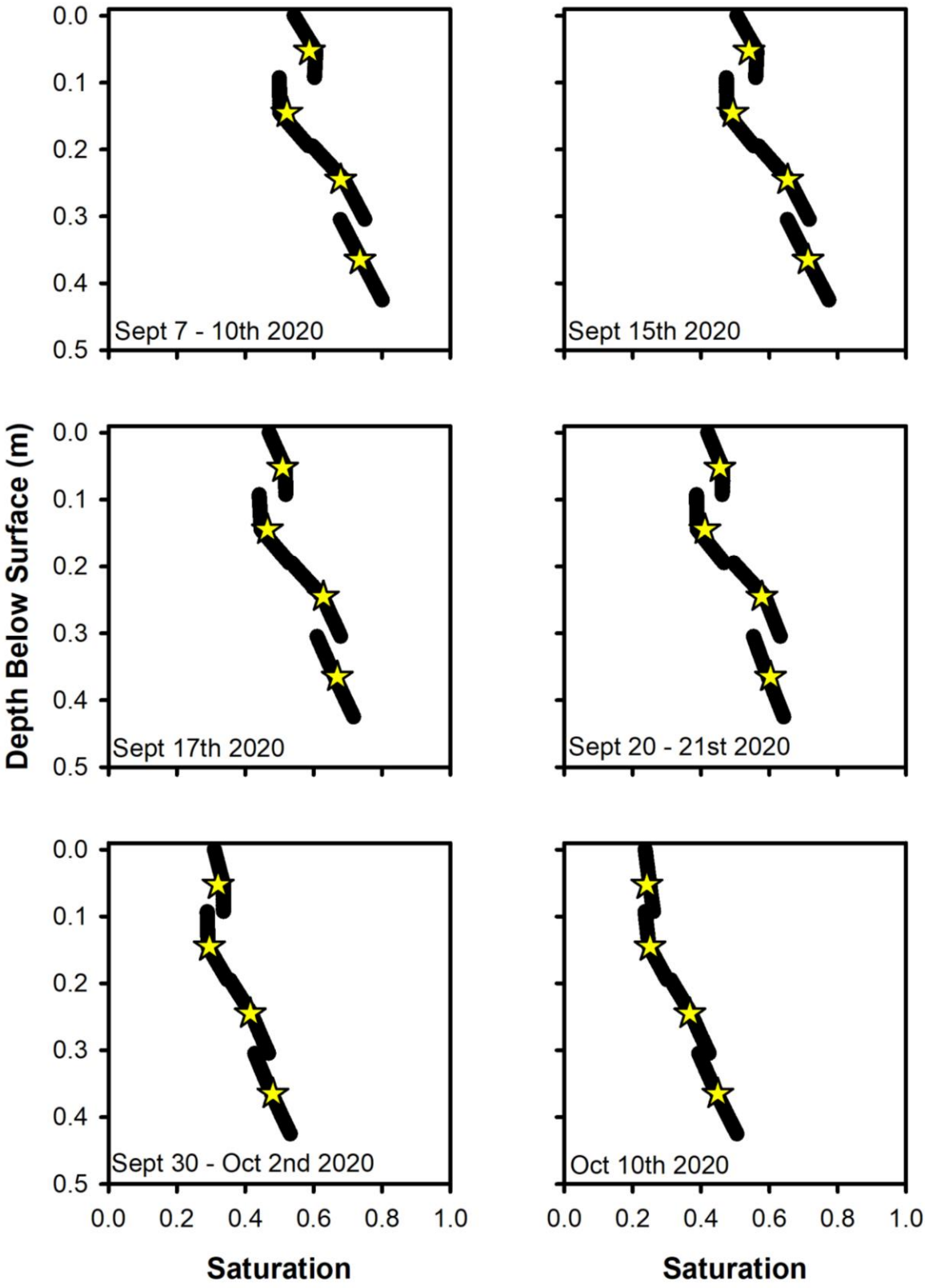

Fig. B.13.1 Faro Drying. MIN3P simulated moisture content profiles (black line) compared to measured moisture content values from the ECH2Os in the column (yellow stars).

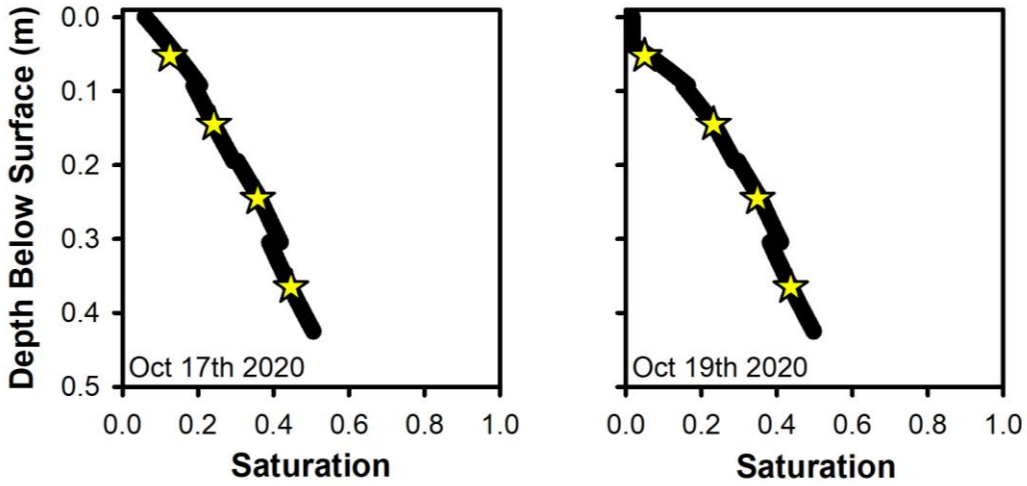

Fig. B.13.2 Faro Drying. MIN3P simulated moisture content profiles (black line) compared to measured moisture content values from the ECH*2*Os in the column (yellow stars).

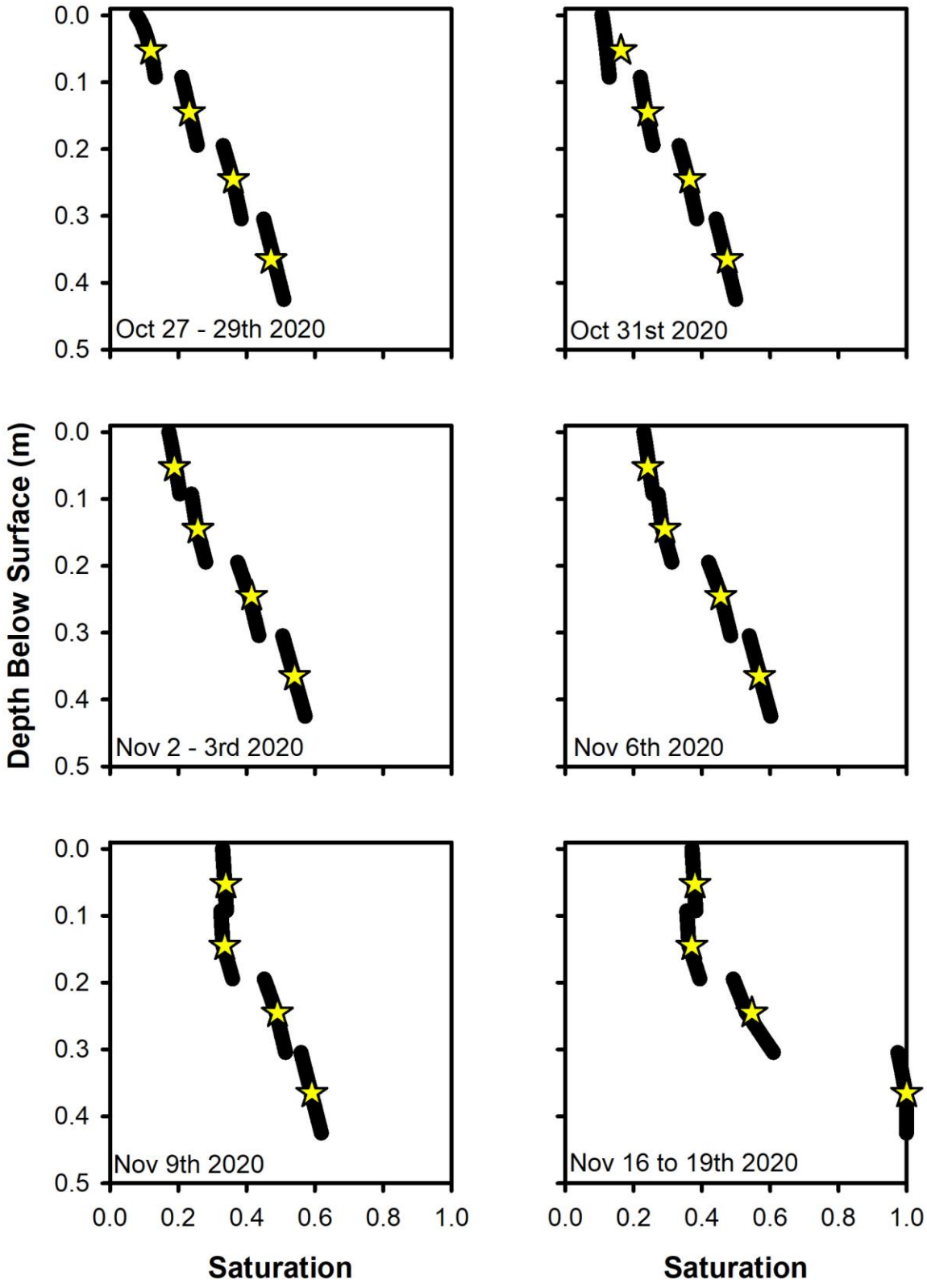

Fig. B.14.1 Faro Wetting. MIN3P simulated moisture content profiles (black line) compared to measured moisture content values from the ECH2Os in the column (yellow stars).

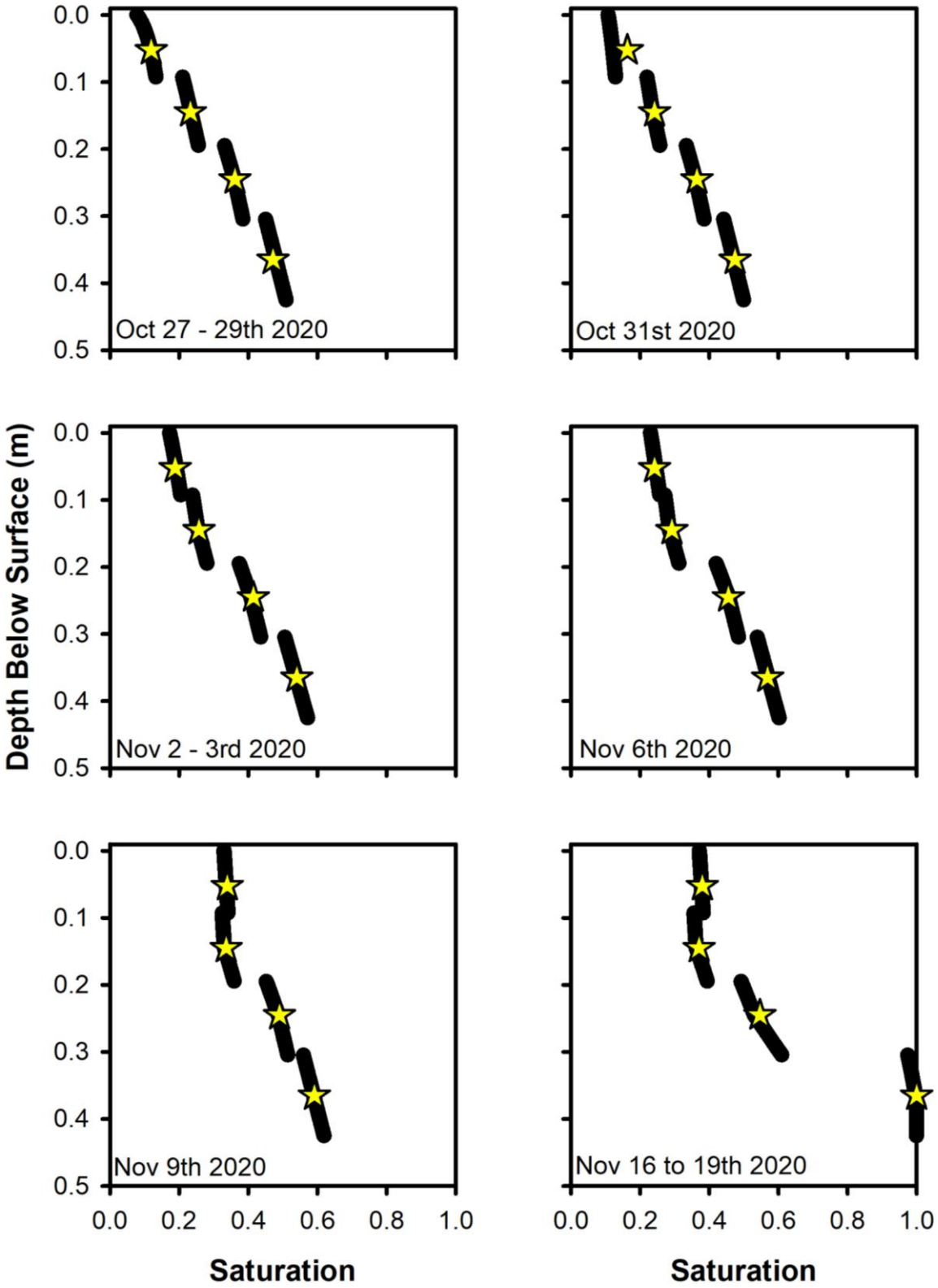

Fig. B.14.2 Faro Wetting. MIN3P simulated moisture content profiles (black line) compared to measured moisture content values from the ECH*2*Os in the column (yellow stars).

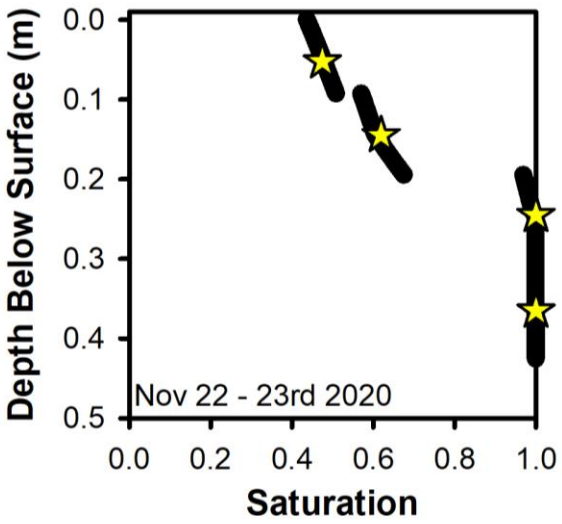

Fig. B.14.3 Faro Wetting. MIN3P simulated moisture content profiles (black line) compared to measured moisture content values from the ECH2Os in the column (yellow stars).

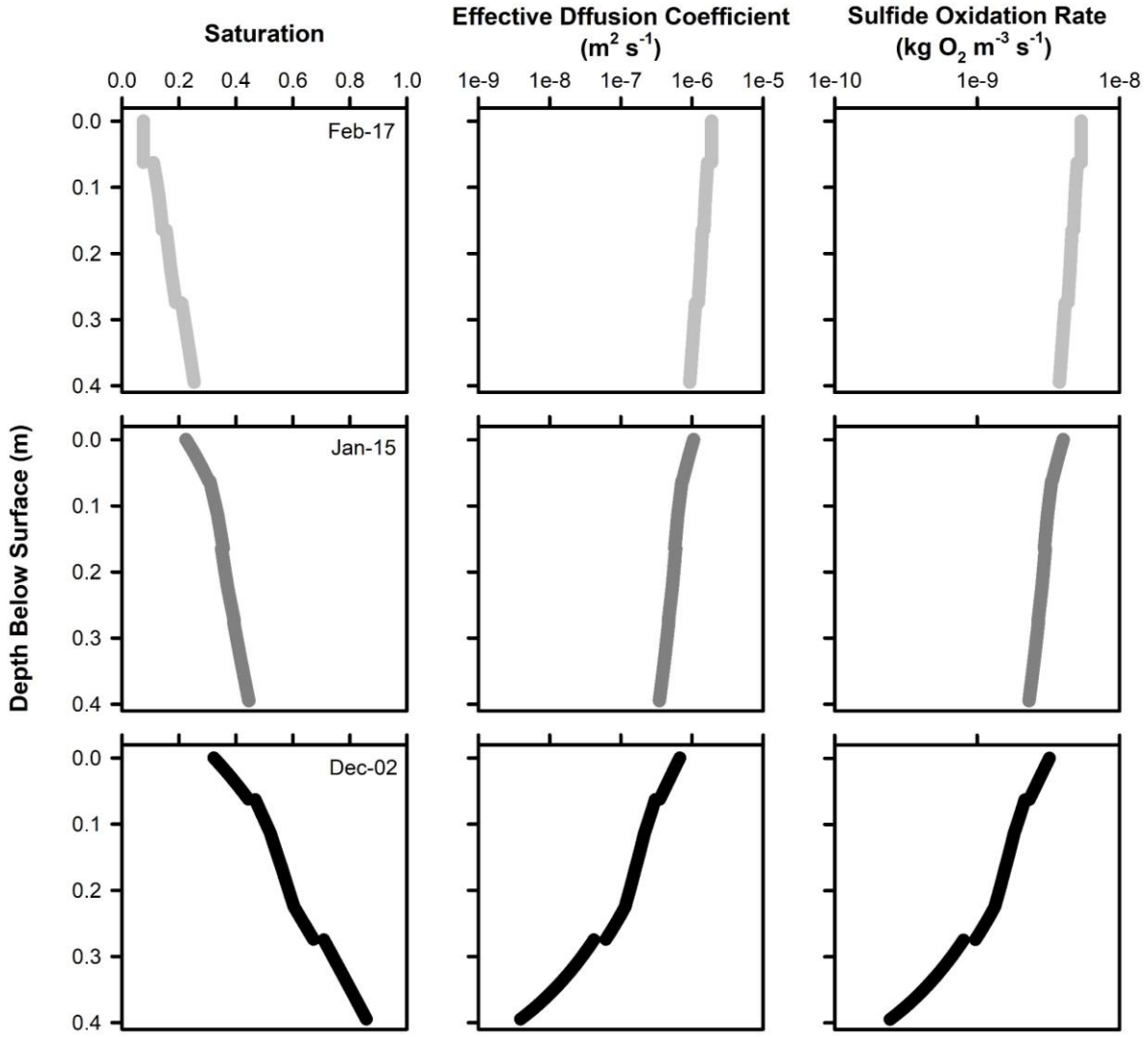

Fig. B.15 Variation in estimated D_{e_O2} values and R values based on the moisture content profile in the column for a low saturation (top), medium saturation (middle) and high saturation (bottom) diffusion experiment.

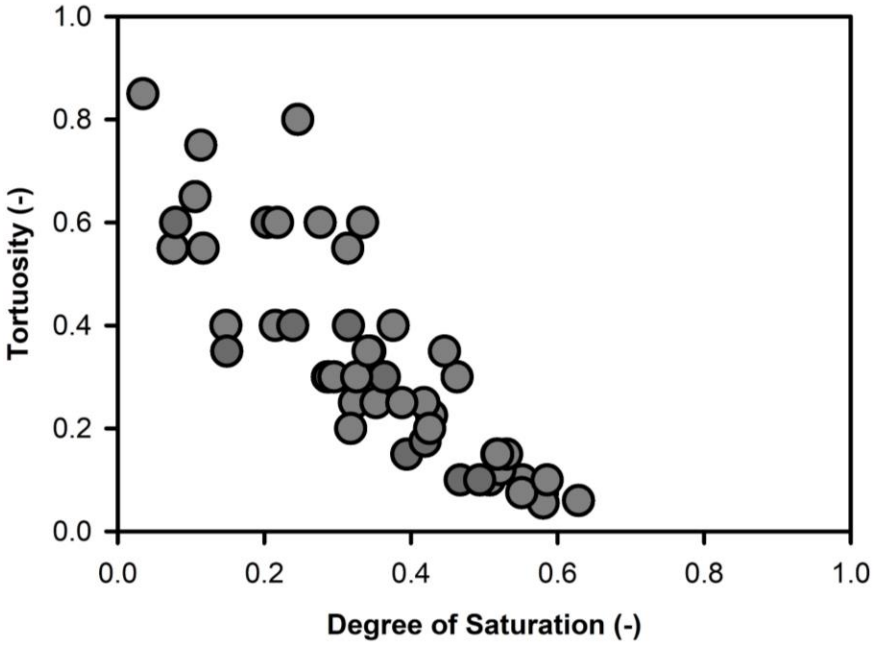

Fig. B.16 Tortuosity values derived from MIN3P simulations of experimental $O_{2(g)}$ breakthrough curves.

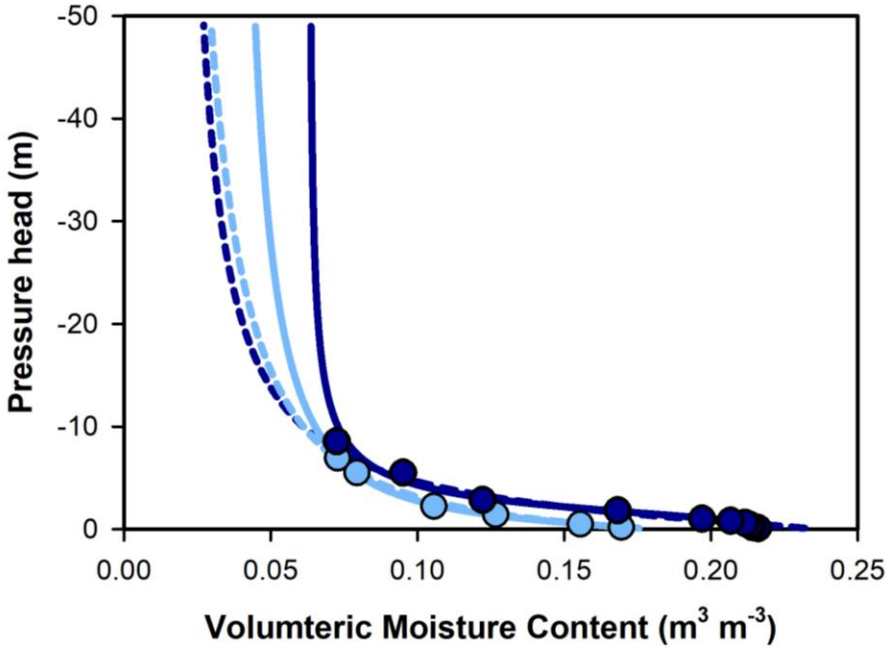

Fig. B.17 Diavik Adjusted soil-water characteristic curves based on the modified van Genuchten parameters compared to the soil-water characteristic curves from the original van Genuchten parameters.

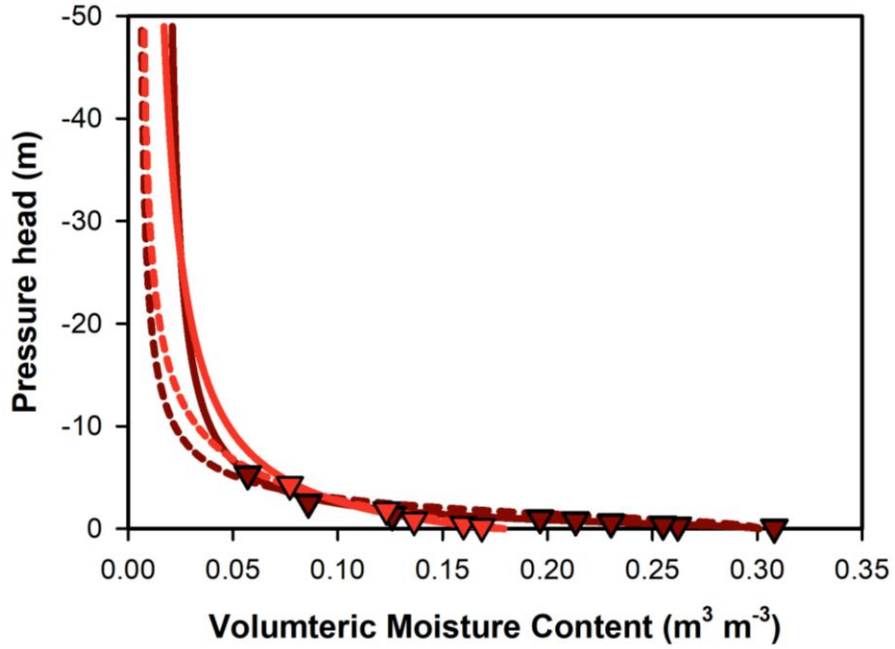

Fig. B.18 Faro Adjusted soil-water characteristic curves based on the modified van Genuchten parameters compared to the soil-water characteristic curves from the original van Genuchten parameters.

Table B.1 Diavik Drying Measured ECH_2O probe readings from the saturation-diffusion apparatus. Larger port number reflects greater depth (*e.g.* Port 1 = near surface).

Date	ECH_2O Reading [VMC (m^3 m^{-3})]			
	Port 1	**Port 2**	**Port 3**	**Port 4**
26/11/2019 - 27/11/2019	0.145	0.187	0.208	0.260
01/12/2019 - 12/12/2019	0.141	0.181	0.205	0.258
14/12/2019	0.142	0.179	0.203	0.256
17/12/2019	0.139	0.176	0.193	0.245
18/12/2019 - 19/12/2019	0.134	0.170	0.185	0.230
30/12/2019	0.129	0.163	0.181	0.225
1/3/2020	0.125	0.154	0.166	0.205
9/1/2020	0.125	0.154	0.166	0.205
11/1/2020	0.112	0.133	0.146	0.168

13/1/2020	0.104	0.124	0.136	0.150
21/1/2020	0.073	0.102	0.116	0.131
11/2/2020 - 17/2/2020	0.047	0.063	0.076	0.094
21/2/2020	0.047	0.063	0.076	0.094

Table B.2 Diavik Wetting Measured ECH_2O probe readings from the saturation-diffusion apparatus. Larger port number reflects greater depth (*e.g.* Port 1 = near surface).

Date	ECH_2O Reading [VMC (m^3 m^{-3})]			
	Port 1	**Port 2**	**Port 3**	**Port 4**
20/2/2020 - 21/2//2020	0.051	0.065	0.094	0.129
22/2/2020 - 26/2//2020	0.097	0.103	0.125	0.150
04/3/2020 - 05/3//2020	0.105	0.120	0.141	0.168
7/3/2020	0.111	0.132	0.160	0.197
10/3/2020 - 13/3//2020	0.117	0.142	0.173	0.225
17/3/2020	0.114	0.145	0.179	0.250

Table B.3 Faro Drying Measured ECH_2O probe readings from the saturation-diffusion apparatus. Larger port number reflects greater depth (*e.g.* Port 1 = near surface).

Date	ECH_2O Reading [VMC (m^3 m^{-3})]			
	Port 1	**Port 2**	**Port 3**	**Port 4**
07/09/2020 - 10/09//2020	0.145	0.187	0.208	0.260
15/09/2020	0.141	0.181	0.205	0.258
17/09/2020	0.142	0.179	0.203	0.256
20/09/2020 - 21/09//2020	0.139	0.176	0.193	0.245
30/09/2020 - 02/10//2020	0.134	0.170	0.185	0.230
10/10/2020	0.129	0.163	0.181	0.225
17/10/2020	0.125	0.154	0.166	0.205
19/10/2020	0.125	0.154	0.166	0.205

Table B.4 Faro Wetting Measured ECH_2O probe readings from the saturation-diffusion apparatus. Larger port number reflects greater depth (*e.g.* Port 1 = near surface).

Date	ECH_2O Reading [VMC (m^3 m^{-3})]			
	Port 1	**Port 2**	**Port 3**	**Port 4**
27/10/2020 - 29/10//2020	0.106	0.142	0.183	0.218
31/10/2020	0.120	0.145	0.184	0.219
02/11/2020 - 03/11//2020	0.128	0.150	0.200	0.240
6/11/2020	0.145	0.161	0.213	0.249
9/11/2020	0.176	0.175	0.224	0.256
16/11/2020 - 19/11//2020	0.189	0.186	0.242	0.340
22/11/2020 - 23/11//2020	0.219	0.265	0.399	0.308

Example of MIN3P Input File

MIN3P Version 2.0.14.761
March 23rd 2020

```
!
! Data Block 1: global control parameters
! ------------------------------------------------
!
'global control parameters'
''
.true.                      ;varsat_flow
.false.                     ;steady_flow
.false.                     ;fully_saturated
.true.                      ;reactive_transport

'done'

!
! Data Block 2: geochemical system
! ------------------------------------------------
!
'geochemical system'

'use new database format'

'define temperature'
23

'database directory'
‘Enter database path’

'define input units'
'mol/l'

'components'
1                     ;number of components
'o2(aq)'

'secondary aqueous species'
1                     ;number of secondary aqueous species
'h2(aq)'

'gases'
1                     ;number of gases
```

```
'o2(g)'

'done'

!
! Data Block 3: spatial discretization
! -------------------------------------------------
!
'spatial discretization'
1                       ;number of discretization intervals in x
1                       ;number of control volumes in x
0 1                     ;xmin,xmax
1                       ;number of discretization intervals in y
1                       ;number of control volumes in y
0 1                     ;ymin,ymax
1                       ;number of control volumes in z
1131                    ;number of control volumes in z
0.0 0.565               ;zmin,zmax
'done'

!
! Data Block 4: time step control - global system
! -------------------------------------------------
!
'time step control - global system'
'hours'                       ;time unit
0.0                   ;time at start of solution
24.0                  ;final solution time
0.12                  ;maximum time step
1.2d-9                      ;minimum time step

'done'

!
! Data Block 5: control parameters - local geochemistry
! -------------------------------------------------
!
'control parameters - local geochemistry'

'newton iteration settings'
0.0001                      ;factor for numerical differentiation
1.d-6                 ;convergence tolerance

'maximum ionic strength'
2.0                   ;maximum ionic strength

'minimum activity for h2o'
0.5                   ;minimum activity for h2o

'output time unit'
'days'
```

```
'activity update settings'
'time_lagged'                    ;type of activity update

'done'

!
! Data Block 6: control parameters - variably saturated flow
! ---------------------------------------------------
!
'control parameters - variably saturated flow'

'mass balance'

'input units for boundary and initial conditions'
'hydraulic head'                 ;input unit

'compute underrelaxation factor'
10.0                  ;max allowed update

'solver settings'
0                     ;level_vs, incomplete factorization level
100                   ;msolvit_vs, maximum number of solver iterations
1                     ;idetail_s, solver information level
1.d-7                 ;restol_vs, solver residual tolerance
1.d-7                 ;deltol_vs, solver update tolerance

'newton iteration settings'
0.0001                     ;increment for numerical differentiation
15                    ;max. number of newton iterations
1.d-6                 ;convergence tolerance
0.1                   ;sw_star

'done'

!
! Data Block 7: control parameters - reactive transport
! ---------------------------------------------------
!
'control parameters - reactive transport'

'mass balance'

'spatial weighting'
'upstream'                  ;spatial weighting

'activity update settings'
'time_lagged'                    ;type of activity update

'tortuosity correction'
'assigned tau'                   ;tortuosity correction

'user-specified underrelaxation factor'
```

```
1.0

'solver settings'
0                       ;level_vs, incomplete factorization level
100                     ;msolvit_vs, maximum number of solver iterations
1                       ;idetail_s, solver information level
1.d-7                   ;restol_vs, solver residual tolerance
1.d-7                   ;deltol_vs, solver update tolerance

'newton iteration settings'
0.0001                        ;increment h for numerical differentiation
12                      ;anticipated number of Newton iterations
15                      ;max. number of Newton iterations
0.5                     ;anticipated update in log cycles
1.0                     ;maximum update in log cycles
1.d-6                   ;convergence tolerance (global system)

'done'

!
! Data Block 8: output control
! ------------------------------------------------
!
'output control'

'output of spatial data'
1                       ;number of output times
24.0

'output of transient data'
2                       ;number of output locations for transient data
1                       ;time steps between outputs
1 1061

'done'

!
! Data Block 9: physical parameters - porous medium
! ------------------------------------------------
!
'physical parameters - porous medium'
4                       ;number of property zones

! ------------------------------------------------
'number and name of zone'
1
'Headspace'
1.0                     ;porosity
100.0                  ;tortuosity

'extent of zone'
0.0 1.0 0.0 1.0 0.395 0.565
```

```
'end of zone'

! ------------------------------------------------
'number and name of zone'
2
'Sample Above'
0.216                  ;porosity
0.2        ;tortuosity

'extent of zone'
0.0 1.0 0.0 1.0 0.3675 0.395

'end of zone'
! ------------------------------------------------
'number and name of zone'
3
'Sample Below'
0.216                  ;porosity
0.1             ;tortuosity

'extent of zone'
0.0 1.0 0.0 1.0 0.0 0.3525

'end of zone'

! ------------------------------------------------
'number and name of zone'
4
'Reduced Porosity Layer'
0.037                  ;porosity
0.0267                ;tortuosity

'extent of zone'
0.0 1.0 0.0 1.0 0.3525 0.3675

'end of zone'
! ------------------------------------------------



'done'

!
! Data Block 10: physical parameters - variably saturated flow
! ------------------------------------------------
!
'physical parameters - variably saturated flow'

! ------------------------------------------------
'Headspace'                       ;name of zone
```

```
'hydraulic conductivity in x-direction'
0.0

'hydraulic conductivity in y-direction'
0.0

'hydraulic conductivity in z-direction'
2.23d-20

'specific storage coefficient'
0.0003

'soil hydraulic function parameters'
0.001            ;residual saturation
50                    ;van genuchten - alpha
2.64                  ;van genuchten - n
0.5                        ;expn
0.185                 ;air entry pressure
0.0                   ;max bubble entrapment

'end of zone'
! ------------------------------------------------

'Sample Above'              ;name of zone

'hydraulic conductivity in x-direction'
0.0

'hydraulic conductivity in y-direction'
0.0

'hydraulic conductivity in z-direction'
2.23d-20

'specific storage coefficient'
0.0003

'soil hydraulic function parameters'
0.06             ;residual saturation
0.4                   ;van genuchten - alpha
2.64             ;van genuchten - n
0.5                        ;expn
0.185                 ;air entry pressure
0.0                   ;max bubble entrapment

'end of zone'
! ------------------------------------------------
'Sample Below'         ;name of zone

'hydraulic conductivity in x-direction'
0.0
```

```
'hydraulic conductivity in y-direction'
0.0

'hydraulic conductivity in z-direction'
2.23d-20

'specific storage coefficient'
0.0003

'soil hydraulic function parameters'
0.06              ;residual saturation
0.4                    ;van genuchten - alpha
2.64              ;van genuchten - n
0.5                         ;expn
0.185                  ;air entry pressure
0.0                    ;max bubble entrapment

'end of zone'

! ------------------------------------------------
'Reduced Porosity Layer'                      ;name of zone

'hydraulic conductivity in x-direction'
0.0

'hydraulic conductivity in y-direction'
0.0

'hydraulic conductivity in z-direction'
2.23d-20

'specific storage coefficient'
0.0003

'soil hydraulic function parameters'
0.06              ;residual saturation
0.4                    ;van genuchten - alpha
2.64              ;van genuchten - n
0.5                         ;expn
0.185                  ;air entry pressure
0.0                    ;max bubble entrapment

'end of zone'
! ------------------------------------------------

'done'
!
! Data Block 11: physical parameters - reactive transport
! ------------------------------------------------
!
'physical parameters - reactive transport'
```

```
'diffusion coefficients'
2.5d-9                      ;aqueous phase
1.8d-5                      ;gaseous phase

!
! ------------------------------------------------
'Headspace'                       ;name of zone

'longitudinal dispersivity'
0.0001

'end of zone'
! ------------------------------------------------
'Sample Above'              ;name of zone

'longitudinal dispersivity'
0.0001

'end of zone'
! ------------------------------------------------
'Sample Below'         ;name of zone

'longitudinal dispersivity'
0.0001

'end of zone'
! ------------------------------------------------
'Reduced Porosity Layer'                     ;name of zone

'longitudinal dispersivity'
0.0001

'end of zone'
! ------------------------------------------------


'done'

!
! Data Block 12: initial condition - variably saturated flow
! ------------------------------------------------
!
'initial condition - variably saturated flow'
     !1                     ;number of initial condition zones

'read initial condition from file'

! ------------------------------------------------
'done'

!
! Data Block 13: boundary conditions - variably saturated flow
```

```
! ------------------------------------------------
!
'boundary conditions - variably saturated flow'
3                     ;number of zones

! ------------------------------------------------
'number and name of zone'
1
'Top'

'boundary type'
'idle' 0.0            ;hydraulic head

'extent of zone'
0.0 1.0 0.0 1.0 0.565 0.565

'end of zone'

! ------------------------------------------------

'number and name of zone'
2

'Internal'

'boundary type'
'idle' 0.0            ;hydraulic head

'extent of zone'
0.0 1.0 0.0 1.0 0.36 0.36

'end of zone'

! ------------------------------------------------
'number and name of zone'
3

'Bottom'

'boundary type'
'idle' 0.0            ;hydraulic head

'extent of zone'
0.0 1.0 0.0 1.0 0.00 0.00

'end of zone'

! ------------------------------------------------


'done'
```

```
!
! Data Block 15: initial condition - reactive transport
! -------------------------------------------------
!
'initial condition - reactive transport'
1                      ;number of initial condition zones

! -------------------------------------------------
'number and name of zone'
1
'fullArea'

'concentration input'                  ;fullArea
2.36d-5 'po2' ; o2(aq)

'guess for ph'
7.0

'extent of zone'
0.0 1.0 0.0 1.0 0.0 0.565

'end of zone'
! -------------------------------------------------

'done'

!
! Data Block 16: boundary conditions - reactive transport
! -------------------------------------------------
!
'boundary conditions - reactive transport'
1                      ;number of initial condition zones

! -------------------------------------------------
'number and name of zone'
1
'Internal Bottom Ports'

'boundary type'
'mixed'

'mixed boundary condition diffusion for O2'

'concentration input'                  ;Internal Bottom Ports
0.12 'po2' ; o2(aq)

'guess for ph'
7.0
'extent of zone'
0.0 1.0 0.0 1.0 0.36 0.36
```

```
'end of zone'
! ------------------------------------------------

'done'
```